Design and Fabrication of a Multi-Electrode Surface for use in a DNA Based Biosensor

by

Guy Dawson

A thesis submitted to
The University of Birmingham
for the degree of
DOCTOR OF PHILOSOPHY

School of Chemical Engineering

College of Engineering and Physical Sciences

University of Birmingham

February 2019

ABSTRACT

Being able to determine if a sample contains a specific protein, chemical or biological molecule has led to the development of the field of biosensors, devices that use biological components to detect their target. There are many designs of biosensors using various mechanisms and biological components, but all successful designs both detect a target in a sample, and to give a signal to the user as to the result of the test. A challenge with many biosensors is that degradation of the bio recognition component through use, age or contamination of non-target molecules can lead to reduced signals or false positives — a signal that a target is present at a concentration which is not accurate.

The ultimate purpose of this work is to aid in the design and fabrication of biosensor devices that detect specific biomarkers in sample using DNA modified with electrochemically active redox tags as a bio-recognition molecule. The work examines different methods of preparing a raised electrodes surface, that can help increase accuracy of biosensors by having simultaneous multiple methods of detection of a transducing event, and how to prepare them for deposition of these self-assembled monolayers, a precursor in depositing DNA recognition molecules. The focus of the project is in two parts, the lithography and fabrication techniques required to create the novel surfaces, and the further development of spin on hardmasks that were used elsewhere in the project. These surfaces have been designed to aid with both signal detection and reduce false positives from the breakdown of immoblised bio-recognition molecules by using a novel three-dimensional design with both surface and raised electrodes, separated by a thin dielectric. Chapters 3 focuses on the design and fabrication of the surfaces through different lithographic and fabrication techniques, challenges and solutions of both the top-down approach, including electron beam lithography and photolithography, and bottom-up approach of self-assembled monolayer deposition, which are used to pattern features in the sub 100 nanometre scale. Different surfaces were successfully fabricated and techniques proven to work for the selective cleaning and deposition of molecule onto electrodes, required for the addition of DNA to the surfaces. Sandwich electrodes were created using a spin on carbon as an electrical insulator Chapter 4 focus on the development procedure for new spin on carbons, used throughout the project, with features designed for further applications in the fabrication industry. Advancement on a new formulation of spin on carbon were achieved, including the additions of thermal acid generators to lower the required bake temperature and time, increases in film thicknesses, drain test compatibility and etching profiles.

ACKNOWLEDGEMENTS

I would like to express my enormous gratitude to my supervisor Dr Alex P. G. Robinson for introducing me to this project, the world of lithography and micro fabrication, and for his continued support throughout the PhD. Both his expertise in the field, and his advice on personal matters has been invaluable, and his patient supervision and understanding allowed me to persist in this work. Further I would like to commend his understanding and advice on balancing a PhD together with work and with family, and for the flexibility he offered with the birth of my children both at the beginning and again part way through the project.

I would like to thank my co-supervisor professor Paula Mendes for their continued support in both academic and personal matters, and for welcoming me to a research group of excellent and talented individuals. I would also like to thank my sponsors at Defence Science and Technology Laboratory (DSTL), particularly Dr Sarah Goodchild for her input and advice on the project.

I am very grateful to colleagues and friends I have met throughout the project. Mr Karolis Virzbickas and Ms. Carmen-Mariana Popescu for making long hours in the cleanroom pass quickly, Dr Andreas Frommhold and Dr Dongxu Yang for training and advice on various equipment and techniques and Mr Alan Brown and Alexandra McClelland from Irresistible Materials for their company and work with regard to the spin on carbons. I am grateful for all the people I met on the way of which there are too many to list.

Finally, I want to thank my family, and in particular my wife Karman, and my two children. The three of you have brought me unimaginable joy throughout the PhD, and your continued support and love is what keeps me going.

TABLE OF CONTENTS

List of Tables

List of Figures

CHAPTER I

INTRODUCTION

1.1 Project Introduction

The work in this thesis focuses on the electrodes used in a sensing device called a biosensor, aiming to improve the accuracy and reproducibility of results, particularly by having a design that can reduce false positives by have multiple, close sensing electrodes. Electrochemical sensing in a DNA based biosensor can be improved by using novel approach of creating nano-sized surface structures to be used as an alternative electrode, electrically separated from the surface itself. It focuses on the creation of a three-dimensional patterned surface that makes is designed to make use of a DNA based recognition molecule. The surface is designed so as each electrode can be separately cleaned and modified electrochemically, to allow the correct deposition of the biological entities required for a biosensor to work, and to allow detection of confirmation change of the deposited molecule to be detected on multiple electrodes simultaneously to improve the functionality of the sensor.

The fabrication of these surfaces requires thin films of resists, metal deposition, etching, hardmasks and lithography patterning at a sub 100nm level, without any defects in the resulting surfaces that would cause bridging and loss of function. Chapter 3 focuses on the different techniques and approaches used to achieve this, up to the deposition and cleaning of monolayers of a thiol-alkane SAM. Throughout the project, one of the approaches used to achieve better surfaces with the use of a carbon mask as an intermediate layer, that could be spun onto a surface, as opposed to the more standard carbon vapour deposition method, which lead to further exploring this type of material. Chapter 4 focuses on the use of one such spin on carbon, which lead to further developing its properties and features both for this project and as a commercial product. This introductory section firsts examines biosensors as a whole to give relevance to the surface work and then why the design of a novel surface can improve on their accuracies. Modern fabrication methods are examined, many of required throughout the project.

1.2 Biosensors

1.2.1 What are biosensors?

A Biosensor can be defined as an analytical device that takes a biological process and outputs a quantifiable signal (1). Biosensors include a broad range of devices, each with a specific use. Perhaps the most widely known and successful biosensors are glucose biosensors used by health services and diabetics, which can measure the blood sugar level of the user quickly and accurately from a single finger prick. The creation of devices such as the glucose biosensor drastically improves the health and quality of life of millions of people around the world, and it is no wonder that research and development is being heavily invested in, with the sector estimated to be worth $21.2 billion by 2020 in the US alone (2).

The history of biosensors goes back to the early in the 20th century, with the first examples of what we would now call a biosensor being cited as the glass pH electrode, developed by Hughes in 1922 (3), and the Oxygen Electrode by Leland Clark in 1954 (4). It was nearly a decade after this, in 1962, that Dr Clark introduced the glucose biosensor (5).

1.2.2 Design of a Biosensor

A single biosensor device is usually made up of three main components as shown in Figure 1.1. First is the biological sample, which may be cells or fluid from a human or animal, environmental samples or food. Second is a bio transducer, that is the transduction of a specific recognition element of the target analyte from the biological sample. The sensing element specifically recognizes the analyte to which it is sensitive, and no other analyte that may be present. The third part is a system to read out the transduced signal for the user, and is usually electronic or optical. The selection of the transducing mechanism determines the type biosensor, with different types including Optical detection biosensors, thermal detection biosensors, electrochemical biosensors and resonant biosensors.

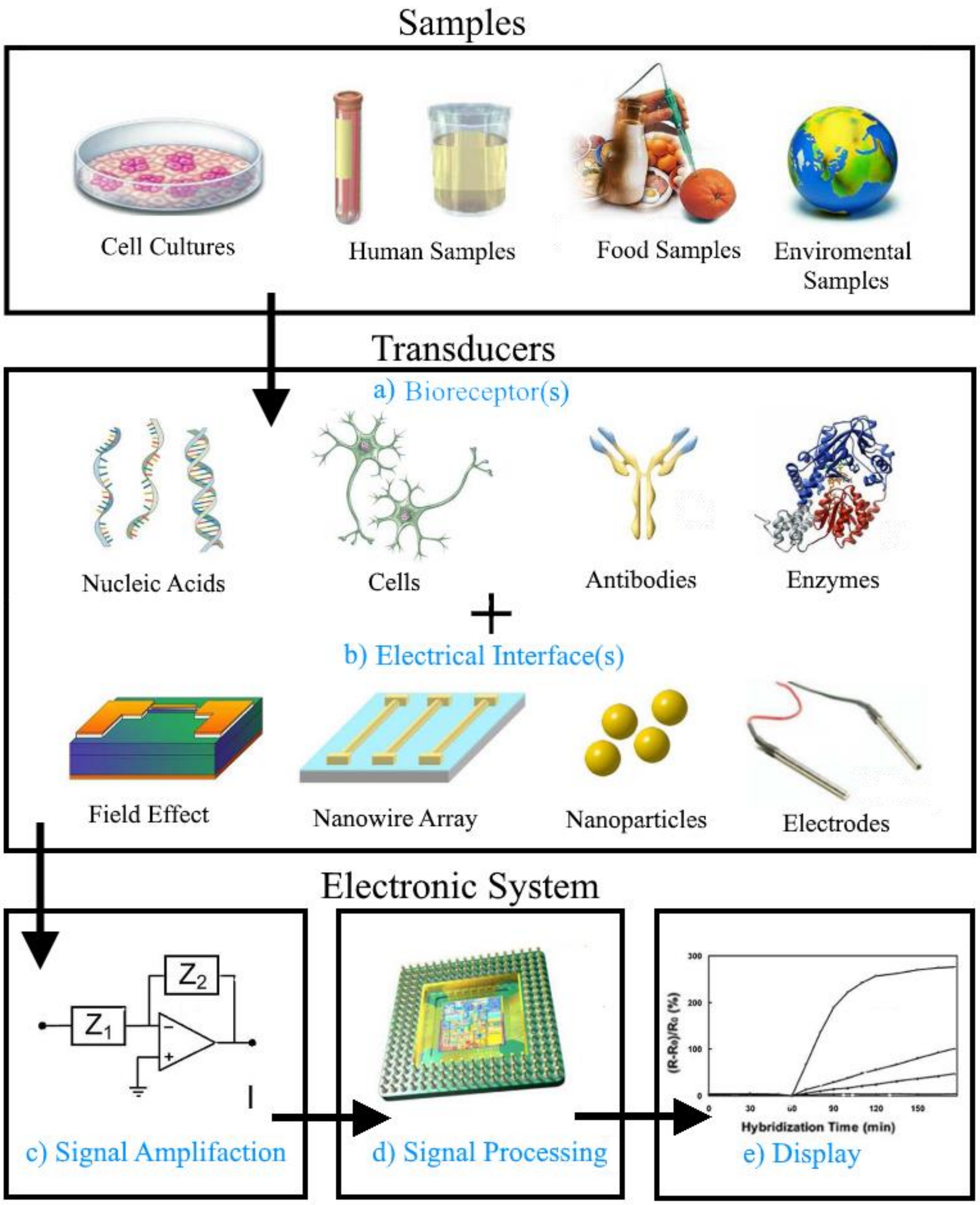

Figure 1.1 Examples of typical biosensor components. All functional biosensors require a component from each (a)-(e), whereas this work focuses on electrical interfaces. (6)

1.2.3 Limitations of Biosensors

For a biosensor to be successful, it must satisfy the conditions below (7).

- The biological components need to be stable in storage during their whole shelf life, without loss of function or accuracy with respect to age.
- The biosensor should consider environmental factors, such as temperature, humidity etc., and give results that are independent of these conditions.
- **The biosensor response should be accurate and reproducible in its working range.**
- For human samples, the sensor should provide rapid measurements of analyte.

The advantages of a so-called point of use biosensor are extremely appealing, as, for example the prominence of hereditary or degenerative diseases such as Alzheimer's (8) and cancers (9) is a major concern across the world, particularly in developed countries . Research into biological sensors to detect Alzheimer's is a much studied area, with multiple approaches being investigated (10). Likewise a review on current cancer sensing mechanisms reports various biomarkers that can be used, including cancer antigens, antibodies enzymes and DNA fragments being used to detect the presence of cancers before spreading of cancers cell becomes widespread (11). Development is focused on diagnosing devices that can detect the onset of these and similar diseases, often via genetic screening of the individual, and devices that distinguish between variations in the DNA of individuals are much needed. A point of use biosensor that is also mobile would have obvious applications, for example allowing paramedics the ability to diagnose away from a laboratory or hospital, allowing quick treatment decisions based on that diagnostic, and for smaller rural hospitals to have similar quick diagnostic abilities (12). However, several challenges exist to making accurate and reliable point of use devices, including extraction of the molecules of interest from the biological sample without specialist auxiliary equipment, rapid response times, user friendliness and high accuracy (13).

1.3 Types of Biosensors

The most successfully used recognition molecules are specific and allow for a definite signal upon addition of the analyte (14). Since most diseases result in concentrations of particular molecular signatures that deviate from the norm, measurement of the change or production of these molecules can be used to detect the condition in question. The molecules of interest may be DNA, RNA, metabolites or proteins, so detection of these has often been the focus of the research (15). As the components are biological in nature, there are different approaches that can be taken to capture the target molecule.

1.3.1 Immunosensors

Immunosensors make use of antibodies as a recognition molecule, and these have historically been widely used due to their high affinity and selective binding to the analyte (16). Antibodies have evolved to bind to the things that make us ill, (pathogens and toxins etc.), and are therefore already adapted to detecting the presence of certain biological agents that are desirable to detect. The most famous and successful example of an immunochemical biosensor is perhaps the over-the-counter pregnancy test (17), which uses qualitative measurement to detect the presence of human chorionic gonadotropin (hCG) in urine (18). In this application, the transduction element is a lateral flow test, where the antibody — combined with a coloured molecule such as latex —, is previously immobilised on a surface. On addition to the sample, the antibody / antigen pair is transported past a third set of capture elements that selectively bind to only the antigen. As the antigen will be bonded to the antibody, and thus the coloured latex, this results in a visible colour change of a test strip only when hCG is present, as shown in Figure 1.2. Antibody sensors have some inherent challenges that, aside from the pregnancy test, have limited their widespread success as point of use diagnostic devices. One such challenge is that normally the antibody binding of antigens does not produce a strong and measurable transducer event such as fluorescence, electron release or a large change in conformation (19), and although the lateral flow example used in the pregnancy test overcomes these issues, this is not always feasible. In fact, there are often two approaches to overcoming this issue. First is the analyte binding induces a conformation change elsewhere in the molecule, subsequently produces the output signal; and the second is to modify the antibody with various functional groups that respond to the presence of the analyte (20). Beyond difficulties of signal detection, antibodies require in vivo environments to work as intended, which compounded with short shelf life and the tendency to denature at elevated temperatures, make both storage and operation of such devices difficult.

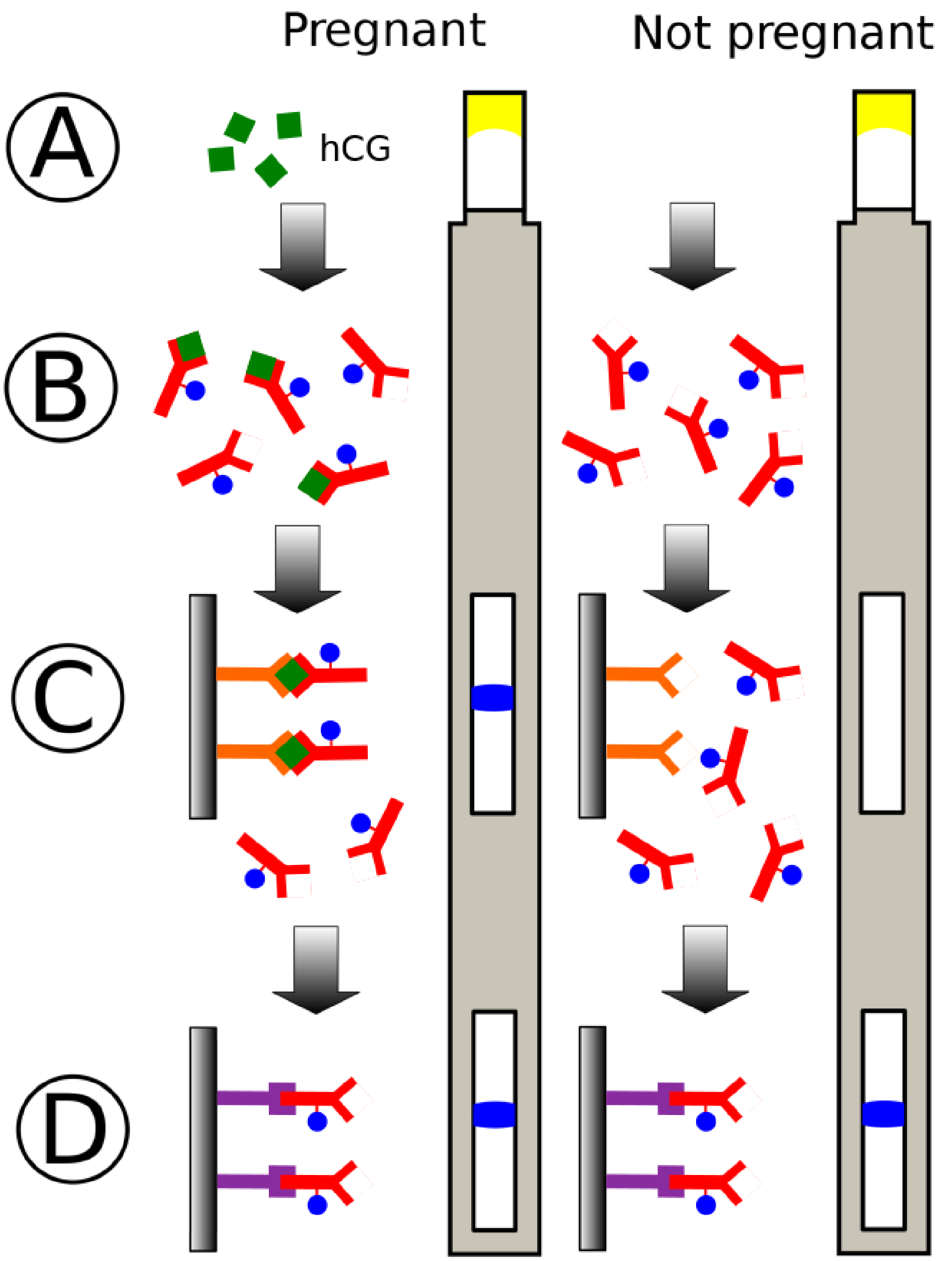

Figure 1.2 A diagram showing a lateral flow biosensor with positive and negative results.This sensor detects hCG). (A). Urine sample is applied B) dye-labeled antibodies attach to hCG. (C) hCG molecules attached to the dye are immoblised by antibodies and form a line. (D) Immoblised antibodies selective to the dye are used for control. Image from ref (21).

1.3.2 Nucleic acid based biosensors

DNA biosensors work on the basis that a single-strand of nucleic acid molecule can bind to its complementary strand selectively and effectively (22). The interaction is due to the formation of stable hydrogen bonds between the two complementary nucleic acid strands. Nucleic acid sensors either depend on the highly selective binding of the complementary strand, or alternatively the DNA receptor can also be designed to bond to another chemical species. The binding event is fast and selective, and promises the development of fast and cheap sensors that can also be a lab on chip, i.e. using different strands for multiplex testing. Teengam et al (23) have developed an assay on paper sensor that releases fluorescence molecule upon addition of different target DNA strands. Also, unlike the antibody or enzyme based sensors, DNA molecules can be readily synthesised via the polymerase chain reaction. Although there are examples of sensors where the DNA is present throughout the working medium, the majority of DNA sensors immobilise the strands onto a surface, usually gold, via thiol bonds (15).

A number of approaches have been made to turn the binding of the receptor molecule with its target into a usable signal, including various different transducing mechanisms to produce a signal for detection (24). These may be based of the conformational change of the receptor molecule, which can be modified to produce a detectable transducing effect, or which hybridisation biosensors are an example, where short (<50 base pairs) selective, single strands of DNA are immobilised on a surface. The method of immobilisation must allow the fragments of DNA to be oriented in such a way that they are approachable by the analyte in the target medium, and retain their selectivity, reactivity and stability. On the hybridisation event, a signal must be produced, and requires an electrochemical indicator or label, such as Ferrocenyl naphthalene diimide, which will bind to the DNA duplex preferentially to single strands (25,26). There are also other labels that use similar mechanisms, including the enzymes Horseradish Peroxidase and alkaline phosphatase (27). These types of DNA sensors are particularly responsive to their environment, and as such temperature, pH, and ionic strength.

A widely-explored alternative to using an indicator is to tag the receptor molecule modified itself with a label, that in turns produces a measurable effect (26,28). Most commonly the labels may be a redox active molecule or fluorescence molecule, measured via electrochemistry or spectrophotometer techniques respectively.

1.3.3 Aptamer biosensors

Aptamers are a specific type of molecule that selectively binds with a chosen analyte. There are two types of aptamers; (29) oligonucleotides (30) and peptide aptamers(31), although it is only the former that is of interest to the work in this thesis. Natural aptamers do exist (32), but the vast majority of those of interest in the medical disciplines are engineered for the purpose using a method of accelerated natural selection called SELEX. Aptamers can be created for a specific target using Systematic Evolution of Ligands by Exponential Enrichment (SELEX) shown in Figure 1.3, whereby a large library of oligonucleotides are exposed to the ligand target and those sequences with high binding affinity are separated from the bulk, replicated, and the process repeated, creating a final aptamer of high binding affinity to the specific ligand. The SELEX tool takes advantage of a sequence library of the order of $10^{14} – 10^{15}$ different base sequences of length *n* to select only the best candidates (30), which can then be isolated and the Polymerase chain reaction (PCR) used to reproduce copies for use in a sensor. PCR, invented by Mullis et al in 1987 (33), is a widely used technique used for amplifying large amounts of DNA using cycling of heating steps to continually denature DNA into separated strands, and elongation steps to create complementary strands. Repeated PCR cycles allow for exponential duplication of DNA from a very small amount of source material. Used within the SELEX process, only a very small number of viable aptamers need to be naturally selected before a library of useable sequences can be obtained.

The Selex technique also offers several other advantages, including:

- The method is in vitro, allowing the aptamer to be designed and tuned to specific affinities
- Functional groups can be tagged onto the molecule with little loss of affinity.
- Due to the production methods, there is little to no variation between batches of aptamers, unlike alternatives such as antibodies, which can have significant variation.
- The shelf life of aptamers is longer than that of antibodies.

The surfaces created in this work are designed to work with DNA or aptamer based recognition molecules, both of which can be modified to attach to SAMs (34). The dimensions of features created are determined by the available length of DNA molecules that can be attached to a SAM surface without clumping (35). This is examined in more detail in Chapter 3.

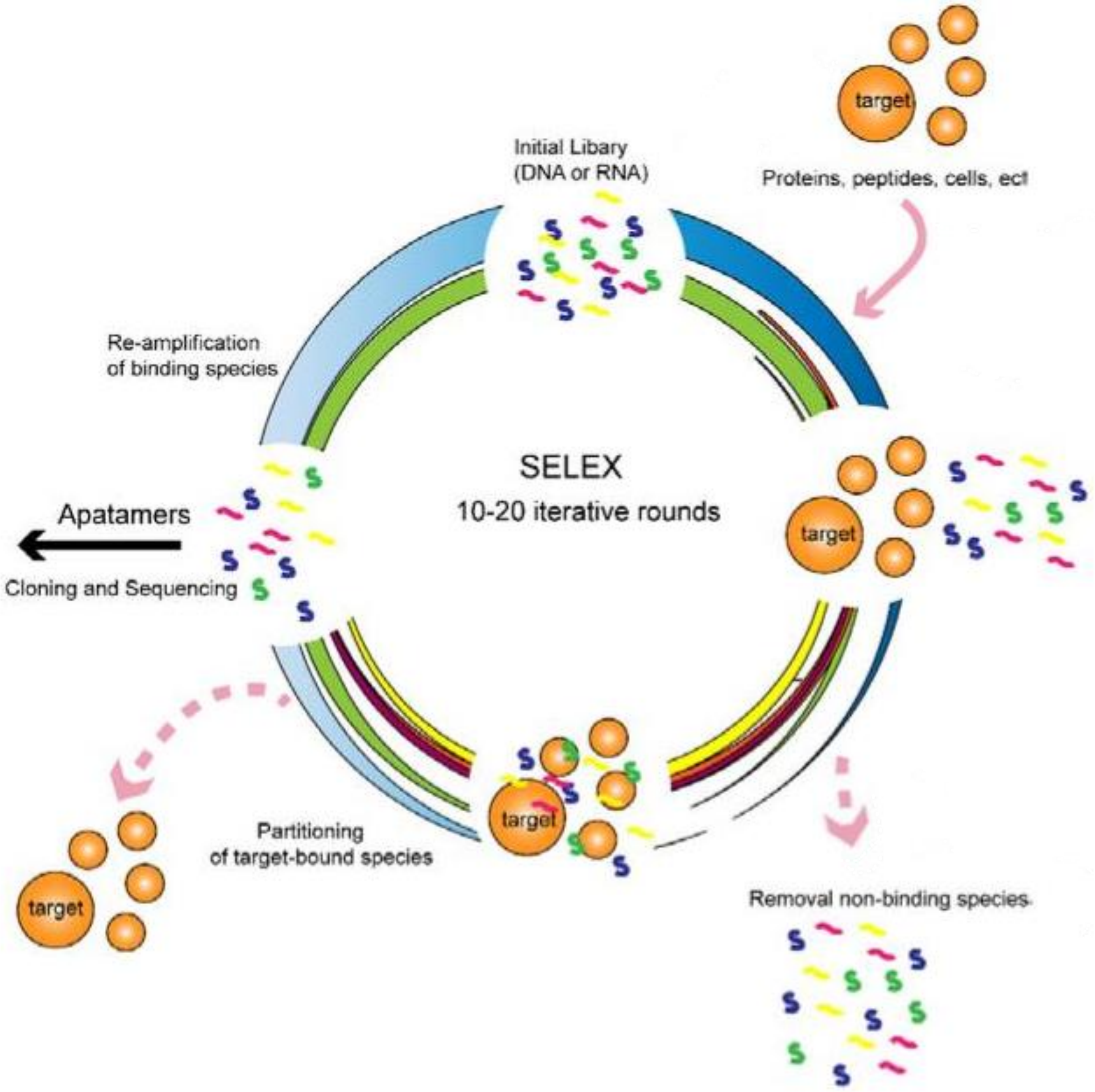

Figure 1.3 Diagram of SELEX, process Image modified from ref (36).

1.3.4 Signal Detection and the Importance of Electrode Design

Electrochemistry has become an important research area in biosensors (37). Within bio sensing, the process requires a redox active species, that is a molecule that can readily accept (reduction) or donate (oxidation) electrons. The redox reaction occurs at a potential that is unique to the redox species and experimental conditions, and requires that the redox species is in close proximity to an electrode, in essence allowing an electrical circuit to be completed. The movement of the electrons back and forth produces a current that can be measured by techniques such as cyclic voltammetry, electrical impedance or square wave voltammetry, the first of these that is used in this work. The design of the surface in this project aims to allow the deposition of molecules with a ferrocene redox group Figure 1.4. This is a redox group that is stable, its electrochemical behaviour has been well studied (38) and has been previously synthase into DNA (39).

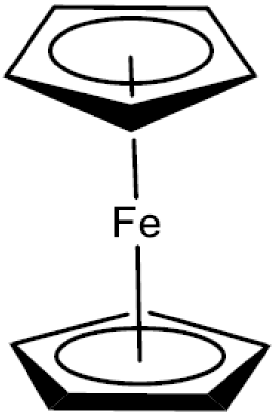

Figure 1.4 Ferrocene structure

Sensors that make use of conformational changes of DNA often make use of the stem loop (also known and a hairpin loop) (40). A stem loop consists of a single strand of DNA that has two regions of base pairs that complement themselves, allowing them to form a hairpin as shown in *Figure 1.5*. Upon addition of the complementary DNA (cDNA) strand, the loop structure is removed and the DNA takes its longer, double helix form.

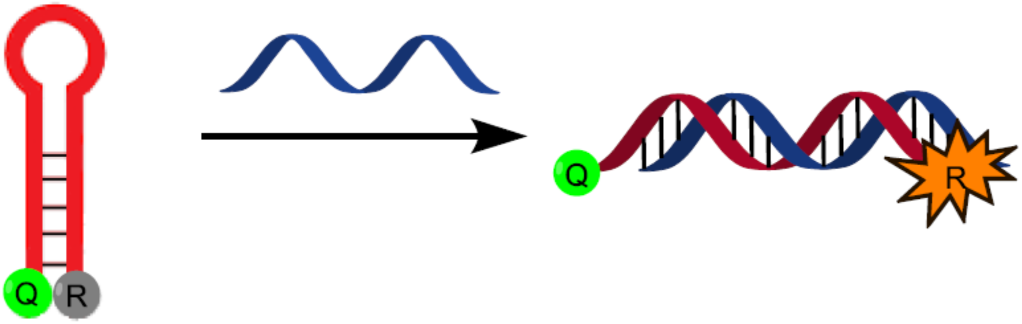

Figure 1.5 Hair pin loop configuration of a fluoresce reporter (R) and quencher. The reporter is only able to become active upon addition of a target, complementary DNA.

Work by Tyagi et al (41) shows the succesful use of a flureoence end group, quenched when in a hairpin loop but active upon addition of the complementry strand of DNA. In the work from Plaxco et al (42,43), it is shown that via conformational change upon addition of cDNA, a redox active group is moved further from the surface, which produces a change in current that can be measured using the surface as an electrode. This work also emphasises the importance of the density of a deposited molecule on the surface to allow for a strong reliable signal, without false signals from lone DNA’s redox group returning to the surface after binding of cDNA, as shown in Figure 1.6.

This set up is known as a signal off system, as the current reduces from 100% with no binding, to 0% with maximum binding. This method has the inherent flaw, that some signal could be produced from the system should the redox group become removed from the DNA, or the DNA from the surface, regardless of a binding event, giving false positive signal.

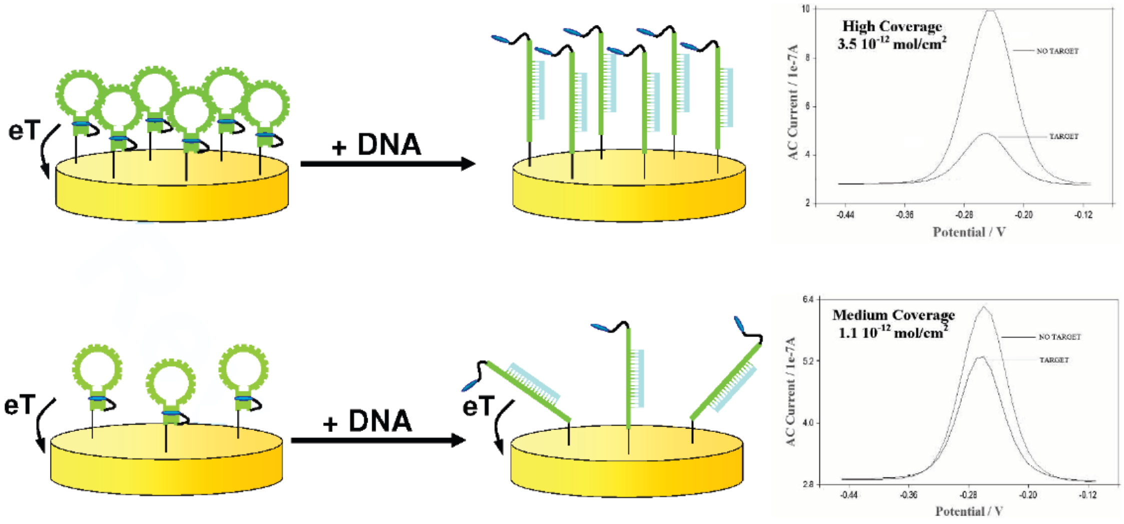

Figure 1.6 Cartoon of conformational change DNA with a redox group. The proximity of the blue redox group to the surface allows for electron transfer (eT), and a signal. Upon addition of target DNA, the redox group is moved away from the surface limiting the eT and producing a different signal. Close packing of DNA upon the surface (top) is essential to avoid signals from a bound DNA (bottom). Image from ref (42)

An alternative method of detection, the subject of this work, is shown in Figure 1.7 which uses multiple electrodes. A second electrode, electrically isolated from the surface can carry a signal that should be the inverse to that of the surface, allowing simultaneous on and off detection. The maximum length of the DNA in the hair pin formation, modified with ferrocene is usually in the region of 50 – 80 base pairs (44), corresponding to a length of around 20 – 30nm, therefore it is desirable that the distance between the surface electrode and raised electrode be within this range. Fabrication at these sizes requires specialised tools often found within the semiconductor industry, and this leads to the work within this project.

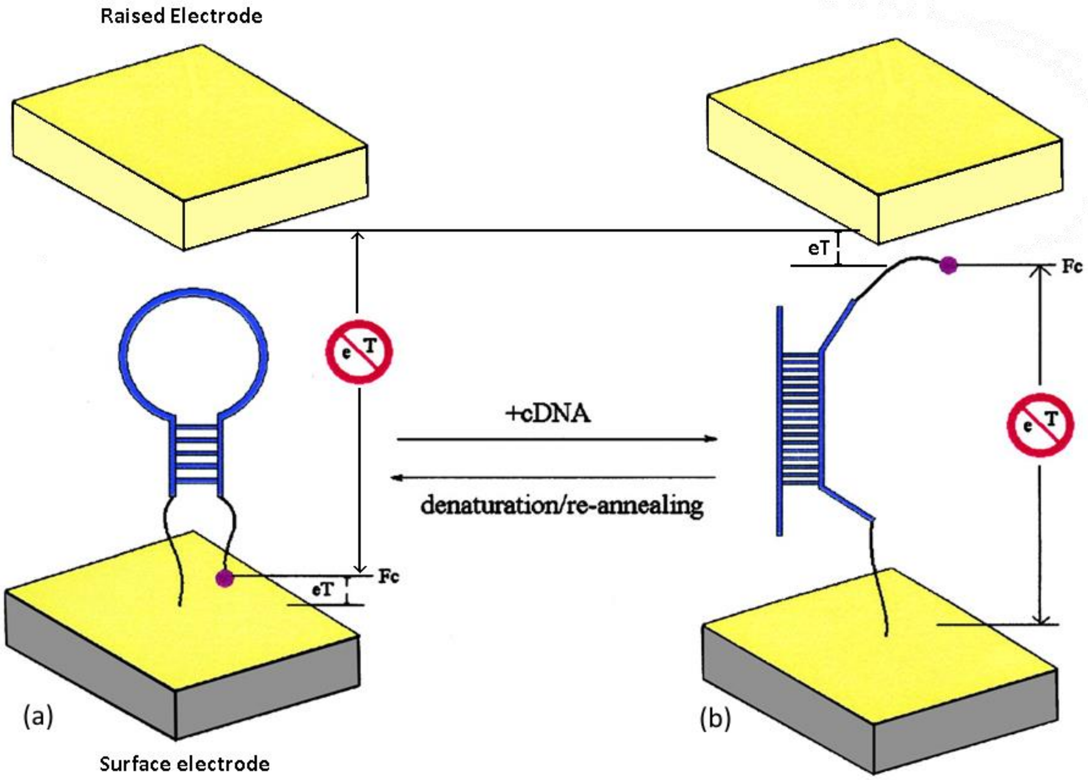

Figure 1.7 Two alternative signals The electron transfer (eT) between the ferrocene end group (Fc) and the surface stops upon addition of a complementary DNA (cDNA) due to conformational change of the bound DNA. With a second raised electrode, current, or lack thereof, can be measured independently at each electrode. Before addition of cDNA, (a) current can be detected at the surface but not the raised electrode, after addition of cDNA (b) current can be measured only at the raised electrode.

1.4 Bottom-up Fabrication

1.4.1 Introduction

The creation of an area micro or nano sized structures with two or more different electrodes that are electrically separated, the immobilisation of molecules to these surfaces, and ways of transferring a signal from a biological event to the measuring device all need to be considered in the designing of the biosensor surface. In this way techniques for preparing and creating the surface are required.

The fabrication of nanostructure devices can be classified into two different approaches, top-down and bottom-up. Top-down fabrication is the creation of complex nano structures from a parent entity (45) and can be broadly thought of as the tradition fabrication process used in the semi-conductor industry where patterns are designed on a computer and transferred to a substrate. These techniques use lithography tools to pattern with long range order and etch away or deposit material over the surface to create functional structures. On the other hand, bottom-up is an additive process where basic atoms and molecules self-assemble at a surface to create larger, more complex structures, and have application from diagnostics to therapeutics within the medical industry (46). Bottom up approaches are akin to biology and chemistry where physical conditions (e.g. temperature, concentration etc.) can be used to manipulate the building blocks into forming desired structures one block at a time. Both approaches are viable for the creations of nano sized features, but as semiconductors reach ever smaller sizes, the bottom up approach is the focus of much research so as to compliment the current top down methods used, for example in the production of semiconductor nanowires (47).

Top-down is widely used in the microelectronics industry, via the lithography in patterning and etching of silicon to create computer chips, and is an accurate and precise method that can place billions of structures in the exact locations needed for a working processor (48). The limitations of top-down fabrication come from the feature size, which is limited by the resolution of the tools and materials being used. On the other hand, examples of the bottom-up approach are the creation of nanodots and graphene from chemical synthesis (49). The advantage of bottom-up is that huge numbers of chemical entities can be created with relative eases and atomic levels of precision as the larger molecules are built up from their constituent parts without the user’s individual attention. In particular, self-assembly of molecules to form a larger structure or device is a bottom-up approach that can change the properties of a surface which is used in this work (50).

1.4.2 Self-assembled Monolayers

A self-assembled monolayer (SAM) is a spontaneously formed layer of highly arranged, tightly packed molecules covering a surface as shown in Figure 1.8. Depositing a SAM allows for different chemical and physical properties, such as the wettability and electrical properties at the surface compared to that of an unmodified surface (51). This can be a permanent change, or as an intermediate step within a manufacturing step to allow for depositions of a different molecule that might otherwise react with the bare surface. Within the biosensor sector, SAMs are widely used for a variety of reasons (52), including shielding a bound biological surface from a surface that could otherwise denature it (53), surface plasmon residence detection (54), and quartz crystal microbalances (55). Within this work, SAMs are of interest for their ability to help bind DNA to a surface via incorporation of the DNA into the terminal group of the SAM (56). Producing the DNA modified SAMs fell out of the scope of this work, but the design of the surfaces is intended to be fully compatible with DNA SAMs.

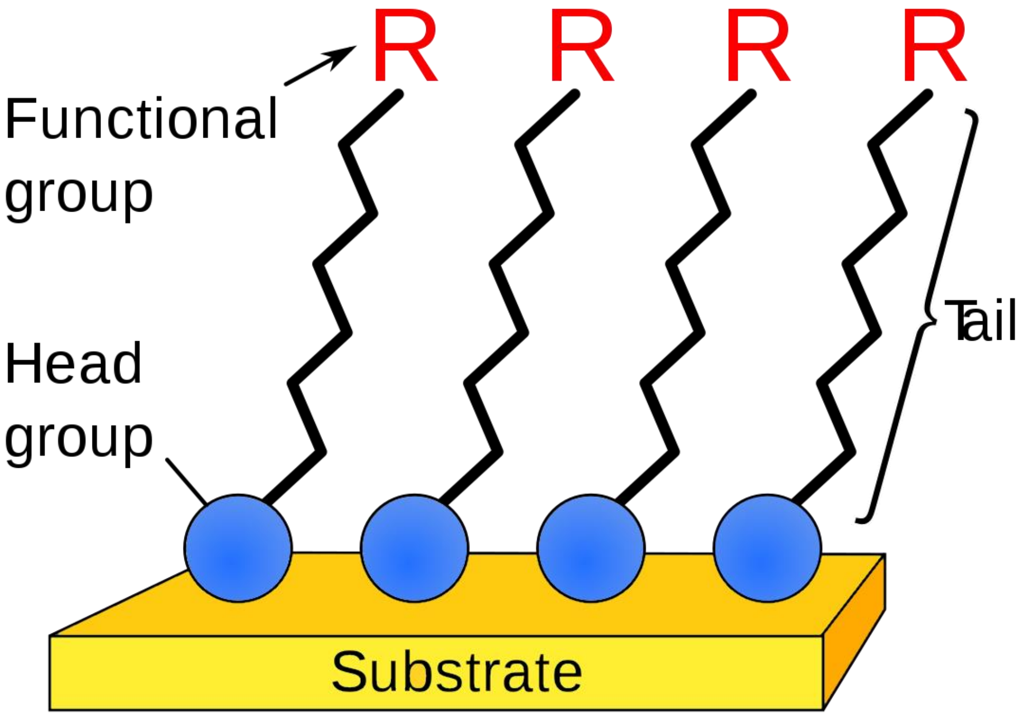

Figure 1.8 Diagram of A self-assembled monolayer on a surface Successful SAMs form a defect free single molecule layer across the surface. A single molecule consists of a head group, alkane based tail and function end group.

All SAM molecules consist of three parts, the head, the spacer, and a functional end group (57). The method of adsorption to the surface is controlled by the head group, and it is the interaction between the substrate and the head group that determines the strength of this bond. The packing and orientation of the SAM is determined the spacer group and interactions between functional group. Van der Waals forces are the major factor determining the packing arrangement and angle of the SAM to the surface, and these are predominantly affected by the length of the tail (58). Finally, the end group will help determine the surface properties after deposition of the layer and how it interacts with external molecules away from the surface. Polar functional groups such as amines or some peptides (59) also change the packing characteristics of a SAM.

There are many different types of bonds that a SAM can form with a surface including silicon — oxide bonds, gold — sulphur bonds, and carbon bond — gold bonds, described below.

> *Silane based SAM*: A silane can undergo silanation to create Si-O-Si bond with silicon oxide surfaces, a full chemical bond that is strong and stable (60). A number of methods exist to create silane SAMS (61), and may involve creating hydroxyl terminated surfaces (62). Silanes are also often used to functionalised metal oxide surfaces such as aluminium oxide or silicon oxides.
>
> *Thiol based SAM*: A thiol head group can form a bond with gold, and is a widely-used method of SAM preparation (34,63,64). These surfaces are easy to

> create and characterise, although the Au—S bond is relatively weak. The advantage of using gold based SAMS are that the surface electrochemistry of gold is well studied (63), and the thiol SAM is simple to deposit.
>
> *Alkene/alkyne bond*: A type on monolayer less widely used, but extremely stable (65). Formed between an oxide surface and an alkene/alkyne head group, these can be prepared under UV or visible light conditions. However, pre-treatment of the silicon surface requires a harsh HF dip to activate the surface and limits the electrochemistry (66). Alkyne SAMs on gold are also studied as a method to form a SAM (67).

There are many other surface to SAM bonds with other functional groups, including amines (68), carboxylic acids (69), esters(70), and fullerenes (71), but the bonds in each of these can lead to structural rearrangements of the films, surface etching and reforming (72).

1.4.3 SAM formation

The process of creating a SAM on a surface affects the quality, uniformity and whether a monolayer or multiple layers of compound are present. Self-assembly starts when absorption of a surfactant onto the surface occurs. This can be initiated from a solution of the SAM compound, or via gas phase deposition (73,74). In the case of thiols onto gold, the most used procedure in this work, an ethanoic solution of the corresponding thiol was used, whereas with silanation process both the gas phase and a toluene solution of the silane was attempted(75). Figure 1.9 shows the four stages of the creation of a thiol SAM(76).

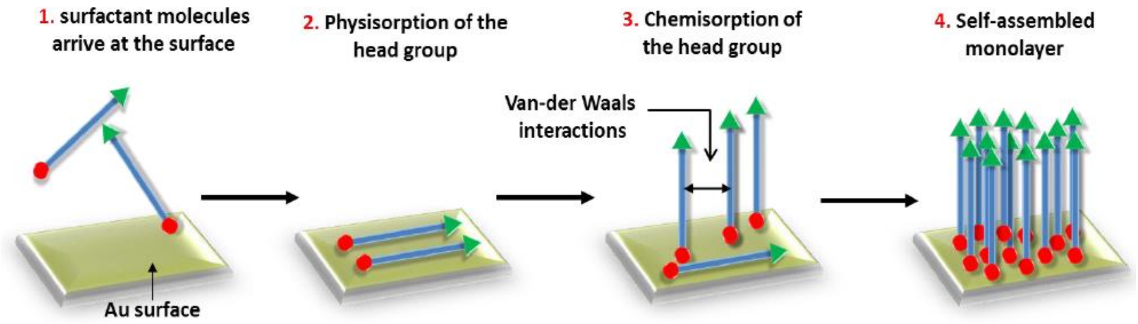

Figure 1.9 Schematic of SAM formation in four steps. Image from ref. (77).

1. Physisorption of the SAM molecule to the surface. The surfactants arrive at the surface, from solution or the gas phase. The then molecules lie parallel to the gold surface.
2. Chemisorption of the head group (thiol) occurs. This may be a covalent or ionic chemical bond, resulting in the SAM molecule lying more normal to the surface. The current understanding is the reaction is oxidative adsorption of the Sulphur group to the metal surface, releasing hydrogen in the process, but hypothesis of alternative mechanisms involving radicals exist (78,79)
3. Initial molecular ordering starts as the number of chemisorbed SAM molecules increases causing interactions between adjacent tail groups. The shorter the

alkane backbone, the faster this step occurs, and increasing the end group size increases the time required due to steric hindrance (80).

4. Definitive molecular ordering occurs after initial ordering. A chain length of at least 10 carbon groups is required for good ordering (81). The angle that the monolayer tilts at depends on the substrate lattice and choice of molecule, and is usually 30 – 35° from the surface normal for alkanethiols (82).

1.5 Top-down Fabrication

1.5.1 Introduction to lithography based fabrication

Lithography is the process of transferring patterns from one medium to another. In the semiconductor industry, the patterns are transferred from a mask to a resist, in one of the many steps required to make an integrated circuit (IC). There are multiple types of lithography, but a common theme of all the techniques is that of reducing the features size, that is the smallest writable pattern. In 1965 Gordon Moore observed that the number of transistors in a densely pack IC tended to double approximately every year (83), and since then the semiconductor industry has used Moore’s law as a roadmap, and mostly successfully, managed keep pace. Lithography techniques therefore must constantly improve, requiring development in all areas, including the lithography tools themselves, and the material design of resists and structures on the silicon. In 2017, IC with transistors using the 7-nm process (fin pitch ~27nm) were commercially available, with the 5-nm (fin pitch 21nm) transistor process predicted by 2021 (84). Feature sizes in this range start to experience quantum effects such as quantum tunnelling, and may require fundamental changes in the design of transistors going forwards (85). It is clear however, that IC based lithography requires powerful tools to image and manipulate the world on the nanometer scale.

1.5.2 Imaging the Nano World

The simplest way to image features smaller than the eye can see is to use optical microscopes, but these are fundamentally limited by the features sizes that they can resolve, with even the most powerful (visible) optical microscope not able to resolve features smaller than a few hundred nanometers. The limit of resolution (R) for a microscope using light is dependent on the wavelength of the light.

$$R = \frac{k \,.\, \lambda}{NA} \qquad (1.1)$$

Where λ is the wavelength of light, *NA* is the numerical aperture of the system and *k* is a constant dependent on the process. The numerical aperture is defined as

$$NA = n \sin(\alpha) \qquad (1.2)$$

Where *n* represents the refractive index of the medium, and α is the one-half angular aperture of the objective. In optical systems with objective lens and condensing lens, when both numerical apertures are ideal, the above equation can be simplified to:

$$R = \frac{\lambda}{2NA} \qquad (1.3)$$

Therefore, in order to improve the resolution, the numerical aperture value needs to be as high as possible, and this can be achieved using substances with higher refractive indexes. Air has n = 1, for water n = 1.33, and some immersion oils can be as high as n=1.5 (86), therefore by using different substances between the lens and the sample, the optimum resolution can be changed. For example, when high refractive index immersion oil, $n = 1.5$, is placed between the objective and the sample, under the ideal situation where $\sin(\alpha)$ approaches 1, the value of NA will also tend to ~1.5, which limits resolution of optical systems to ~0.33 the wavelength of the light, or 150 nm for violet visible light. In practice the best optical microscope can achieve closer to 200 nm, which is 1500× magnification. Fortunately, however, the maximum resolution achievable can be further increased by lowering the wavelength with higher frequencies of light such as UV, or by using photons with a lower wavelength than those of visible light photons. Extreme ultraviolet (EUV) is the current industry choice for high resolution lithography ($\lambda = 13.5$ nm), but EUV tools are not suited for imaging due to their cost and the effect of EUV radiation on the samples.

In 1924 Louis de Broglie showed that particles propagate like a wave (87) and that the wavelength of a particle can be calculated by the following equation:

$$\lambda = \frac{h}{\rho} \tag{1.4}$$

where λ is the wavelength of a particle, h is Planck's constant (6.626×10^{-34} J seconds), and ρ is the momentum of a particle. Further, the momentum is a product of mass (m) times velocity (v):

$$\lambda = \frac{h}{m} \tag{1.5}$$

The electrons velocity is determined by the accelerating voltage or electron potential (*eV)*, and can therefore be calculated by:

$$V = \frac{\sqrt{2eV}}{mV} \tag{1.6}$$

Combing and rearranging equation 1.5 and 1.6 gives the wavelength of an electron at a given accelerating voltage:

$$\lambda = \frac{\mathrm{h}}{\sqrt{2meV}} \tag{1.7}$$

Substituting the values for the mass of electron 9.1 x 10^{-31} kg, e = 1.6 x 10^{-19} and h = 6.62 x 10^{-34} shows that the wavelength of electrons:

$$\lambda = \frac{1.223 \times 10^{9}}{\sqrt{v}} \tag{1.8}$$

In practice, the velocity of an electron accelerated by high potential is a significant proportion of the speed of light, so a further consideration of the relativistic mass of electrons in a system, needs to be made. The relativistic mass (*mR*) of an electron at a given velocity is given by:

$$mR = \frac{m}{\sqrt{1 - \left[\frac{v}{c}\right]^{2}}} \tag{1.9}$$

Where *m* is mass of an electron at rest, and *c* is the speed of light in a vacuum, (2.998 x 10^{8} m/s). Therefore equation 1.8 can be modified to take this into account:

$$\lambda = \frac{1.223 \times 10^9}{\sqrt{v}} \times \frac{1}{\sqrt{1 + \frac{eV}{2mc^2}}} \tag{1.10}$$

Table 1.1 shows the theoretical wavelengths of electrons at different accelerating voltages, both with and without relativistic mass, at some typical values found in modern electron based microscopes.

Acceleration voltage (kV)	**Wavelength (pm)**	**Velocity (m/s)**	**Relativistic wavelength (pm)**
1	38.7	1.87×10^7	38.77
5	17.3	4.16×10^7	17.30
10	12.2	5.85×10^7	12.21
30	7.08	9.84×10^7	6.98
100	3.88	16.4×10^7	3.70

Table 1.1 Wavelengths of accelerated electrons

Abbe’s equation shows how theoretical maximum resolution of a particle/wave system (diffraction limited) depends on aperture size and wavelength, relevant when there are no aberrations or distortions:

$$R = \frac{0.612\lambda}{NA} \tag{1.11}$$

Substituting the values of λ from the Table 1.1, it can be seen that using electrons instead of photons would allow the resolving of features in the order of picometers, compared to that of hundreds of nanometers for visible light. In practice, there are other technical considerations that limit current scanning electron microscopes to around 0.8 nm resolution, and transmission electron microscopes (TEM) to ~50 pm, namely spherical aberration, chromatic aberration, astigmatism and distortion, which are discussed later in this chapter.

1.5.3 The Scanning Electron Microscope

Invented in 1937 by Manfred von Ardenne (88), a Scanning electron microscope (SEM) creates an image by scanning a conductive surface with electrons, and measuring the signals detected from reflected or emitted electrons from the sample surface. The images are created by a computer interpreting signals received from one of a number of detectors, the most common being backscattered electrons (BSE), secondary electrons (SE) or characteristic X-rays, but there are also cathodoluminescence, specimen current and transmitted electron detectors. When imaging, the SEM scans a finely focused spot of electrons over the area of interest in a raster scan, and the computer linked to the detector analyses the received samples to build a greyscale image. The size of this spot is what determines the resolution of the image that is created, and in modern tools the spot can resolve features as low as 0.8 –1.2 nm (89), giving a suitably conductive sample. The system that forms the electron beam, referred to as the column, is shown in Figure 1.10, along the main components of an SEM. It consists of an electron source, lenses to focus the beam using magnetic fields, deflectors to control the beam, a stage to hold the sample, and the detector(s).

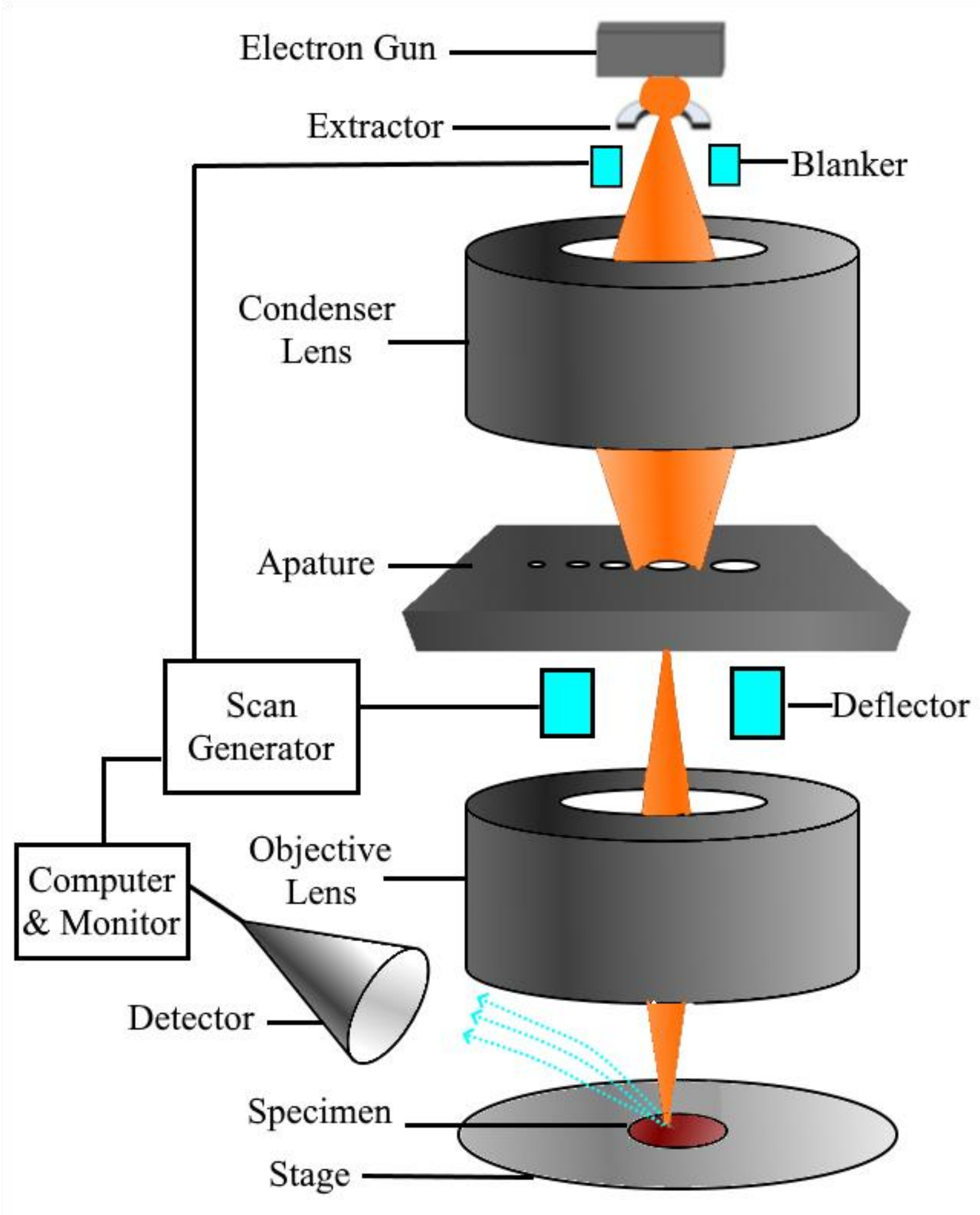

Figure 1.10 Schematic of the major components in an electron beam lithography tool.

Three main types of electron sources are used for SEM, tungsten thermionic source, hexaboride crystals (LaB_6 or CeB_6) and field emission sources (90). Electrons in thermionic sources require a certain energy to overcome the work function, with emitted electrons then accelerated by the anode. Tungsten is the simplest thermionic source, producing electrons with enough energy via heat, generated by a high current passing through the thin wire. The wire is around 100 µm in length and v shaped. A tungsten source is relatively dim (10^6 A/cm² sr) and short lived (up to 100 hr), and due to the high operating temperatures of 2800 K and higher work function of 4.5 eV, it gradually evaporates away during use, meaning breakage will occur during operation leading to contamination issues with the column. Hexaboride crystal sources operate at ~1800 K, and have work function of ~2.7 eV, giving them a longer lifetime of operation, at ~1000 hr. These sources produce current at around 10^7 A/cm² sr, allowing for higher current or smaller spot sizes. As the hexaboride tip is around 25µm diameter, electrons are produced in a smaller area with respect to a tungsten tip, putting less stress on the column optics, and this coupled with the fact that the reduced chromatical aberration of hexaboride sources compared to that of tungsten sources, means that better imaging is possible. The disadvantages, compared with tungsten sources are that a higher vacuum of 10^{-4} Pa is required, and the upfront cost is higher. With field emission (FE) sources, which are used in the tool used to conduct this research, a very fine tip ~400 nm is produces the electrons used in the beam. FE sources come in different types, but all create a more focused, brighter beam (~10^8 A/cm² sr), with a very lower energy distribution ~0.3 eV, (which allows for quicker and finer patterns) compared to either thermionic option. FE requires the highest vacuum of all the sources, but offers the best image quality in most situations. FE tips will often last more than a year due to the milder operating conditions.

The inside of an SEM is kept at vacuum to reduce scattering of the electrons within the beam with other matter. However, the electrons are mutually electrostatically repulsive, so the beam naturally tends to diverge. The degree of this effect is negatively affected by higher beam currents and lower acceleration voltages. SEM uses electromagnetic lenses, where lower voltages are required to manipulate the beam or electrons, and an electron is more heavily deflected from its course the closer to the lens (and thus the stronger magnetic field) it is. The XL30 SFEG electron column consists of a condensing lens, a set of apertures, and an objective lens.

The condensing lens, which is the closest lens to the emitter, converges the electron beam to a point (the crossover) after which it expands out again. Manipulation of this lens allows for control of the number of electrons passing through the aperture, a hole within a metal plate, located further down the column. When the action on the condenser lens is strong, the beam converges closer to the condenser lens, and thus increased angle of diverges means beam spreads out more as it reaches the aperture. This results in a larger beam dimeter, and thus a smaller portion of the electrons pass through the aperture to the objective lens located after the aperture. Alternativity, decreasing the action on the condenser lens results in a smaller beam dimeter and higher electron density passing the aperture. As well as controlling the beam currents, the condensing lens is also used to correct for chromatical aberrations.

The objective lens' primary role is focusing the electrons to a small spot on the sample. It is in the final part of the electron beam, and determines the final beam diameter and focus. The object lens is also used to correct for astigmatisation. It is Between the two lenses is the aperture plate, which consists of several different size holes in a thin metal plate. A smaller aperture will narrow the beam below it, resulting in a smaller spot size at the cost of a smaller total current. By changing the focal length of the condenser, the position of the crossover can be changed with respect to the aperture plate. In the lower convergence position, more of the beam will pass through the aperture, giving a higher beam current. This is shown in Figure 1.11.

Stigmators are required to reduce or remove the effects of astigmatism, where the electron beam becomes oblong rather than round in one of the axis, causing a smeared image. The stigmator forces the beam back to the desired shape. The lens can be magnetic or electrostatic, and a placed around the optical axis, and can be controlled by the user in the software.

Electrons interact with the sample and create a variety of effects. Figure 1.12 shows the different particles and photons that are emitted when the electron beam in the SEM interacts with the sample surface. The spot size of the electron beam is not the only determinant of the resolution of the technique — the electron beam / solid interactions are much more complex than for optical imaging, and several pathways must be considered.

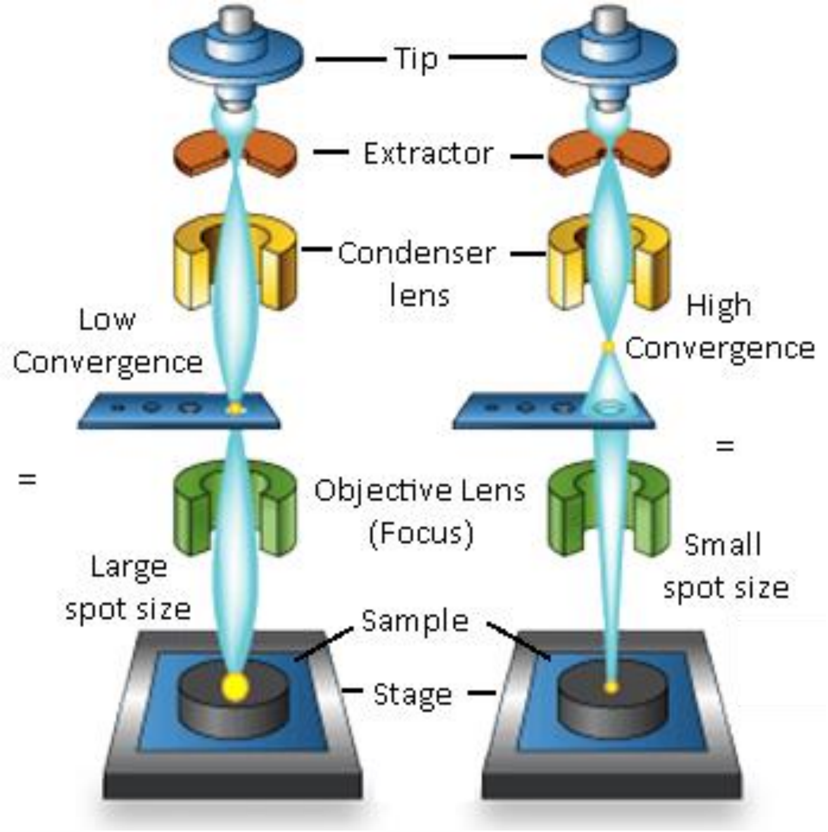

Figure 1.11 Differences in convergence and the effect on spot size. Image modified from source (91)

When the electron beam interacts with a sample elastic or inelastic interactions between the collimated primary electrons of the beam and the sample occur. Secondary electrons (SE) are created near when the ionization energy of a primary electron is high enough to interact with the substrate by inelastic interactions. They have lower energies than the primary electrons. As they are created near the surface, a suitable detector can create topological data about the sample from the secondary electron signal. Secondary electrons are the most commonly detectable electrons created at the surface. Backscattered electrons (BSE), formed by elastic interactions, are more likely to occur in atoms with heavier atomic weights, and up to micrometres away from the incident beam point. These electrons are often used to find chemical information (i.e. relative atomic weight differences) within a sample. Whilst the most common imaging modes are SE and BSE, specialised SEM's can make use of the X-ray or Auger electron emissions to measure further properties of the samples, but such capabilities were not utilised in this work.

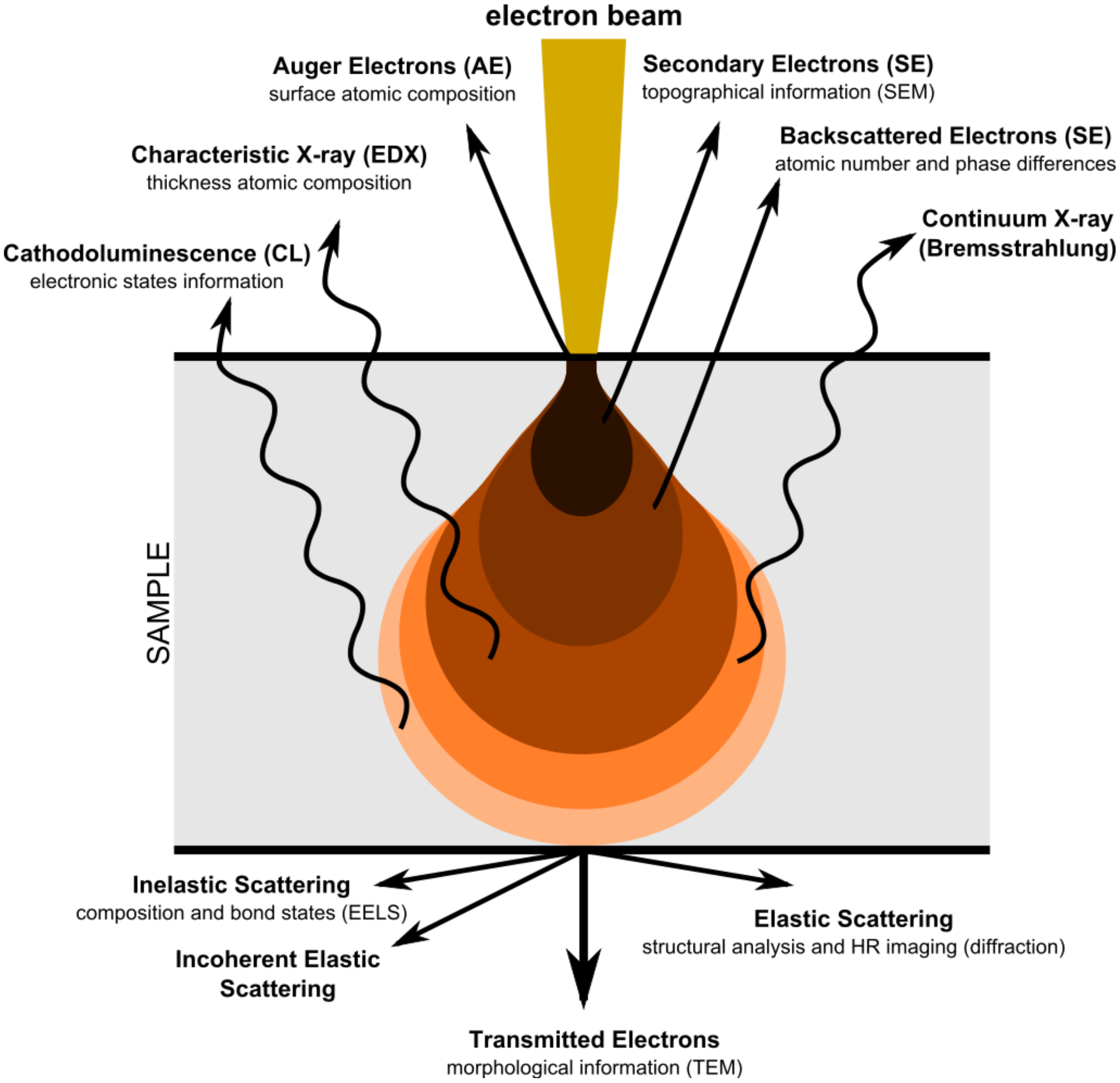

Figure 1.12 emitted signals from electron / substrate interaction. Image from ref (92)

Different detectors are used for the SE and BSE. SE are created when an incident electron from the beam is inelastically scattered from the sample. A primary electron knocks an electron out of an atom’s outer shell and is scattered through a small angle, also losing some energy to the sample. The electron which is knocked out of the atom is the secondary electrons and has a lower energy, dependent on the PE energy. An interaction with a PE of 100 keV can create 1st order SE with energies around 15 keV, but as these electrons further interact with the sample their energy decreases. SE therefore can only escape to be detected when created close to the surface of the sample (within nanometres), as those created further in quickly lose their energy by this type of interaction. The SE detector consists of a positively charged plate (~10 kV) held in front of the sample, to the side, that attracts the low energy. A fluoresce tube called a scintillator, creates light when a SE collides with it, which is amplified and processed to create an image. Control of the number of electrons hitting the detector can be obtained by use of a second charged electrode called a collector across the scintillator, which has a variable voltage. As only SE which originate close to the surface can escape, this allows high resolution topography imaging of the sample, and is the primary detection used in the images throughout this research. When the surface of the sample is perpendicular to the beam, the region that emits electrons is uniform to the beam axis, and some electrons can escape from the sample to be detected. However, when the beam to surface angle increases from an edge or step surface, the interaction volume is higher than that of the flat surface, which allows more secondary elections to be emitted from these angled edges. The detector will receive more electrons giving a brighter image, creating a well-defined image in three dimensions.

BSE are caused when an electron from the beam is deflected through a large angle by a sample atom's nucleus, and retain most of their original energy. This occurs more strongly for materials with a higher atomic weight due to their larger cross sectional area and happens deeper into the sample. BSE can be used to find information about the sample composition, but as they occur further from the surface they have a lower resolution compared to SE.

The electron beam can be accelerated to differing potentials, typically between 20 V up to 100 kV on some tools, by changing the potential between the extractor and the tip. Imaging is usually performed at 5 kV–10 kV, for resist and substrates used in this research, as this is an optimal region for conducting samples.

1.5.4 Electron Beam Lithography

The addition of a pattern generator allows for an SEM to be used for electron beam lithography (EBL) and pattern a sample with designs from software. Figure 1.10 shows a schematic of a typical ebeam system. The pattern generator can be fitted retrospectively to the SEM, as was the case with the XL30 system used in this research, and consists of blanking and deflection control to control the beam, as well as stage control to move the write field area (the area of the sample that the beam can be deflected across), all linked to a computer to allow the creation of patterns.

Ebeam patterning requires a sample to be coated by an electron sensitive resist. Patterning is then achieved by focusing the spot at different locations for different durations, causing a chemical change in the exposed areas of the resist. This change depends on the type of resist, in a positive tone resist scission of molecules leads to an increase in solubility, whilst for a negative tone resist cross linking of the molecules reduces solubility. In either tone, after the soluble areas are removed with a suitable solvent (developer) EBL results in arbitrary patterns being formed at a very high resolution.

To turn on and off the beam a pattern generator uses an electrostatic beam blanker to deflect the beam away from the sample. Due to the quick response time required for blanking, the beam blanker typically uses electrostatic deflection. In addition to blanking, the beam position is controlled using electromagnetic x- y- deflectors.

The main drawback of EBL, and the reason the technique is not suitable for industrial scale mass production, is that the process exposes only a single spot at a time —i.e. in a serial manner — and thus is very slow. In comparison, photolithography with a mask can pattern a whole wafer at once in parallel; EBL would have to expose each line of the pattern in series. However, EBL is widely used in other applications, such as mask production, research and small scale integrated circuit production, and there are multiple designs of EBL tools that can increase throughput compared to a more standard setup. EBL systems have two modes to move the beam across a write field area; raster scans or vector scans. In a raster scan, the beam moves across the write field one line at a time, gradually scanning the entire area. The beam is unblanked when a feature is to be exposed. Raster scanning, a simpler, but often more time consuming method, is based on the same beam technique used by SEM-only systems to take images. The second approach is vector scanning, where the beam is deflected to only the areas requiring exposure, potentially saving much time. However, vector scanning is a more complex operation, and can be harder to for converted SEM systems to achieve. The time saved also depends largely on the pattern created, and in some cases, may not differ from the raster scanning mode. A hybrid approach where the beam is vectored to specific areas of the writefield and then rastered is also sometimes seen.

Further to the scanning mode, the shape of the beam can be modulated to reduce the write time of a pattern. In a standard SEM, the spot is circular and Gaussian in cross-section. Typically, the beam is scanned across the resist surface in a series of pixel dots (i.e. raster scan), to create the design desired. This means that the beam must be deflected across each dot until the required dose is achieved, resulting in long write times due to settling times between shots. However, in systems containing multiple aperture plates in the column, overlapping two apertures can create a beam of different shapes, allowing for patterning of larger areas quicker. Figure 1.13 shows the different approaches available. In shaped beams, rather that single pixel dots, larger areas can be exposed at a time without the need for the beam to repeatedly move over the smaller units of the feature. Shaped beam come at the cost of resolution of the features, but may reduce the write time of larger simple features. Cell beam writing takes this development a step further using an array of apertures in the shapes of commonly features, and can be useful when a task has many repeating features.

Multiple beam systems are another approach to increase the throughput in electron beam lithography. These systems require complex optics and come at a vastly higher cost compared to single beam units, but can write multiple shots at a time and thus greatly reduce write time. They operate on the principle of using multiple electron sources, or dividing a single large electron beam into multiple independent beams with an aperture array, or a mixture of both techniques.

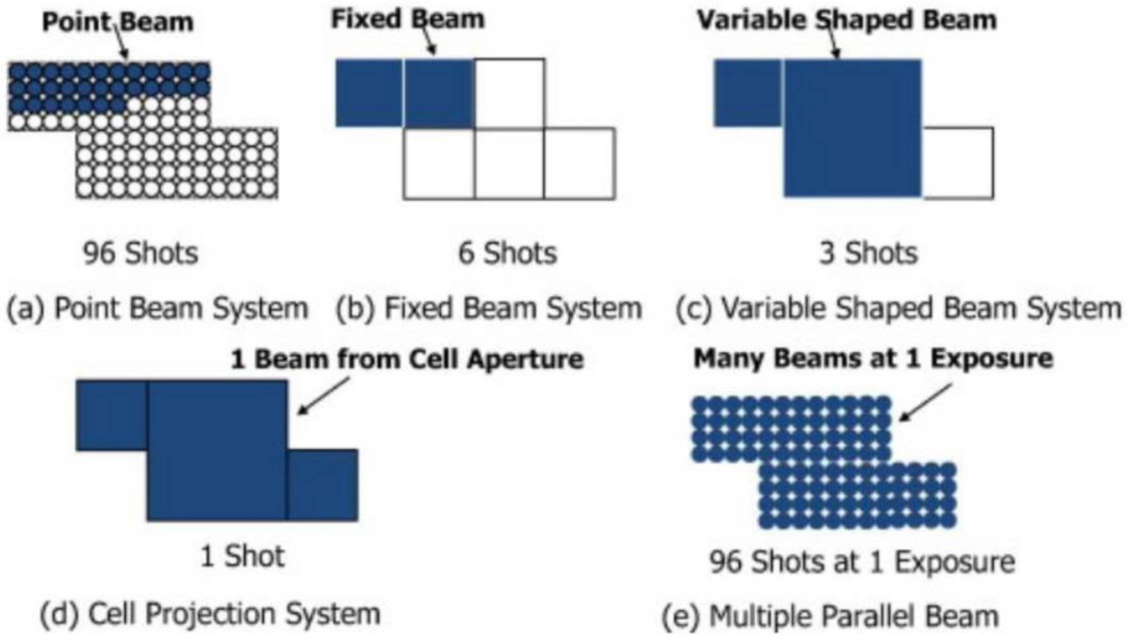

Figure 1.13 EBL writing methods showing alternative methods to increased write speed Image from (93)

EBL systems require a precisely controlled stage to position the sample. This is vital for patterns that span multiple write fields. The symptom of poor stage control is stitching errors, where multiple write fields don’t align and the pattern ends up mismatched. As patterns have features in nanometre range, two neighbouring write fields need to be very closely aligned. Multiple approaches can be used to ensure good alignment. Fine stage control is not vital, but knowing the precise position of the stage is. For example, some systems use slow but accurate piezoelectric translators to achieve fine stage control, others use more basic motors and rely on the whole write field being shifted by the lenses in the column.

The precise reading of the stage position on high end SEMs is achieved with laser controlled stages known as interferometers, which use the principle of inference in a split beam of light, and the Doppler Effect caused by the moving stage to precisely calculate its position.

1.5.5 Patterning with Electron Beam Lithography

The formula below shows that the time T (sec) required to expose and area A (cm^2) is dependent on the dose D (C/cm^2) and beam current I (A), in EBL.

$$D \times A = T \times I \tag{1.12}$$

The dose required depends on the sensitivity of the resist, and ideally a resist of a given thickness would be entirely removed at the critical dose, and unaffected at a lower dose, though in practice resists exhibit a finite rate of change from unexposed to exposed and thus the remaining film thickness decreases (or increases depending on the tone of resist) until this point. Therefore, in an ideal situation, to achieve quick writing of a pattern, the dose required should be minimized and the current of the beam maximized. In practice, however there are many other effects to be considered. The main factors and their effect on the pattern are summarised in Table 1.2.

Parameter	Process impact
Exposure energy	Resolution, sensitivity; proximity effect
Exposure dose	Pattern quality; throughput
Pattern density	Proximity effect, pattern quality
Resist material	Sensitivity, resolution, contrast
Resist thickness	Sensitivity, resolution, pattern quality, proximity effect; transferability; pattern collapse
Developer	Sensitivity, resolution, development window
Development temperature	Sensitivity, resolution, exposure window
Development time	Sensitivity, resolution, exposure window

Table 1.2 Impact of different process parameters

The proximity effect is a phenomenon that causes exposure, and thus pattern corruption, to resist outside of the patterned area. The majority of exposure is due to secondary electrons, as these are of the right energy to cause chemical changes. However, they tend only have a first order range of around 100nanometers, and therefore do not contribute to the proximity effect. However, as the primary beam travels through the resist it will undergo small angle scattering in the forward direction when it interacts with the resist (forward scattering), and when the beam interacts with the substrate, primary electrons can undergo large angle scattering and then travel back through the resist generating more SE at distances up to a few micrometres from the exposure point (backscattering). Forward scattering tends to lead to increased and unwanted dose between closely spaced features (nanometre dimensions) whilst back scattering contributes a difficult to predict and variable dose floor across the sample.

An example of proximity effect particularly relevant to the work in this project can be seen when exposing dense and narrow lines. The resist between two parallel lines may receive so many scattered electrons that it is partially developed, causing narrower lines or pattern collapse. The inverse case would be a small isolated feature, which may lose some of the dose due to scattering effects and therefore be underexposed. This results in that, as the pattern increases with the pitch, the exposure dose increases.

Mitigating the proximity effect plays a large part in successful EBL. There are different strategies which are discussed here, some which are achieved via the tool setup, and some of which rely on adjustments to the pattern.

By minimizing the forward scattering and back scattering of electrons, the proximity effect can be reduced. The average scattering angle of an incident electron can be reduced with higher energy incident electrons. Therefore, narrower effective beam diameters can be achieved with higher acceleration voltages. The effective beam diameter, *df*, due to the forward scattering of electrons can be found empirically from the formula:

$$df = 0.9\left(\frac{R_t}{Vb}\right)^{1.5} \tag{1.13}$$

Where R_t is the thickness of the resist (nm), and V_b is the voltage of the electron beam (kV). Thus, for a given resist thickness a high spec commercial tool with a 100 kV beam can reduce the beam divergence by over a factor of 6 compared to a 30 kV system. The total number of backscattered electrons are not dependent on the accelerating voltage, but the distribution of the electrons across the sample area is, thus a higher beam voltage will have the effect of diluting the number of electrons hitting the area closer to the patterning point. This reduces the cumulative proximity effect in the dense feature region, although this will be dependent on the overall patterning density on the wafer. It is possible to reduce the backscattering by making the substrate significantly thinner (e.g. going from a 500 µm thick wafer to a 100 nm thick membrane), but this is rarely practised. When patterning fine and dense patterns, the highest acceleration voltage available is often the best choice, but ultimately the user will have little choice and be limited by the tool available.

The material of the substrate is an option in some cases but changing may often not be practical due to cost or function of the project. The material of the substrate has the greatest effect on proximity effect caused by back scattering of electrons. The higher the atomic number of an atom, (z) the higher the chance that an incident electron has an elastic interaction with an atom's nucleus leading to BSE and a greater chance of inelastic collision.

Resist Selection is another major factor when patterning, and consideration as to whether to use negative or positive resist, the effective dose, contrast, sensitivity, film thickness and composition needs to be given. The beam divergence caused mainly by forward scattering has the effect of causing a sidewall undercut in positive resist, which can help with the lift-off fabrication process, but at the cost of weaker structural integrity and potential pattern collapse — due to capillary forces, when the sample is dried after development. Negative tone resists, on the other hand, experience positive sidewall tapering, which can make metal lift off particularly troublesome. The thickness of resist directly affects the forward scattering proximity effect. The effect, especially in lower kV systems, often limits the maximum resist thickness that can be used when patterning small features. The composition of the resist however, also has an important role, as the presence of heavier atoms throughout will increase the chance of BSE occurring within the resist

The most common technique used in proximity correction is dose modulation, where different parts of the pattern are assigned differing doses dependent on the expected “extra” dose they will receive from adjacent regions. For example, a region of dense of lines may assign doses higher in the outer regions (which will experience a low proximity effect) and higher in the centre of the pattern. In modern tools, the dose modulation can be performed by software, and in older systems may need to be done by the user when designing the patterns.

Pattern design can be altered to take into account the extra dose that is received by dense patterns. An example of this would be reducing sizes of features in the centre of dense regions, and allowing that the proximity effect will cause over exposure of these areas and pattern a feature larger than designed. Careful design of feature sizes in the pattern design software can achieve a similar affect as dose modulation. In practice for all but the simplest designs, it is generally necessary to simulate the proximity effect in order to suitably alter the pattern.

Imaging software is used to create the patterns in a format that can be interrupted by the tool. Files are commonly created in the GDSII format. GDSII is a hierarchal format, which allows for a cell or group of shapes to be repeated and nested, across multiple layers. in space efficient way, which is one reason why the format became the industry standard, especially when computer storage space was premium. The file is streamed to the software that controls the column, and the nested patterns must be uncompressed, which can cause a lag in writing time in some systems.

1.5.6 Electron Beam Lithography Parameters

Pattern design – During creation of the pattern, dose or design should be used to offset the proximity effect. Once the pattern is completed, parameters that affect the writing need to be selected. These include the step size, dose, spot size, write field size, beam current and dwell time. Each of these will affect the final feature resolution or write time.

Beam current: This is measured via an ampere meter faraday cup. The beam current is a function of spot size and the column setup. As the write time is directly proportional to the current, a higher current is desired.

Spot size: The size of the spot can be selected, with smaller spots required for higher resolution patterns, generally at the cost of a lower beam current. Spot size of the beam on the sample depends on the net current of the beam, aperture selected, the writing distance, acceleration voltage and the column lenses.

Write field size: This is the area that can be patterned without the stage being physically moved. Should the pattern fall over two or more write field areas, then the beam must be blanked while the stage repositions. A precise stage control can eliminate stitching errors that could otherwise occur due to stage movement. Write fields usually are in the range of 10µm × 10 µm for the finest patterns, to 520 µm x 520 µm for large exposure areas (e.g. bonding pads). Using a larger write field can limit the minimum step size due to the address space of the digital to analogue-converter (DAC) in the pattern generator. The minimum stepsize can be calculated as

$$\text{Step size} = \frac{\text{Write field}}{\text{DAC Addressable points}} \tag{1.14}$$

Dwell Time (µs): The time that the beam is held at a specific location. The actual time it takes to expose two adjacent spots is more than just twice the dwell time, as extra time for moving the beam and allowing it to settle needs to be taken into account. Furthermore, the minimum dwell time is dependent on the frequency of the pattern generator. For a 10 MHz tool, the theoretical minimum is 100 ns, but this time may be shorter than the analogue components of the column can match. The exposure dose is a function of the dwell time and the step size.

Step size (nm): The smallest distance the beam is moved between two exposure locations, for instance a line is patterned as a series of overlapping dots, and the step size indicates the separations of the centres of each dot. The total exposure time is given by the dwell time multiplied by the number of steps, which is inversely proportional to the step size. By reducing the number of steps (increasing the step size), the total exposure time would be shortened as the overhead at each step (beam moving, settling time, etc.) would be reduced. On the other hand, the larger the step size the coarser the pattern will be, meaning for fine patterns a smaller step size is required than for lower resolution patterns.

Dose (C/cm^2): The number of electrons required to fully expose (but not over expose) the resist. The area dose (usually given in µC/cm^2) is the dose required to expose an area of pattern, and is shown below, assuming step size is equal in vertical and horizontal directions.

$$Area\ dose \propto \frac{Dwell\ time \times Beamcurrent}{Step\ size^2} \tag{1.15}$$

Most tools allow for dot or single pixel line exposures, with differing doses (in µC and µC/cm respectively).

1.6 Carbon Hard mask.

As feature sizes of semiconductor devices continue to decrease, and feature density increases, it has been required that the thickness of the photoresist film must also become much thinner to avoid mechanical pattern collapse associated with high aspect ratios during the drying step after development. Pattern collapse of a resist is one of many potential challenges that the next generation of fabrication processes must address. The collapse of a resist can occur during the development and drying steps of a lithography process due to capillary forces that are experienced. The capillary stresses σ of a resist are:

$$\sigma = 6\gamma \cos\theta \left(\frac{H}{W}\right)^2 \times \left(\frac{1}{S_1}\right) \tag{1.16}$$

where γ is surface tension, H is the height, W is the width and S_1 is space between resist patterns. The term *H/W* shows the aspect ratio, and as this increases, and the distance between features decreases, the stress experienced by the resist patterns increases. There are two major failure modes of resists due to pattern collapse. When experiencing the capillary stresses the pattern can bend or break or the pattern can be removed from the surface due to loss of adhesion. Figure 1.14, shows examples of pattern collapse that can occur leading to an unsuitable pattern.

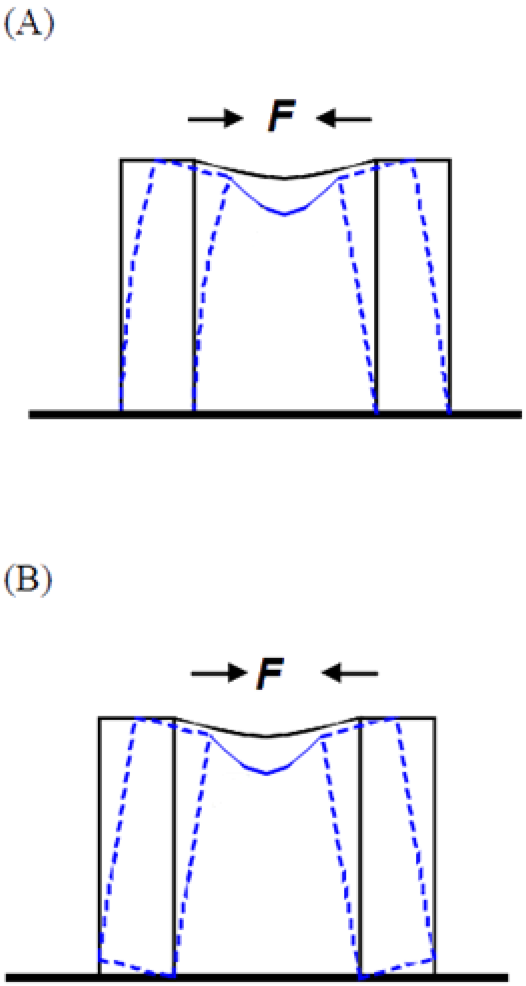

Figure 1.14 Pattern collapse of resist features, caused by imbalanced capillary forces (F) during the drying step after development (A) bending failure and (B) loss of adhesion to the substrate.

There are three factors that determine pattern collapse that lithographers have control over:

- The pattern design and geometry,
- The development and drying process,
- The physical properties of the photoresist.

Looking at the pattern design and geometry first, the terms S_1 and W are fixed by the function of the device, which gives control over only the height of the feature, determined by resist thickness. This is the primary driving force for the trend to use ever smaller film thicknesses. The limiting factor for photoresist thickness is the etching process. In etching material is removed from the substrate in areas not protected by the photoresist pattern, however the etching process will inevitably remove the resist too, albeit at a slower rate. The need to achieve etch transfer therefore constrains film thickness reduction (to mitigate this it is possible to increase the etch durability of the resist in some cases).

The drying process is an important step and many groups are looking at ways to improve this step and reduce pattern collapse. Huang et al has been using surfactants to improve collapse margin of line-space patterns surfactants (94). Drechsler et al use cationic surfactants to a similar effect (95). The challenges faced with surfactant use that of pattern shrinkage and deformation, which often leads to further collapse. The properties of the resist, particularly high yield strength, Young’s modulus and a strong interaction with the substrate can lead to a resilient resist that can withstand the capillary stresses, and these factors play an important part is resist formulation and design. Larger bulky molecules such as alicyclics, fullerenes and benzyl rings tend to lead to a resist that can withstand higher stresses, but these groups do not always lead to the sensitivity, selectivity and wettability required by the photolithography process.

A separate approach that is the subject of part of this thesis is the use of intermediate layers in a multilayer stack to allow the continued use thinner resist film, but at the same time not limit the depth of etching that can be achieved. The process is shown in Figure 1.15. In this case, the multilayer stack is created by coating the silicon wafer first with a layer of amorphous carbon, followed by a thin layer of silicon on top, and finally a thin photoresist on top. The silicon is usually deposited by sputter coater, and in the range of 10nm thick. While the resist is thin, it is durable enough to enable etching of the thin silicon layer. This thin silicon layer can then be used to etch the thicker carbon layer, leaving a relatively thick carbon hard mask for the final etching of the feature into the substrate. Silicon has near infinite etch resistance to O_2 plasma used to etch carbon and thus an extremely thin silicon layer can be transferred into a much thicker carbon layer. In this way, the lateral dimensions of the photoresist pattern and the vertical height of the final carbon pattern are used to etch the substrate.

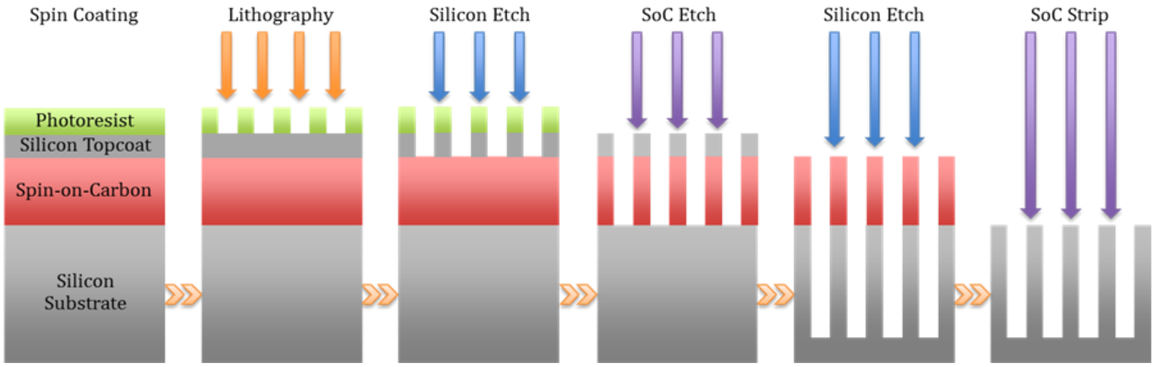

Figure 1.15 The process of lithography using a carbon hardmask (96)

The conventional method of depositing the carbon layer has been via chemical vapour deposition (CVD). However, since semiconductor node size 45 nm, spin-on-carbon (SOC) has become more widely used. This demand for a SOC is due to fewer defects, better alignment accuracy and a lower cost compared to CVD, and as this can lower manufacturing costs and increase throughput. Research for more etch resistant SOC hard masks is ongoing. Additionally, with good planarization and gap filling capabilities, SOC can be used in novel applications in places where CVD or other methods are less suitable. The spin-on-carbon used in this project is a fullerene based hard mask, manufactured by Irresistible Materials (IM) (97) in a collaboration with the author of this thesis, focusing on high carbon content and low metals. The former trait is desirable for increased etch resistance, whilst the latter is a necessity of the semiconductor industry to prevent wafer contamination and metal leaching. Chapter 4 focuses on the development, adaption and characterisation of a new series of SOC for use as a hardmask (HM) based on the HM-340 formulation. The HM 340 are a series of resists based on modified fullerene molecules, and a crosslinker to render the film insoluble in the casting agent when baked.

Development of high carbon content (carbon >80%) SOC for use in the commercial fabrication of devices is an ongoing area of research across the semiconductor industry. Ohnishi discovered an empirical law that states the RIE etch rate is a linear function of the Ohnishi number, where:

$$Ohnishi\ number\ = \frac{N}{N_c - N_o} \tag{1.16}$$

where N is the number of atoms in repeat polymer, N_c is number of carbon atoms and N_o is the number of oxygen atoms.

The IM fullerene films both increased etch resistance due to carbon content, allowing for thinner films, but also have few C-H bonds that contribute to the wiggling effect, that is the distortion of patterns when etching with fluorenes, most noticeable at high resolutions.

CHAPTER II

Equipment and Methodology

A number of experimental techniques have been used during the fabrication, resist preparation, and characterisation of the results presented in this thesis. This chapter introduces the various equipment used and major techniques, and has been subdivided into the broader categories of:

- Exposure and patterning tools including metal deposition techniques and focusing on photo lithography and electron beam lithography.
- Resist and sample preparation including SAM preparation
- Characterisation techniques of samples and films introducing Ellipsometry, Contact and electrochemical cyclic voltammetry.

2.1 Fabrication Tools

2.1.1 Scanning Electron Microscope

A Scanning Electron Microscope, mentioned in the previous chapter, was widely used for imaging samples and exposing patterns, and unless otherwise mentioned, imaging was performed using an XL30 SFEG SEM (FEI) at the University of Birmingham. The XL30 consists of a Schottky field emission gun (SFEG), with a beam energy of 0.2 keV to 30 keV. The tip current, as measured by an ampere meter falls between 1 pA and 25 nA. This SEM includes an ultra-high resolution mode which can resolve features in the sub-10 nm range. The XL30 stage is mechanical and does not feature a laser interferometer. It can tilt to create cross sectional images.

2.1.2 Electron Beam Lithography

The XL30 described has had an ELPHY Plus beam controller and pattern generator from Raith GmbH attached. This module gives control of the beam blanking and deflection allowing control of the beam, and modifying the SEM to become an electron beam lithography tool. The pattern generator allows the beam to be used to create a pattern generated by CAD software by controlling the beam dwell time and the position of the beam. The dose of exposure D_A or D_L, of an area or a line respectively is given by:

$$D_A = \frac{(l_e \times \Delta\tau)}{\mathit{\Delta} l^2} \tag{2.1}$$

$$D_l = \frac{(l_e \times \Delta\tau)}{\mathit{\Delta} l} \tag{2.2}$$

Where l_e is the beam current, $\mathit{\Delta}\tau$ the dwell time and $\mathit{\Delta} l$ the step size. The dose required is a function of the resist’s sensitivity and thickness, the substrate, and the proximity to other areas of exposure. The total write time is calculated by the total dwell time at each position multiplied by the number of positions across the sample, with an overhead that includes moving the beam to the spot and computing time. In practice this means for high resolution dense patterns with a small step size, where a small spot size is required and therefore beam current is low, the total write time can add up to days when both fine features and larger areas need to be created, which is often not practical in a busy lab. Therefore, small areas of denser patterns were created on one tool, and a second electron beam lithography tool, or a photoaligner was used to create larger areas such as electrode pads and wiring in a multistage setup. This required the addition of alignment marks and multiple stages of fabrication.

The exposure of resist with the EBL system required first the manual focusing of the tool and astigma calibration, and the measuring of tip current. This was achieved using a checkerboard calibration target, a chessy, on the stage, and gold nanoparticles in the order or 10–100 nm diameter to ensure that good initial focus is achieved. The tip current was measured by positioning the un blanked beam on the Faraday cup of the stage, and measuring the resulting current with an external ampere meter.

2.1.3 Patterning

Patterns are the designs that are transferred to the chip from the software. The design of a pattern depends on the function of the chip, but also depend on the substrate and resist being used. Patterns are created in a software package called Elphy quantum, in which an image is created from polygons, which are given a base dose multiplier. During patterning, the data from software is transferred to the pattern generator that controls the beam. The software allows for the creation of areas, single pixel lines (SPL) or single pixel dots, with the latter two methods causing the beam to move over the sample just once. In this project, the majority of dense patterning was performed by area doses or SPL. However, by using area polygons, variations in the width of an area as well as in the dose given to each polygon allow for better proximity correction in denser patterns. Unfortunately, the Raith software did not come equipped with proximity correction modules built in, so manual variation of the dose was applied, with lower effective doses towards the centre, feature rich areas of the designs and higher dosages on the borders.

2.1.4 Dosages

The doses required to fully expose an area depend on the sensitivity of a resist, but are also a function of process conditions and the developing solvent and conditions. In practice, it was not possible to find the data for the perfect exposure and it instead had to be worked out experimentally for each pattern and resist. In its simplest form, the dosage pattern design allows for identical block areas to be exposed across different areas of a substrate, each to be exposed at a known but different dose. This would result in a sample with under exposed, over exposed and correctly exposed areas. This is then repeated with a smaller range of doses to determine the optimal conditions required.

2.1.5 Photolithography

Photolithography was performed using the PLA-501FA Mask Aligner (Canon) shown in Figure 2.1. The aligner could expose with UV light at wavelength of 436nm, 405nm and 365nm from a USHIO 250W super high-pressure mercury lamp. Filters were available to create monochromic exposures. The tool takes 4-inch wafers, and was used to expose single or multiple chips by mounting these upon a blank wafer. Alignment was precise to ~0.5um, and can be set for proximity contact – where the mask is held a number of micrometres above the substrate, soft contact –where the mask is in soft contact with the substrate, and hard contact – where the mask and substrate are held together with significant force by use of compressed gas under the wafer. In all cases the mask is held above the sample by use of vacuum.

Figure 2.1 The PLA-501FA Mask Aligner (Canon) used for photolithography. The lighting in the laboratory is filtered of UV to protect the photoresist from unwanted exposure (hence the yellow case).

Masks used in this project were designed and drawn in the CAD program Draftsight 3D. These patterns were transferred onto acrylic or quartz glass (fused silica) masks at JDphoto(98), the opaque parts of the mask in chrome, with a minimum feature size of 2.5 µm. The quartz glass, although expensive has the advantages of being easy to clean, hard wearing, has low thermal expansion and a high light transmission rate.

2.1.6 Nano Imprint Lithography

Compression of sandwich electrodes was performed by on an Atlas press, shown in Figure 2.2.

Figure 2.2 Atlas press with a heated plate used for nanoimprint lithography

2.1.7 Sputter Coater

The Auto 306 RF sputter coater (Edwards) located at the University of Birmingham was used for metal deposition of high melting point materials including hafnium oxide and silicon dioxide, as well as being used with the metals gold and chrome. Equipped with three 3” diameter targets of 3 – 6 mm thickness, multiple different materials can be deposited without needing to vent the chamber to atmosphere. The RF magnetron was run between 100 – 300 W power depending on the target and deposition rate, with argon atoms used as the sputter medium.

2.1.7.1 Adhesion

Silicon wafers used throughout the project have a native oxide layer of silicon dioxide (SiO_2) that forms under standard conditions. Due to the poor adhesion of gold to silicon oxide, this oxide layer must either be removed, or an adhesion metal used. The removal of silicon oxide to form a hydrogen terminated surface requires a 1 minute dip in an aqueous solution of hydrofluoric (HF) acid. Although used in some cases in the project, the hazardous nature of HF and incompatibly with some developed resists led to the use of an adhesion metal layer being the preferred method of adhesion. Chromium or titanium are most commonly used between the substrate and the surface metal, and in this project ~5 nm chromium was sputtered before the gold using the Auto 306 RF sputter coater. As the sample does not need to be brought back to atmosphere before adding the second metal, there is less oxidation of the chromium that would otherwise lower adhesion, and it is for this reason that the sputter coater is often preferred over evaporators even though it is a more highly anisotropic process.

2.1.7.2 Lift off

Lifting off metal to remove all metals from the un-patterned areas of the substrate was performed using a suitable solvent to remove remaining resist, commonly acetone. This was performed by submerging the sample in acetone for 30 secs, following by spraying acetone directly onto the sample. In cases where more vigorous process was required, the sample was submerged in an ultrasonic bath for 10 secs – 5 min, but this ran the risk of damaging finer features. In areas were the resist remained on the substrate after the lithographic development, it was now stripped off, removing any overcoated metal, whilst the metal deposited in the patterned areas (clear of resist) was retained on the substrate.

2.1.7.3 Annealing and post deposition

A tube furnace (Carblite) allows for heating in air, oxygen or nitrogen rich atmosphere up to >1000 °C. To improve the quality of gold layers, sputtered samples can be annealed by heating to 300 °C for 8hr in N_2, resulting in a smoother film with larger grains and fewer voids in the gold surface.

2.1.8 Etching

Multiple methods of etching a material are available, these are wet and dry etching, reactive ion etching (RIE) and inductive coupled plasma etching (ICP).

The simplest method, wet etching, uses a liquid or etchant to remove the material and is isotropic, acting equally in all directions. The exception to this is when the active species attacks a crystal face, etching different faces at different rates, resulting in a non-isotropic wet etch. Although wet etching is simple and fast and controllable, it results in a large undercut in the mask as shown in Figure 2.3, profiles which are not desirable in this work.

On the other hand, dry etching makes uses of a process gas plasma to remove material from the sample, either by physical bombardment with energetic ions (sputtering), or chemical reactions with etchant gas species. Physical etching is typically anisotropic, and chemical dry etching often more isotropic. RIE is a combination of both physical and chemical dry etching, using a high-powered radio frequency (RF) electromagnetic field to create a plasma from a source gas, such as SF_6. In RIE, an RF electric field accelerates electrons in the chamber towards the top; the grounded wall of the chamber, and the bottom of the chamber containing the wafer or substrate, causing a build-up of negative charge only on the wafer. The positive ions in the plasma are attracted to the wafer by the potential difference, where both chemical and kinetic processes remove material. In this way, the etch is very anisotropic and selective. The process of ICP is similar to that of RIE, except that wafer is held at negative potential by its own RF power source, allowing a larger process window as ion current and ion energy can be controlled individually, along with chamber pressure, temperature, and the etchant gas. A Plasma pro 80 Inductively Coupled Plasma (ICP) (Oxford instruments) was used for anisotropic etches in this work.

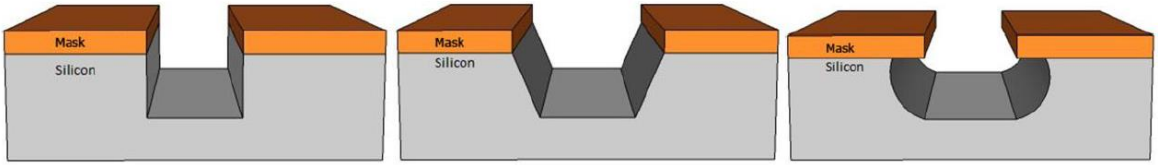

Figure 2.3 Wet and Dry Etching profiles showing (left)completely anisotropic (centre) Partially anisotropic and (right) isotropic etching of silicon (99)

2.1.9 Asher

A 100-E (Technics GmbH) plasma Asher, located at the University of Birmingham was used after patterning and prior to metal deposition to remove surface resist scum from a patterned surface. A Plasma Asher creates an oxygen plasma that removes organic residue at a low rate, whilst not damaging the substrate or metals underneath. The process relies on high energy oxygen plasma reacting with carbon and hydrogen molecules in organic resist, creating CO_2 and H_2O. The Plasma processor 100-E was run at 100–200 W power typically for 1–3 min. A second Asher of higher power, the HPT-100 Asher (Henniker Plasma) was used to remove carbon hard mask at a reasonable rate.

2.2 Substrate preparation

Unless stated otherwise, substrates used in this work were chips of <100> orientation, n-type doped silicon, diced from 4 inch wafers, measuring 18 mm by 18 mm, for ease of use and compatibility with equipment. All sample preparation was performed in a class 10,000 cleanroom, at controlled temperature (21°C) and humidity (40%), away from sources of ultraviolet (UV) or bright light. The dicing machine used is a DAD321 automatic dicing saw (Disco), ensuring a consistently sized chip. In some cases, whole wafers were required to be used for resist characterisation, in which case it was discovered that any pre-cleaning steps did not improve results, however when diced, the cleaning was essential for good quality films.

2.2.1 Resist Preparation

The resists were deposited according to the method in their datasheets, and may include the following steps:

- **Pre-clean and prebake.**

  Chips underwent an acetone clean in an ultrasonic bath for 10 min, an ultrasonic bath in isopropanol (IPA) for 10 minutes, followed by drying with N_2. In some cases where dry conditions were essential, an additional dehydration bake at 120 °C for 2 minutes was used. Samples were then used for resist spinning immediately after cleaning.

- **Application of resist and spin coating on P-6708D spin coater (SCS).**

  The thickness of resist film depends on the concentration of the resist solution, its solvent and the spin conditions. Variation in the spin recipe, particularly the maximum spin speed, is used to control thickness. For commercially available resists the spin speed curve is provided, for resists developed in lab in this project spin speed curves were created. Spinning typically used a two to three step recipe, starting with a slow spin at 500 RPM for 5 secs to ensure the resist is spread across the sample. The spin speed was then ramped up (ramp time 1 second) to the final spin speed of ~1000 – 5000 RPM for 60 sec. For the faster spins (>4000 RPM) an additional short spin step of 4000 RPM for 3 secs before ramping to the final speed was introduced (doe to constraints of the tool).

- **Post Application Bake**

  A post application bake (PAB) was required by most resists to ensure full solvent evaporation, PAB conditions are resist specific, for example, for PMMA 180 °C for 1 minute is required.

- **Bilayer Films**

  In some cases bilayers or multiple layers of resist were required for better profile or thicker films. In these cases, a second application of the appropriate resist was deposited on top of the existing film, and the spinning cycle and PAB repeated.

- **Exposure**

  Exposure of samples occurs after PAB. Any samples not to be used immediately were stored in a vacuum desiccators until exposure.

- **Post exposure bake**

  A post exposure bake (PEB) is required for some resists to drive chemical reactions necessary for exposure.

- **Pattern Development**

  Development conditions for PMMA and SML based resists required developing in IPA: Methyl isobutyl ketone *(*MIBK*)* solutions at 3:1 ratio for 60 secs or with IPA:H_2O at 7:3 30 secs in an ultrasonic bath respectively.

.

2.3 Characterisation

2.3.1 Surface Profiler

A Dektak3ST (Veeco Instruments) surface profiler was used to measure the thickness of metal films. This equipment allows high precision depth measurements of approximately 5 nm resolution across a sample’s surface by contact scanning of a diamond tipped stylus across the area of interest. The diamond tip is electromechanically moved across the sample and coupled to a linear variable differential transformer (LVDT), in which vertical displacement of the stylus is transferred to the LVDT and these movements converted to analogue electrical signals. The signals are processed to create a graphic profile of the surface in question where depth and other topological information can be obtained. The surface profiler has a stylus force that is controllable between 1–10 mg, and the maximum thickness that can be measured is 65 µm, making the profiler suitable for harder resist and under layers, as well as metallic patterned features. To determine film thickness for resists or under-layers, a small scratch was made with a scalpel through the film but not damaging the hard silicon surface underneath. The depth of this scratch was then measured.

2.3.2 Ellipsometry

The thickness of resist, hardmasks and self-assembled monolayers were determined by spectroscopic ellipsometry, using a Jobin-Yvon UVISEL ellipsometer with a xenon light source. Light with a wavelength range of 250 – 800 nm, with a scan increment of 2 nm, is scanned on the sample giving 276 sample points per run. Models used for fitting were based on a silicon substrate with a native silicon oxide layer, Si_SiO2_unbaked_(Classical) for carbon under layers, and Si_SiO2_organic_(Cauchy abs) for resists on silicon, and Au_organic_(Cauchy abs) for thiol based SAMs on gold layers.

Ellipsometry is non-destructive and highly sensitive, process that uses differing wave lengths of the electromagnetic spectrum between UV and infrared (IR) frequencies. The optical properties of a film change with thickness, and this can be used to non-destructively measure the depth of a film layer. Ellipsometry uses light of different polarisation to scan the surface and uses the reflected polarisation of light to calculate a thickness. Generally oblique angles, where there is a larger change of polarisation are used, and typically the angle is ~70°. The basic setup of an ellipsometer is shown in Figure 2.4. Polarised light irradiates a sample, and the reflected light is repolarised and analysed. The amplitude of the polarisation state of the light, *s* (oscillated parallel to the plane of incidence) and *p* (perpendicular to the plane of incidence), once reflective and normalised become r_s and r_p, that are used to calculate complex reflectance ratio (ρ) using the following equation:

$$\rho = \frac{r_p}{r_s} = tan(\Psi)e^{i\Delta} \tag{2.2}$$

where tan(Ψ) is the amplitude ratio upon reflection, and Δ is the phase shift (difference). The values of Ψ and Δ can be fitted to models so as to determine the optical properties of the sample, and the thickness of each layer of material. The choice of model is paramount as the computer system tries to minimise the difference in the model and experimental data to extract the required film parameters.

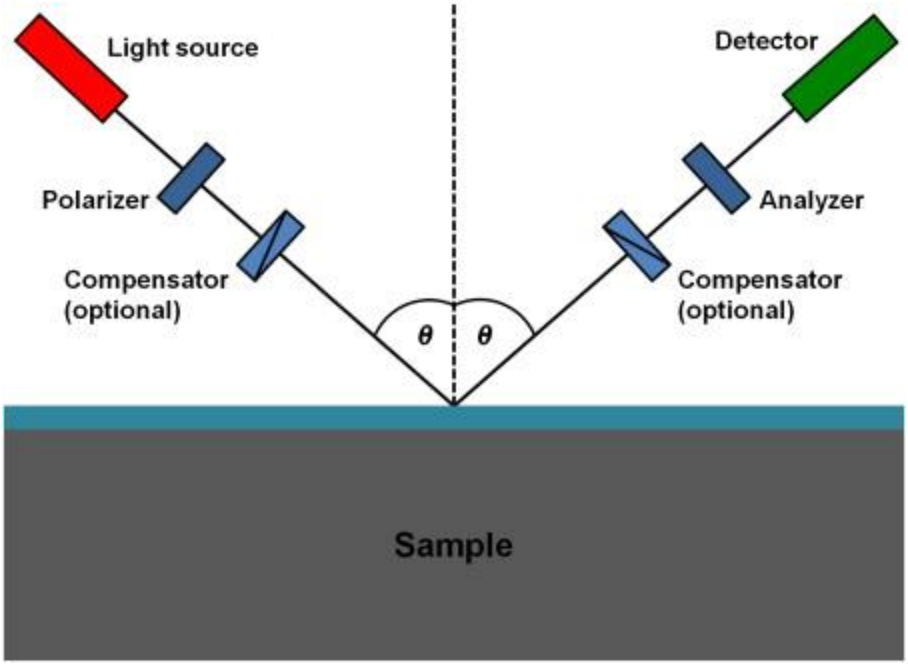

Figure 2.4 The components in ellipsometry

2.3.3 Contact Angle

Contact angle (CA) were determined using a home-built apparatus using a KP-M1E/K camera (Hitachi) connected to a PC running FTA Video Analysis software v1.96 (First Ten Angstroms). Unless stated, ultra-pure deionised H_2O was used, and a micro syringe used to add or remove liquid in a dynamic and controlled fashion. A video feed of 4 frames were taken per second was recorded as the drop volume increased, and decreased. The image recognition software FTA Video Analysis software v1.96 was used to measure the angle at the 3-phase air — surface — drop boundary. Results are performed in triplite and averaged. The contact angle of a substrate is defined as the angle of the drop of a liquid droplet on a surface, and is able to determine the wettability of a system at given temperature and pressure (100,101). Contact angles in practice suffer from hysteresis, and therefore a range of advancing and receding measurements are required to obtain the contact angle, with the difference between known as the contact angle hysteresis. In this work contact angle measurements were used to characterise the quality of substrate or SAM surface, with poor quality SAMs exhibiting significantly differing angles compared with ideal surfaces.

Using a dynamic sessile drop technique, the angle at the three-phase intersection of the water/surface/air is calculated multiple times during drop growth (advancing) and drop reduction (receding) using the analyses software on different frames of the video feed, at 4 frames per second.

2.3.4 Cyclic Voltammetry

Cyclic voltammetry (CV) is a characterisation technique that gives quantifiable information about electrochemical reactions. It was developed by Millar et al in 1985 (102), and since has become a widely used technique in surface chemistry. CV is a type of linear sweep voltammetry, but whereas a linear sweep can measure either oxidation of reduction, measuring the current when using a positive or negative change in potential at a surface, CV uses a triangular wave, as shown in Figure 2.5, to sweep reversibly giving measurements of both oxidation and reductions(103).

Equation 2.3 shows the reactions that are happening at the species during oxidation and reduction.

$$Oxidation: A^- \rightarrow A + e^-$$

$$Reduction: A + e^- \rightarrow A^- \qquad (2.3)$$

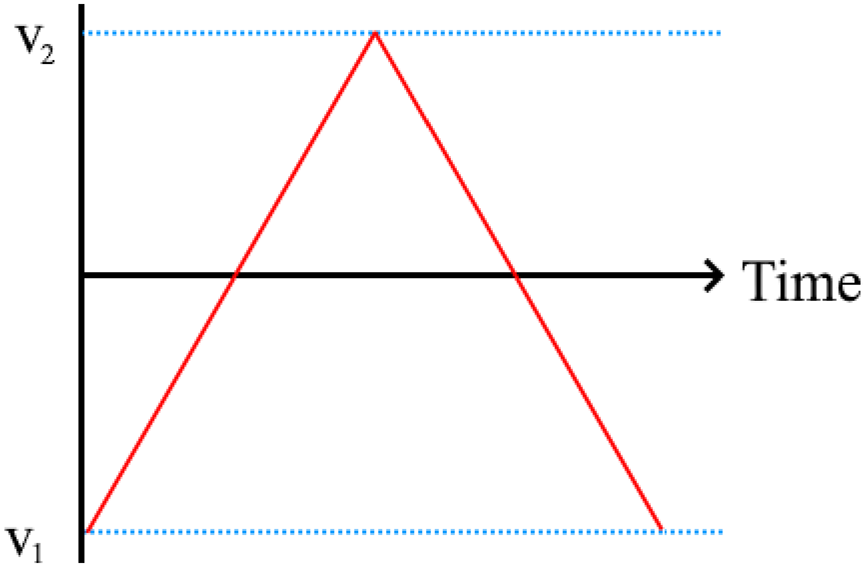

Figure 2.5 Voltage as a function of time in cyclic voltammetry

The voltage is increasing at a constant rate (V_1 to V_2), known as a forward scan, then decreased at the same rate in the opposite direction (V_2 to V_1), known as the reverse scan. The potential is applied by a working electrode, and the current flowing through this electrode at each part of the sweep is measured and plotted and gives a distinct cyclic voltammogram. An example of a single species voltammogram is shown in Figure 2.6. Note that due to convention the positive potential is on the left side of the chart. In this voltammogram, during the forward scan, the species is first fully oxidized with a positive potential, and then the potential is lowered towards the reduction potential ($-V^{red}_p$). The current increases as more of species is reduced, up until the maximum value ($-i^{red}_p$). The current falls off as the concentration of unreduced species falls. Assuming the redox species is fully reversible, a sweep in the opposite direction (V_2 to V_1) causes an oxidation of the species, with a current of i^{ox}_p and oxidation potential of v^{ox}_p.

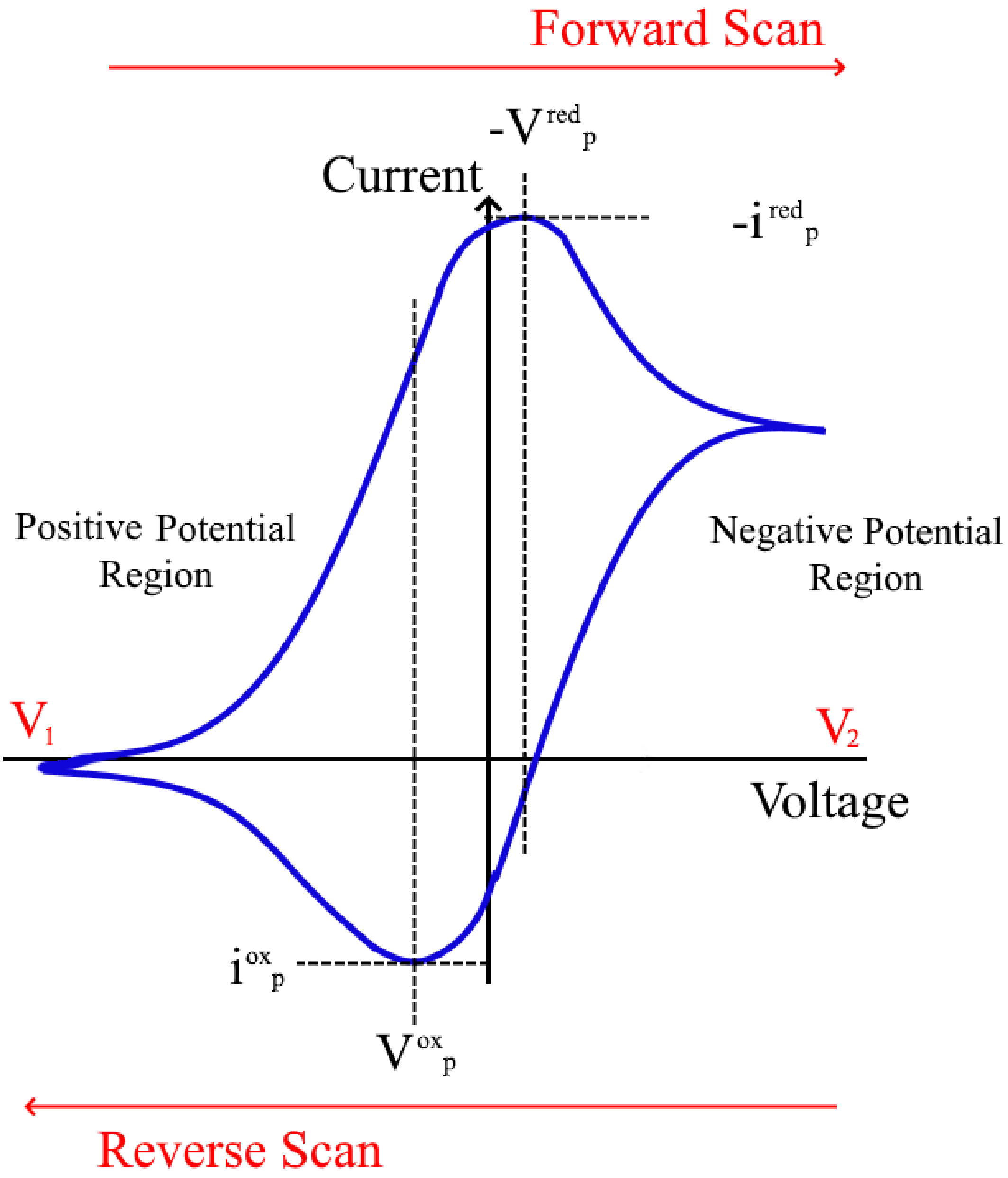

Figure 2.6 A typical voltammogram for a single electron system. Terms are described in the text

In a fully reversible system, multiple sweeps would not change the shape of the chart. The shape of the oxidation and reduction peaks are usually similar. By examining the shape of the voltammogram, information about the reaction rates and surface can be obtained (104). In the case of this work, a non-redox SAM would block the gold surface, significantly changing the shape of the voltammogram to almost a single line. The presence of a redox active group close to the surface would also give a distinct graph. CV requires a three-electrode system due to the difficulty of controlling and measuring current and potential simultaneously. The CV set up consists of a working electrode, reference electrode and counter electrode, connected to a potentiostat, as described below:

- Working electrode – This is the electrode are which the reaction investigated occurs. In the case of this project the working electrode would be the metal surface where SAMs will be formed.
- Reference electrode – This electrode is made of a material where its potential is constant so that other electrodes potential can be measured against it. The reference electrode in this work is the silver-silver chloride electrode (Ag/AgCl) (FLEXREF, WPI, USA).
- Counter electrode – The function of the counter electrode (also known as the auxiliary electrode) is to serve as a sink for electrons so that current can pass through the system. It is usually a platinum wire.

The setup requires use of an electrochemical cell to hold the working electrode, and an electrolyte solution in which the experiment is performed. The cell has a working area of 75 mm^2. CV studies required a redox reaction. Experiments in this work, unless stated, are carried out using the iron complex ferricyanide, the oxidation and reduction reactions are shown in the following equation.

$$\mathrm{Fe(CN)_6}^{3-} + \mathrm{e}_{-} \rightleftharpoons \mathrm{Fe(CN)}_6^{-4} \tag{2.4}$$

A conductive medium is required and the three electrodes must be in contact with this. Commonly a solution of potassium hydroxide (KOH) is used. Using a chemical cell, the area of the working electrode that is in contact with the solution can be controlled, as the area of the working electrode will alter the current measured.

Chapter III

Fabrication of a Biosensor

3.1 Introduction

The fabrication of the biosensor chips requires advanced tools and techniques that are approaching the limits of resolution available today. The design of the biosensor in this project requires a high surface area to achieve a strong enough signal to be detected (105). This requires features in the range of tens of nanometers. To achieve this level of fabrication, lithography techniques are widely used throughout the project. Multiple approaches were used to try meet the aims of the project including electron beam lithography, photolithography, metal deposition, etching, SAM deposition and characterisation using ellipsometry, contact angle and cyclic voltammetry.

3.2 SAM Formation

In order to produce surfaces that can be functionalized with a desired SAM modified with a DNA hairpin loop, first the deposition and formation of SAMs on the desired material must be investigated. Two surface materials were first investigated, silicon to produce surfaces with silane SAMs, and gold to produce thiol headed SAMs. With a hydroxylated surface, silane compounds form a stronger bond than that of the gold thiol bond (106), and are thermally, chemically and mechanically more stable. Silane SAMs are generally less ordered however, and the presence of water (107,108) can lead to polymerization of surface, thus increasing the difficulty of consistency in preparation.

The procedure to produce silane SAMs, shown in Figure 3.1, requires hydroxylation of a silicon surface to produce a native oxide layer. 18 by 18 mm chips from a <100> silicon wafer was cleaned in acetone and IPA, followed by UV ozone atmosphere for 15 minutes so as to break down organic compounds, sulphuric acid and hydrogen peroxide (piranha clean) at 70°C for 10 minutes, followed by a DI water rinse. Prepared surfaces were used immediately after drying with nitrogen. To create a SAM two methods were attempted, chemical vapour deposition and from solution(109).

A 1 mM solution of 3 (aminopropyl)trimethloxysilane in toluene was prepared, and the cleaned chips submerged for 30 minutes, after which the chips were rinsed in toluene for 2 minutes, IPA for 2 minutes and dried with nitrogen. Chemical vapour deposition used a self-made vacuum vessel, where a chip was inserted along with a sample of 500 µl of (aminopropyl)trimethloxysilane in an open vial, and the pressure reduced to 0.01 mBar (110) for 4 hours, after which samples were rinsed with toluene for 2 minutes, IPA for 2 minutes and dried with nitrogen.

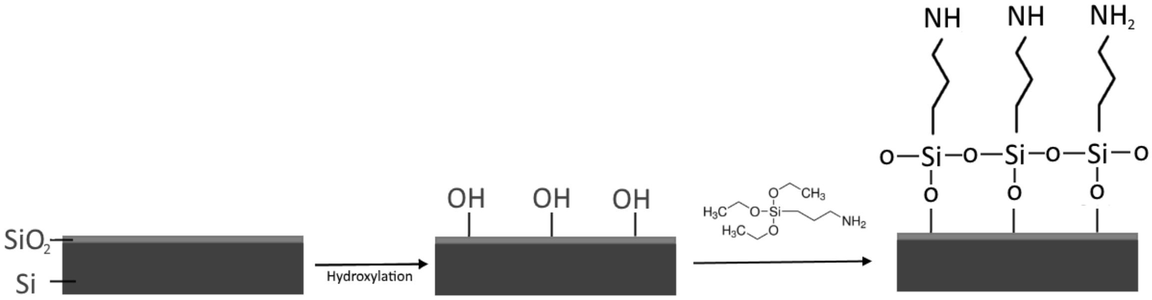

Figure 3.1 Schematic of the process of silanation of (aminopropyl)trimethloxysilane. A silicon wafer with native oxide layer is cleaned and hydroxylation of the oxide is performed, allowing a monolayer to form upon addition of a silane surfactant.

Contact angle and ellipsometry was used to characterise the resulting surfaces, the results of which are shown in Table 3.1.

	Advancing (°)	Receding (°)	Thickness (nm)
Silicon Substrate	62 ° ± 6°	60 ° ± 8	
Prepared Silicon Substrate	<10	<10	
SAM (CVD 2 hour)	40	20	1.8 ± 1.0
SAM (Solution 30 minutes)	35	24	2.65 ± 0.6

Table 3.1 Contact Angle and thickness measurements of 3 (aminopropyl)trimethloxysilane SAMs prepared by solution or chemical vapour deposition.

The lower advancing contact angle of the cleaned surface is due to hydroxyl groups on the silicon (111), which are very hydrophilic. The measured contact angles for SAMs prepared in solution of 35° is the result of the NH functional group of the SAM, and is lower than the values in literature of 44° (112), suggesting that the monolayer is not perfectly formed and may contain defects, causing a difference in wettability and thus contact angle. Further, Figure 3.2 shows that the time the CVD chamber was operated for gave inconsistent results. This may be due to the humidity and temperature of the laboratory (113), but as the solution method gave more consistent and closer results it was the preferred method moving forward.

To form a SAM on gold, a thiol head group creates a S-Au bond with the surface. A simple alkane thiol, 1-Decanethiol, 99%, containing ten carbon atoms and a thiol head group was mixed at 1 mM in HPLC grade ethanol (64).

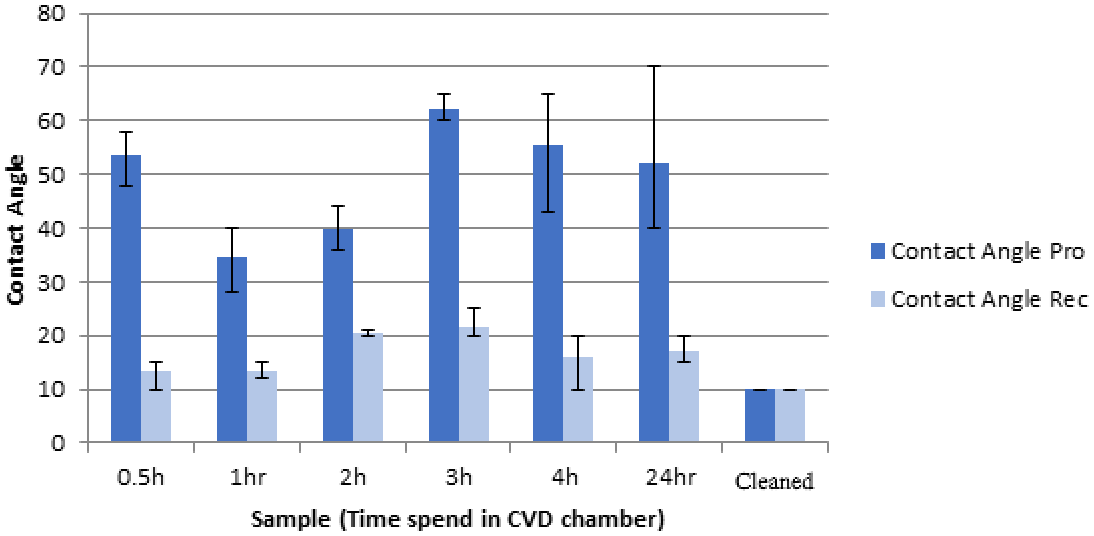

Figure 3.2 Contact angle measurements of vapour deposition of silane SAMs to a silicon based substrates with the chamber being active for different times.

Glass slides with 50 nm of evaporated gold were purchased from George Albert PVD, Germany, and contain 5 nm chromium adhesion layer. These were diced into 18 by 18 mm square and cleaned in piranha solution at 70 °C for 10 minutes, liberally rinsed with DI water and stored in ethanol before use. Samples were immersed for different times so as to determine optimal time for complete formation of a monolayer. After immersion, samples were washed with fresh HPLC grade ethanol and dried with nitrogen. Contact angles were measured as soon as possible for each sample, across 3 repeat samples. The results are shown in Figure 3.2. Inspection of the different contact angles show a slight increase of the advancing contact angle up to 2 hours of formation time, followed by a levelling out. This suggest that the film formation occurs rapidly. However, the receding contact angle keeps increase until 12 hours, where it then levels out. By looking at the difference of the two angles, the hysteresis is decreasing until 12 hour of immersion. This suggests that the order of the SAM is increasing until this point (63,64).

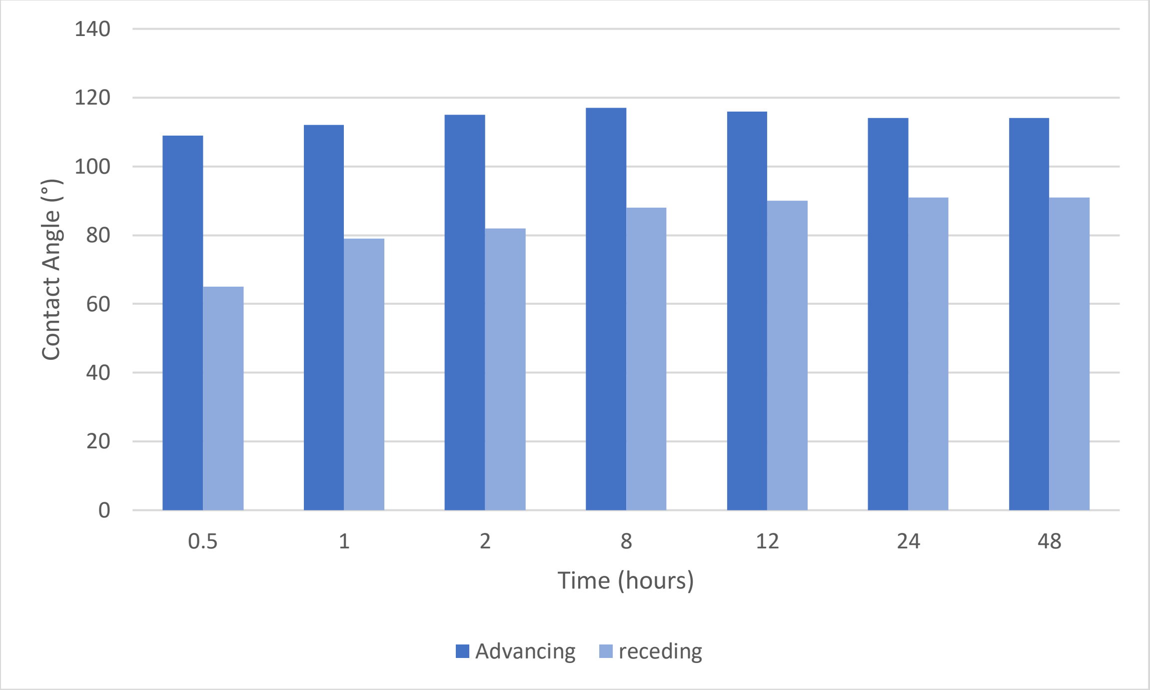

Figure 3.3 SAM formation of 1-Decanethiol on gold surfaces over a 48 period

The behaviour of different functional groups on SAMs is important, as these groups allow for different methods to attach DNA or redox functional groups. The SAMS used are: 1-Decanethiol (DT) an alkane, 11−mercapto−1−undecanol (MUT), an OH terminated group and 11−aminoundecanethiol hydrochloride (AUT), an NH_2 terminated group. The chemical structures of these are shown in Figure 3.4.

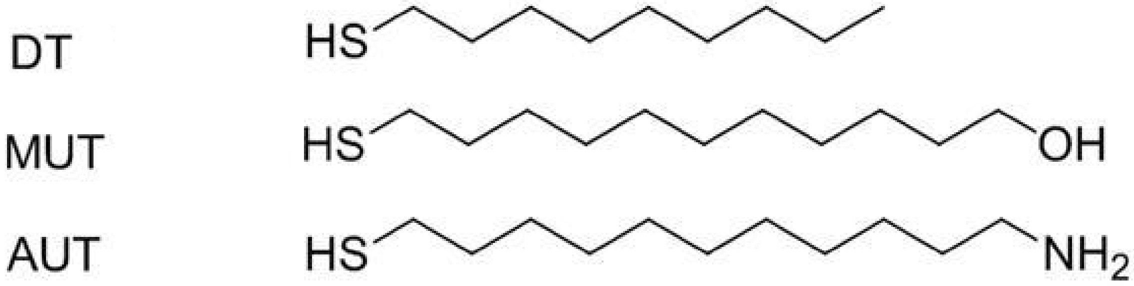

Figure 3.4 Chemical structure of different thiol SAMs

Table 3.2 shows the contact angle and ellipsometry result of different SAMs on gold samples (50 nm gold on glass), all of which were submerged in solution for 12 hours. The thickness was measured by ellipsometry, and theoretical thickness is based on the length calculated in the software Chem 3D. The experimental values are similar to literature data (64).

	Advancing (°)	Receding (°)	Thickness (nm)	Theoretical (nm)
Gold Surface (cleaned)	74	69		
DT	116	90	1.73	1.3
MUT	29	15	1.5	1.5
AUT	64	22	1.43	1.5

Table 3.2 Contact angles and ellipsometry measured thickness of different SAMs on gold surfaces.

3.3 Design of an Interdigitated Finger Based Biosensor

The design of a lab on chip type biosensor requires an area where transducer event can occur i.e. an area where the biological interaction between the bio-recognition molecules and their target occur, and an area where that signal can be detected.

In this project, the design and fabrication of a device to achieve a specific set of conditions to allow future work to continue was outlined early on. The sensor is designed to detect electrical current at multiple surfaces caused by conformation change of aptamers or similar biorecognition molecules. Interdigitated fingers were chosen to as to have two close but isolated electrodes with a known gap between them, and a large surface area. Difference in electrochemical signals, obtained by cyclic voltammetry, can be processed using external electrochemical equipment. Figure 3.5 shows the top-down design of an individual area of the chip, showing that for each area of interaction there will be four electrodes. Electrodes are from the metal surface (SUR), and from reference electrode (REF) and the active electrodes (1 and 2) at the higher level, from the top of the interdigitated fingers.

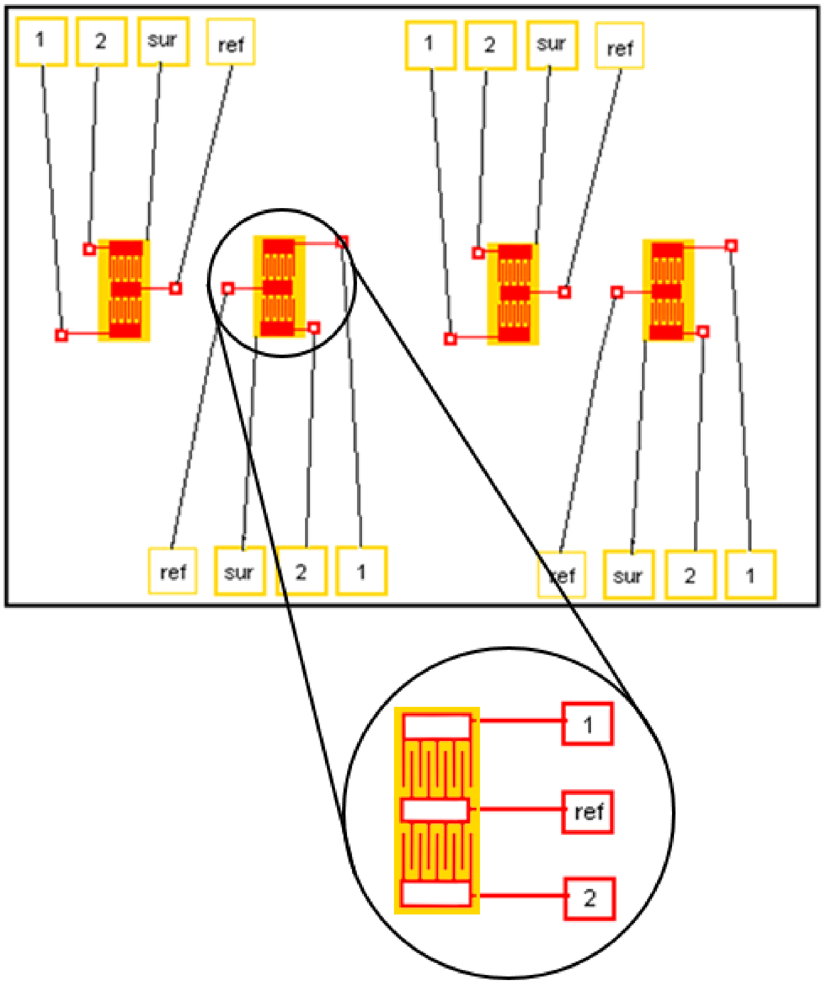

Figure 3.5 Schematic of the biosensor design including four different areas of interaction and their electrodes. The enlarged are shows the layout of a set of interdigitated fingers.

To avoid confusion, the centre area of a chip, where biological reactions occur, will be referred to as surface electrodes and raised electrodes, and the connections to the side of the chips as the pads and wires. In this initial design, multiple sets of electrodes and pads on a single chip allow for simultaneous detection of multiple targets. Figure 3.6 shows the cross-sectional view of a single electrode made from gold, silicon dioxide (SiO_2) and Aluminium with the bio-recognition molecules to be tethered on the gold surface. These molecules are thiol ended aptamers or single stranded DNA with a redox group as discussed in chapter 1, spaced out evenly on the surface., between the electrodes. Aluminium was chosen for the raised electrodes to prevent deposition of the bio-recognition molecules on the raise electrodes.

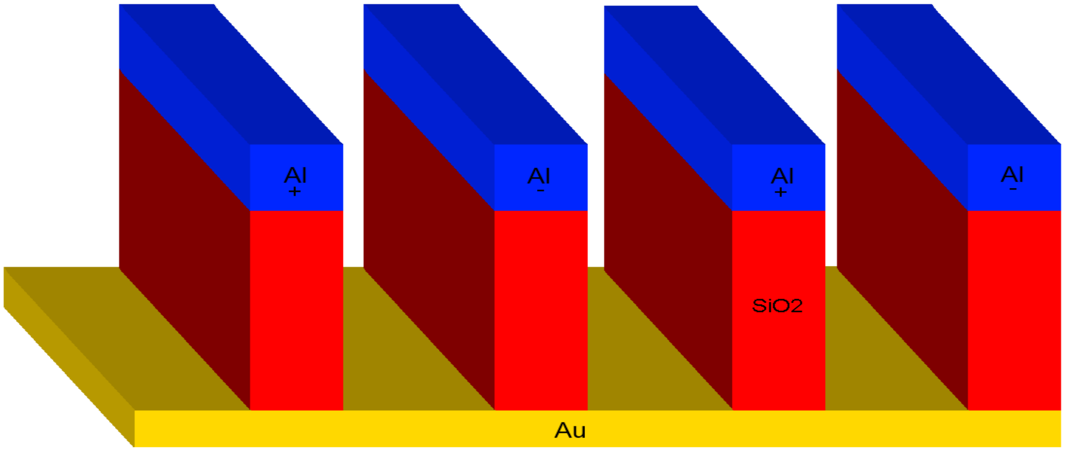

Figure 3.6 Cross section view of a set of interdigitated fingers (Gold and Aluminium) with a dielectric layer of silicon dioxide. Fingers labelled (Al+) and (Al-) are electrically isolated from one another, and from the gold surface.

Figure 3.7 shows how the conformational change of the bio-recognition molecule, in this case on matching with a conformational strand of DNA, causes the electrically active end group to move from proximity of the surface electrode to proximity with the raised electrode. The proximity of the redox group to each electrode at different times, upon an electrical potential, will change a measured signal from the surface. In this design, a measured signal can would change across two different electrodes simultaneously as the redox group moves away from one surface and towards the other, which is designed to decrease any false positive reading caused by stray interactions at either electrode or due to undesired detachment of the bio-recognition molecule.

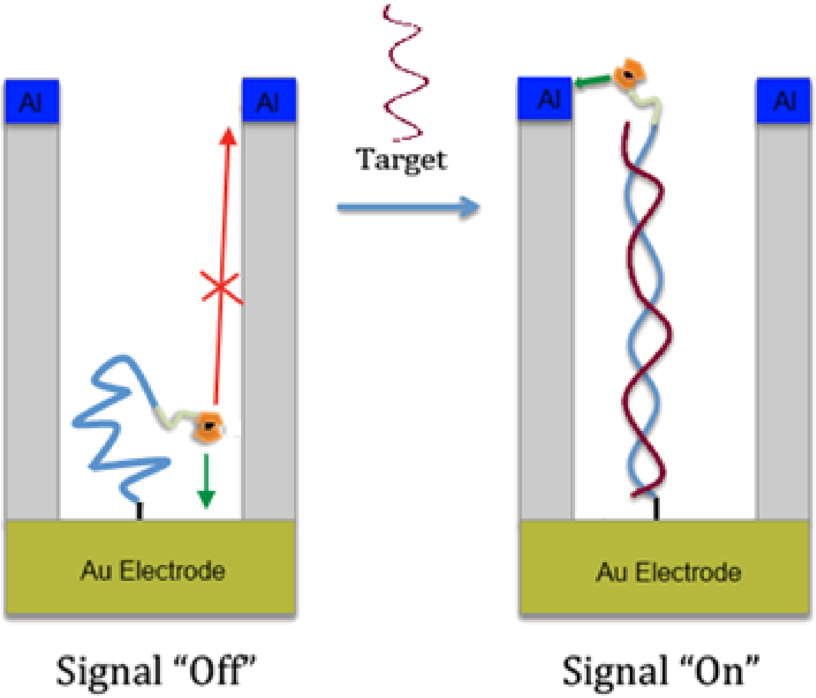

Figure 3.7 A redox end group on a single stand of DNA At rest this is close to the gold surface, but conformational change of upon addition of complementary strand of DNA changes the electrical properties of both surfaces due to the location of the redox group.

The two different surfaces must be separated by a sufficiently insulating material so that each surface is electrically isolated from the other. Furthermore, the dielectric constant of the separating material must be suitable to allow capacitance to be used as a detection method. The thickness of this material is to be such that the conformational change of the bioreceptor molecule, upon bonding with the target, can cause the electrically active end group to move from the surface to the raised surface. Aptamers, the final choice of recognition molecule that this project is aiming towards, have a length dependent on the number of base pairs. A typical aptamer may have as few as 50 base pairs (114), and with a single base pair being 0.3 nm, this corresponds to a length of ~20 nm, giving the maximum target height for this layer, although it is desirable for the dielectric layer to be thinner should it still be sufficiently electrically isolating, as this will simplify fabrication of the surfaces.

3.3.1 Fabrication Process Schematic

The fabrication process to create the design described in section 3.2 is a multistep process and requires use of multiple fabrication methods. The major parts of the process are outlined in Figure 3.8, and require lithography for patterning, metal deposition and chemical SAM deposition. Results and challenges of this process are discussed in the rest of this chapter.

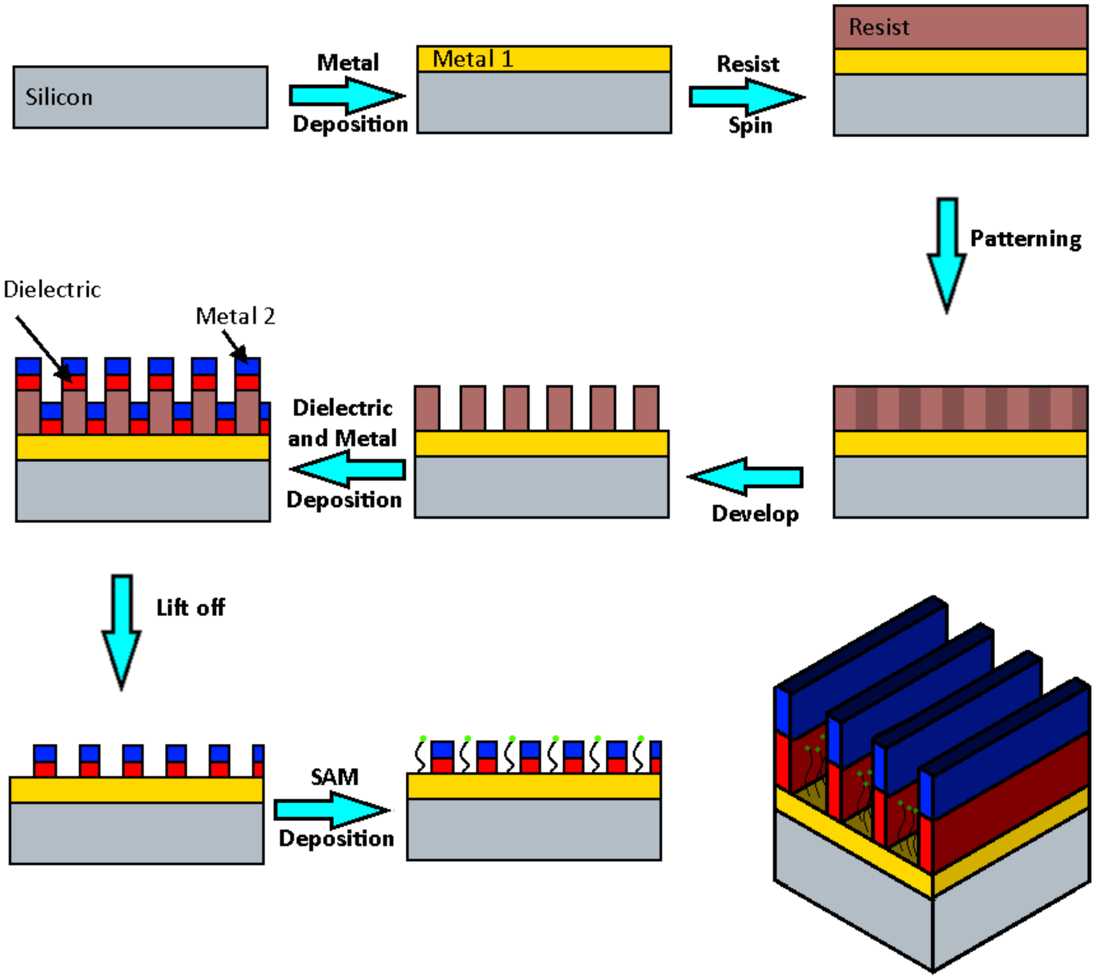

Figure 3.8 Fabrication process schematic from silicon substrate to raised electrodes.

3.4 Electron Beam Fabrication with SML Resist

To create patterns with sub micrometre resolution, it is often necessary to use e-beam lithography to create initial patterns on a substrate. These patterns can then be transferred to a photomask should mass production of the design be required, but in the design and experimental stage Ebeam gives the user flexibility and control over the design. PMMA is a well-known and highly used Ebeam resist and suitable for lithography at both high and low resolutions. However, PMMA has an aspect ratio limit of 4:1 after which proximity effects can lead to difficulties in development and lift-off (115). It is desirable to use high aspect ratio structures to aid in lift off, and to allow a thicker top electrode in the metal deposition stage, and so alternatives resists which can support a higher aspect ratio and aid in easier lift off were examined. Figure 3.9 shows a computer simulation of how the low energy secondary electrons widen the intended width of the pattern, as well as creating a profile through the resist that will give poor results in metal deposition.

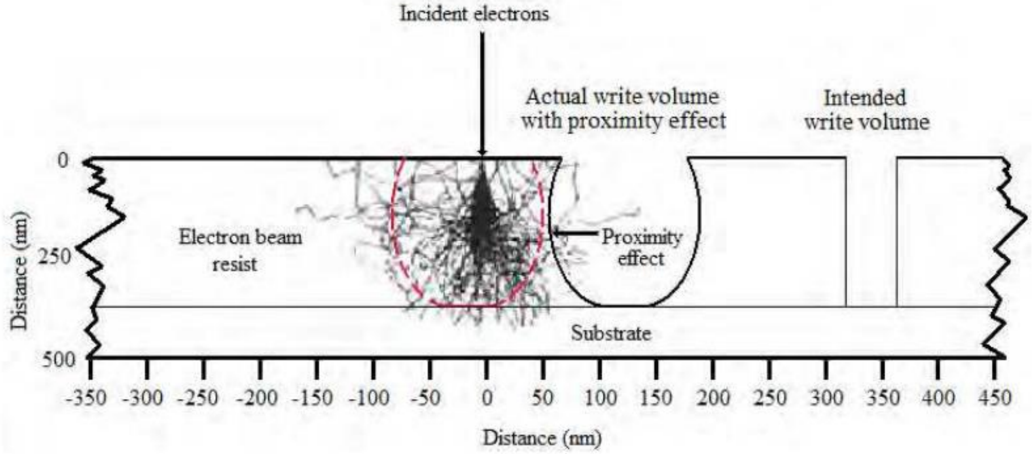

Figure 3.9 Proximity effect demonstrated in Monte Carlo simulation. Image from ref. (115)

In this project, dense features at 20 – 25 nm thickness and similar half pitch were ultimately desired so as to increase the surface area of the raised electrodes and thus have a stronger signal. To ensure good coverage and a well-defined top electrode, a thickness of metal of > 50 nm was required, with a dielectric layer thickness, depending on material, of > 20 nm. The aspect ratio of PMMA at 4:1 would allow for a film thickness of 100 nm at this scale, which could cause difficulties with lift-off of > 70 nm deposited material. Furthermore, without regular access to a 100 keV ebeam lithography, patterning in PMMA can lead to difficulties with wall profile, leading to poor metal deposition and short circuits in the lift off step. The XL30 ebeam tool used throughout the project has a maximum beam energy of 30 keV. An alternative resist by EM Resist (116) and in development at the University of Manchester is called SML, based on PMMA but with additives to improve its function, it is both a photoresist and an EBL resist.

The mechanics behind the differences between the resists are discussed in the work by Scott Lewis (117), and will not be explained in great detail here, but this can be summarised as that due partially to the lower density of the SML resist there are less primary electron scattering laterally leading to a reduced generation of secondary electrons that would otherwise expose the resist via the proximity effect. Figure 3.10 highlights the difference in computer models of resist patterning in PMMA and the dye-enhanced resist SML, at both 30 keV (available throughout this project) and 100 keV. The cleaner profiles of the SML suggest that it is a more suitable choice of resist and would lead to better patterning results, however the simulations had not yet been verified in practice for film thickness between 100 – 600 nm.

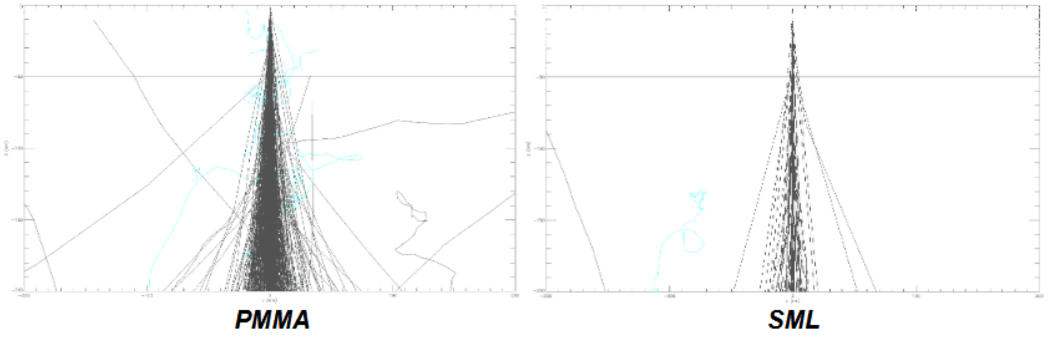
Comparison of 50nm thick PMMA & SML on Si substrate exposed @ 30keV

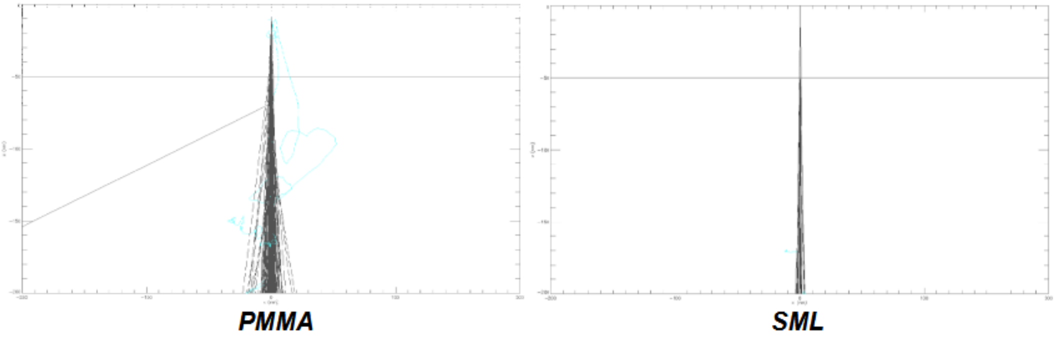
Comparison of 50nm thick PMMA & SML on Si substrate exposed @ 100keV

Figure 3.10 Monte Carlo simulations of PMMA and SML resist at 30 keV and 100 keV.(118)

3.4.1 SML 300 and 600 Exposure

The SML resist is available to spin in different thickness. In this work, in collaboration with Scott Lewis at the University of Manchester, SML 100, 300 and 600 were provided by EM Resist to spin films between 100 nm and 1 µm in thickness. Figure 3.11 shows the spin speed curves used, to create various film thickness. Wafers of silicon were diced into 18 mm by 18 chip and spun with SML resist to the desired thickness. Post application bake (PAB) soft bake was 180°C for 120 seconds.

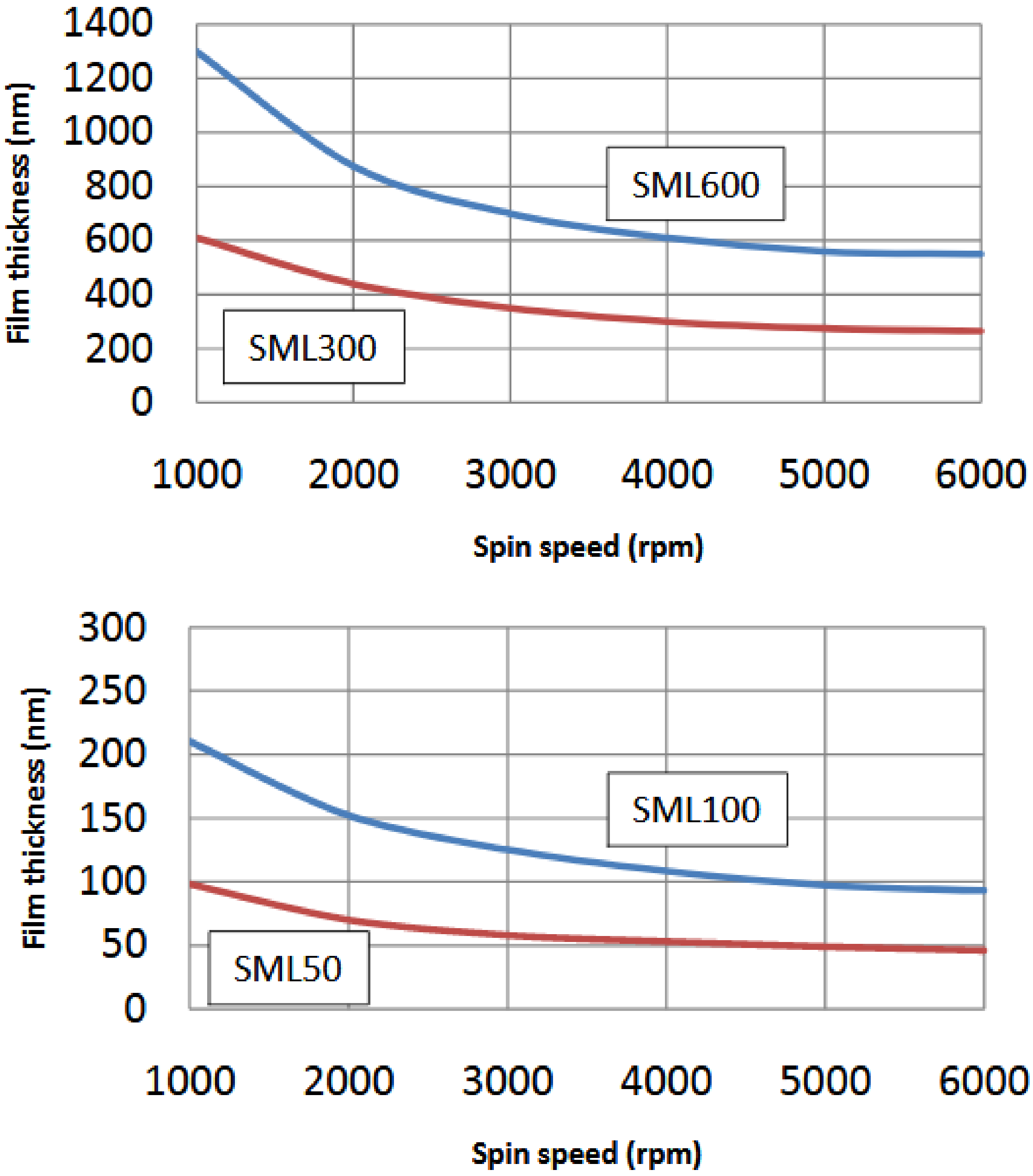

Figure 3.11 SML spin speed curves for SML resist (118)

Exposure parameters were a beam current of 20.6 pA with a dose of 2081.3 µC/cm^2, an area step size of 3.1nm, Dwell time of 0.000924 ms and beam speed of 3.355 mm/s. PMMA (A8) was purchased from Microchem and exposed at 1500 µC/cm^2 with the same beam parameters for comparison. The GSDII file used for exposure was designed for arrays of 20 nm thick lines at 800 nm pitch in a 100 µm write field, as single pixel lines were not used due to software issues with the tool, where upon the beam would overexpose the start of each line.

Using this method, the resulting pattern is of lines of minimum thickness that expose completely through the resist. Both resists were developed using a solution of MIBK (methyl isobutyl ketone) and IPA (isopropanol), in the ratio of 1:3, for 30 secs followed by 15 secs rinse in IPA and a blow dry with N_2.

After development, chips were cleaved across the patterns so that cross sectional images could be taken. The images, shown in Figure 3.12 and Figure 3.13 were taken at a tilt of 70° in the XL30. The profiles of the two resists show straighter side walls with exposure of SML resist compared to PMMA, supporting the computer simulations. With a thickness of 620 nm for PMMA and 635 nm for SML, aspect ratios were calculated at ~ 4:1 and ~ 9:1 respectively. This proves that using SML resist can lead to both steeper wall profiles and support higher aspect ratios, as required for this project, compared to PMMA. SML 100 was used going forwards. In discussion with Scott Lewis, it was theorised that more elastic collisions in the PMMA resist result in increased secondary electron generation, and a higher number of scattering events compared to SML, and that this effect is highest at low >30Kev beam energies.

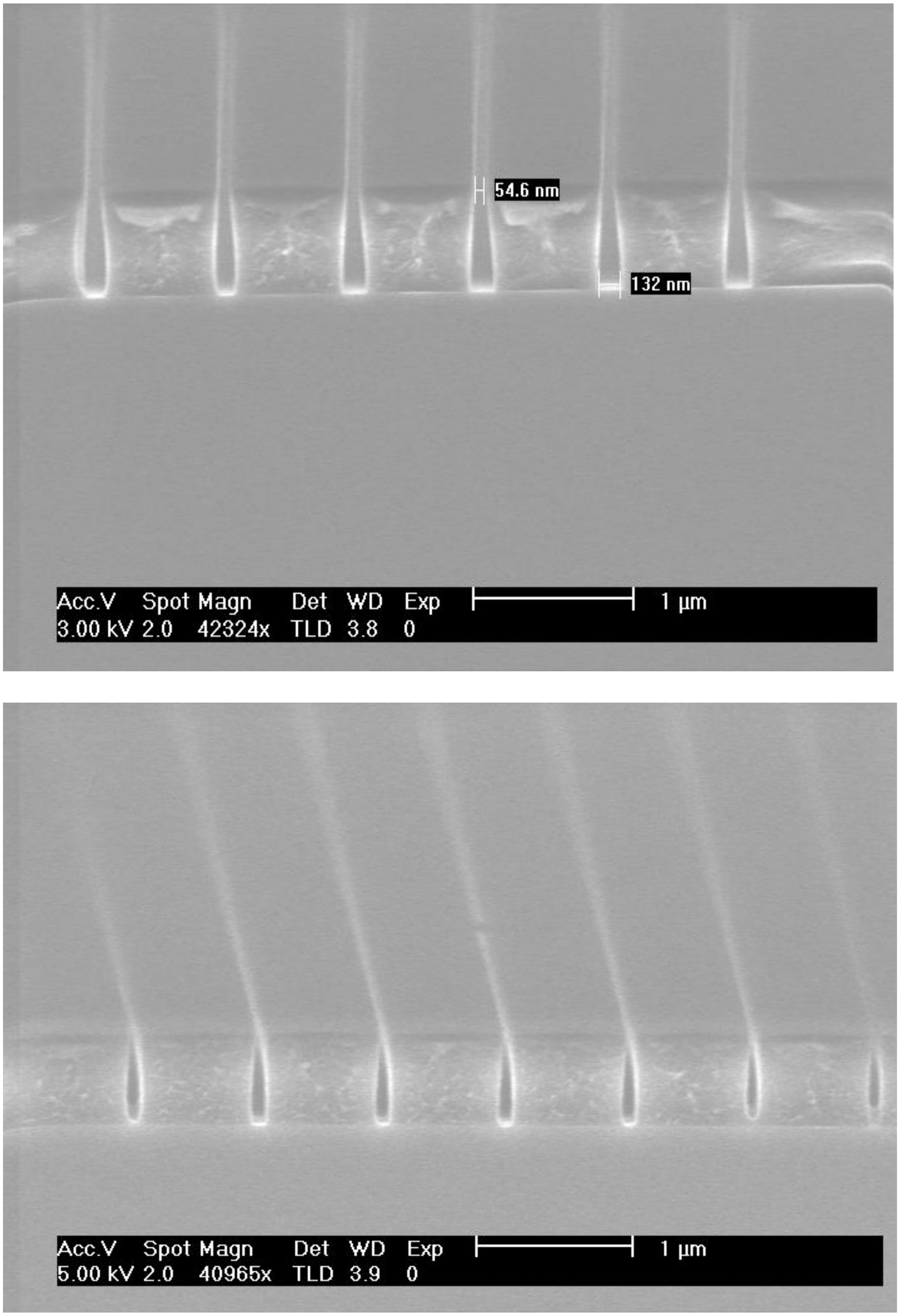

Figure 3.12 PMMA patterned with 130nm trenches on 800nm pitch (top) SML patterned with 65nm trenches at 800nm (Bottom). Thickness of both resists are 600 nm. Exposure dose 2083 µC/cm2.

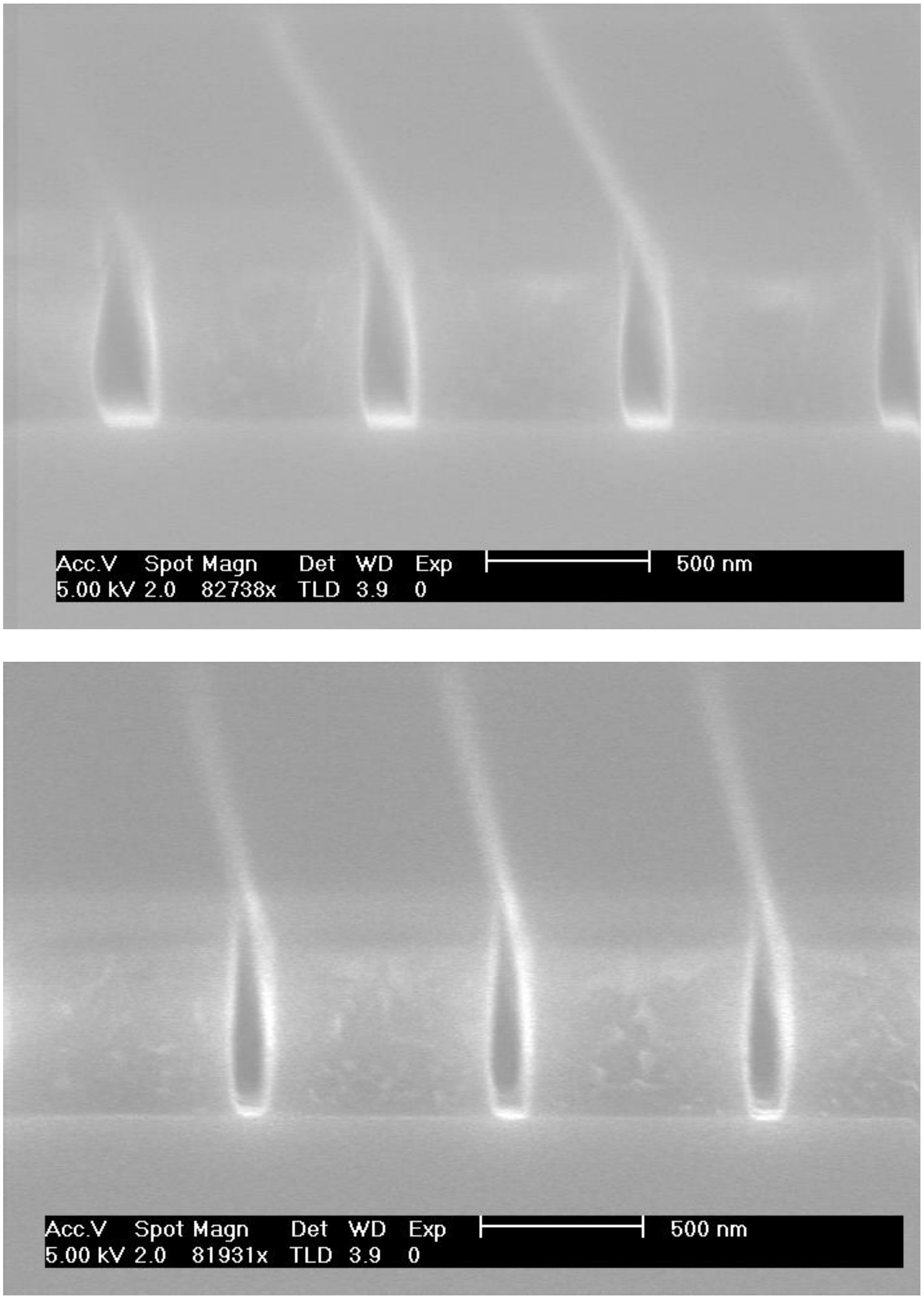

Figure 3.13 Zoomed in micrograph showing the negative wall angle profiles caused by the proximity effect in PMMA (top) and SML600 (bottom)

3.5 Choice of Materials

Initial attempts to lithographically pattern dense patterns lines were performed in collaboration with the University of Glasgow. The design of the surface is shown in Figure 3.14, consisting of a multi-electrode setup, two experimental electrodes and a centre common electrode in aluminium, and a surface electrode in gold. By having a design with multiple electrodes, future work using impedance difference could be considered (119).

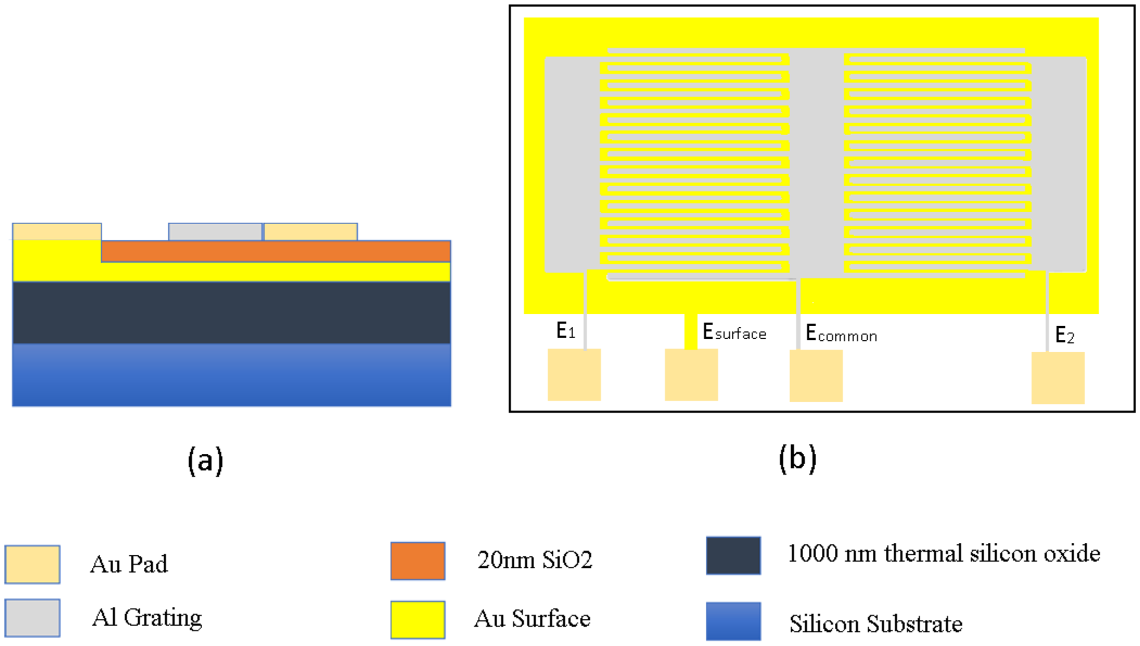

Figure 3.14 Design process schematic showing a) cross sectional view and b) top down view of a multi electrode setup.

Using Vistec VB6 UHR EWF electron beam lithography tool at 100kv, the procedure for creating grating areas was carried out;

1. Deposition of a layer of Au 100 nm (thermal evaporation)
2. Spin a Bi-Layer of PMMA

3. Expose pattern on VB6
4. Develop pattern
5. Deposition of Dielectric ICP/evaporation to 20 nm
6. Deposition of Al 50 nm
7. Lift-off and removal of resist
8. SEM inspection (top down)

The maximum dimensions of the lines achieved were 100 nm on a 300 nm pitch, shown in Figure 3.15. Attempts at a higher resolution than this failed to have acceptable patterning over the whole grating area. The lines were patterned in PMMA, with a silicon substrate and gold surface layer beneath the gratings, 20 nm CVD layer of SiO_2 as the dielectric and aluminium as the top layer.

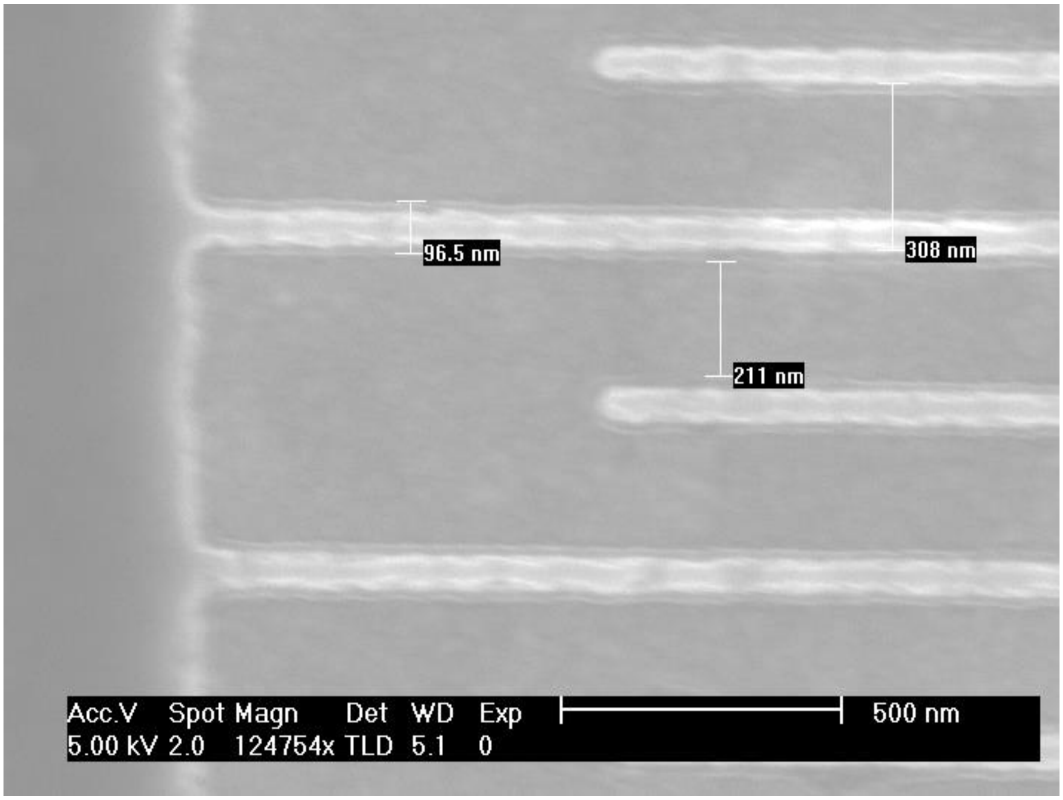

Figure 3.15 ~100 nm lines on a 300 nm pitch. The lines (bright) show gold and the surface is aluminium.

The results in this experiment showed that even with a 100kev ebeam tool, producing the very high resolution structures desired was challenging due to pattern collapse experienced. The Gold-Silicon oxide-aluminium chips were made ready for electrochemistry using gold wire bonding performed on a Delvotec 5430 using and 25 µm wire on the pads. The chip was mounted to a PCB and the grating part submerged in a three-probe cyclic voltammetry cell as shown in Figure 3.16 and Figure 3.17. All CVs were recorded in the presence of 1 mM ($K_3Fe(CN)_6$ in 1 M $NaPF_6$, 100 mM sodium phosphate.

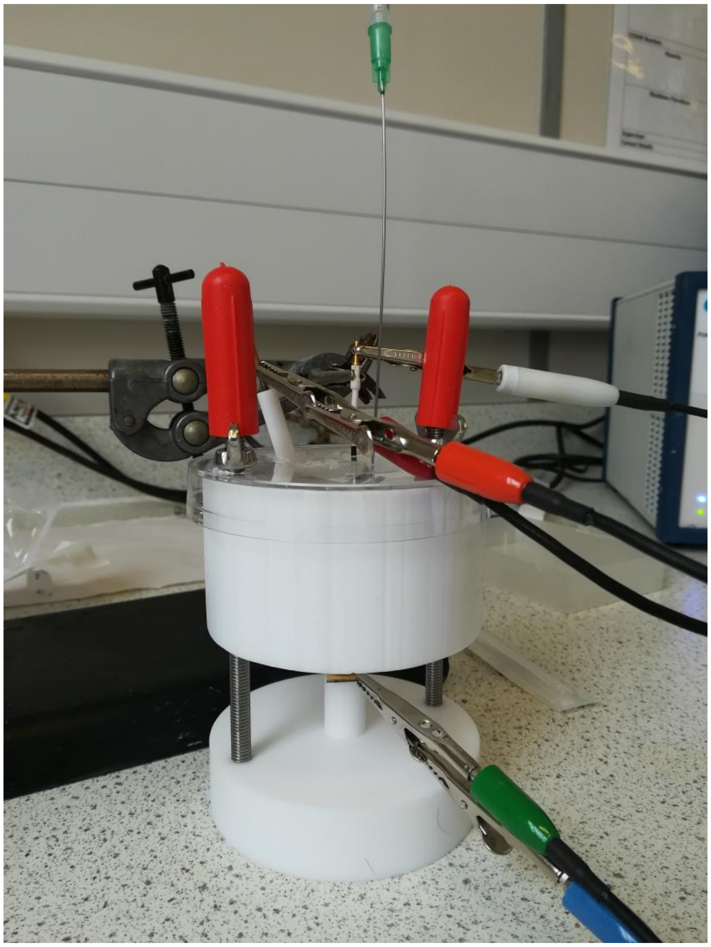

Figure 3.16 Cyclic voltammetry cell used, allowing a set diameter of the surface of the chip to be submerged (120)

However, it was determined that the biochip design was flawed as the aluminium was damaged in electro chemistry. It is thought that the aluminium was electrically removed (121) during cyclic voltammetry tests as shown in Figure 3.18.

Whereas the gold part of the chip performed as expected, with a cyclic voltammetry response typical for gold, the aluminium showed no known response curve. Therefore, the decision was made to create both the surface and raised part of the grating in gold.

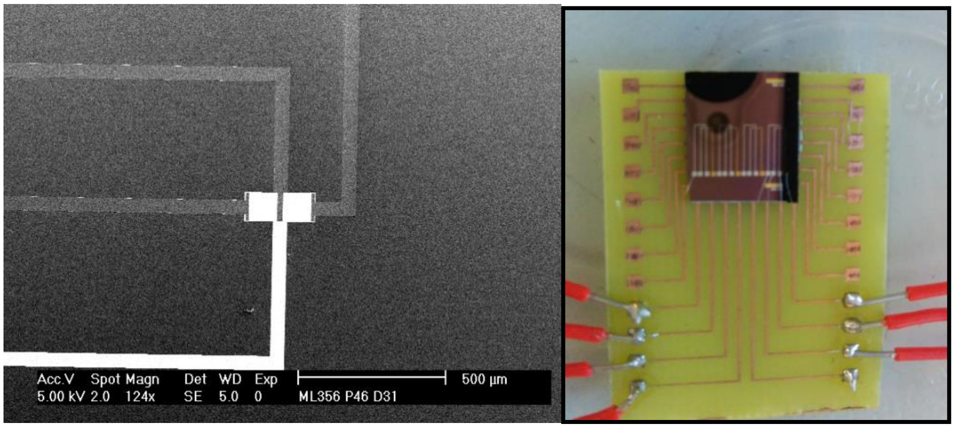

Figure 3.17 The grating area of the gold-silicon oxide-aluminium chips (left), the chip wire-bonded to a PCB ready for electro chemistry.

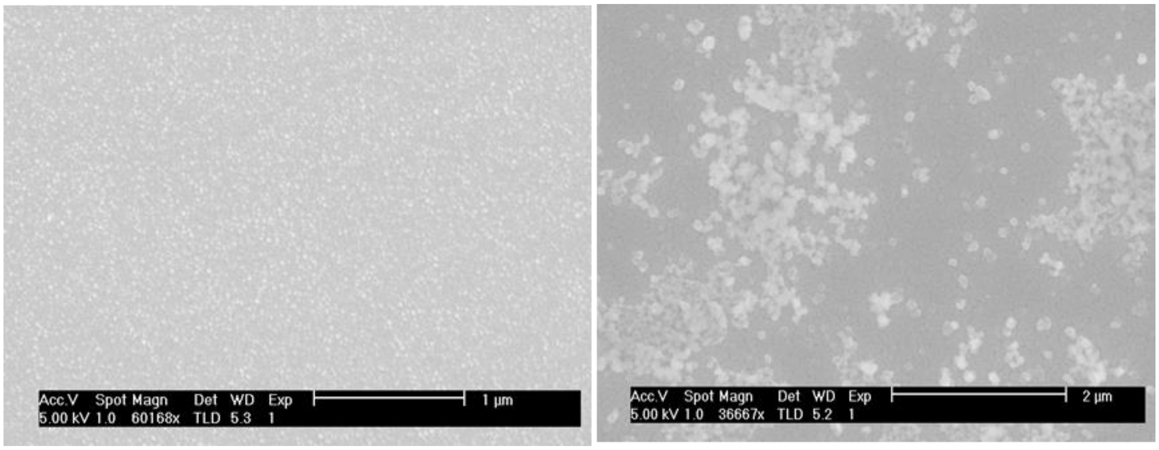

Figure 3.18 Aluminum surfaces (a) before and (b)after electrochemistry. Showing the removal of aluminum form the substrate after electrochemistry.

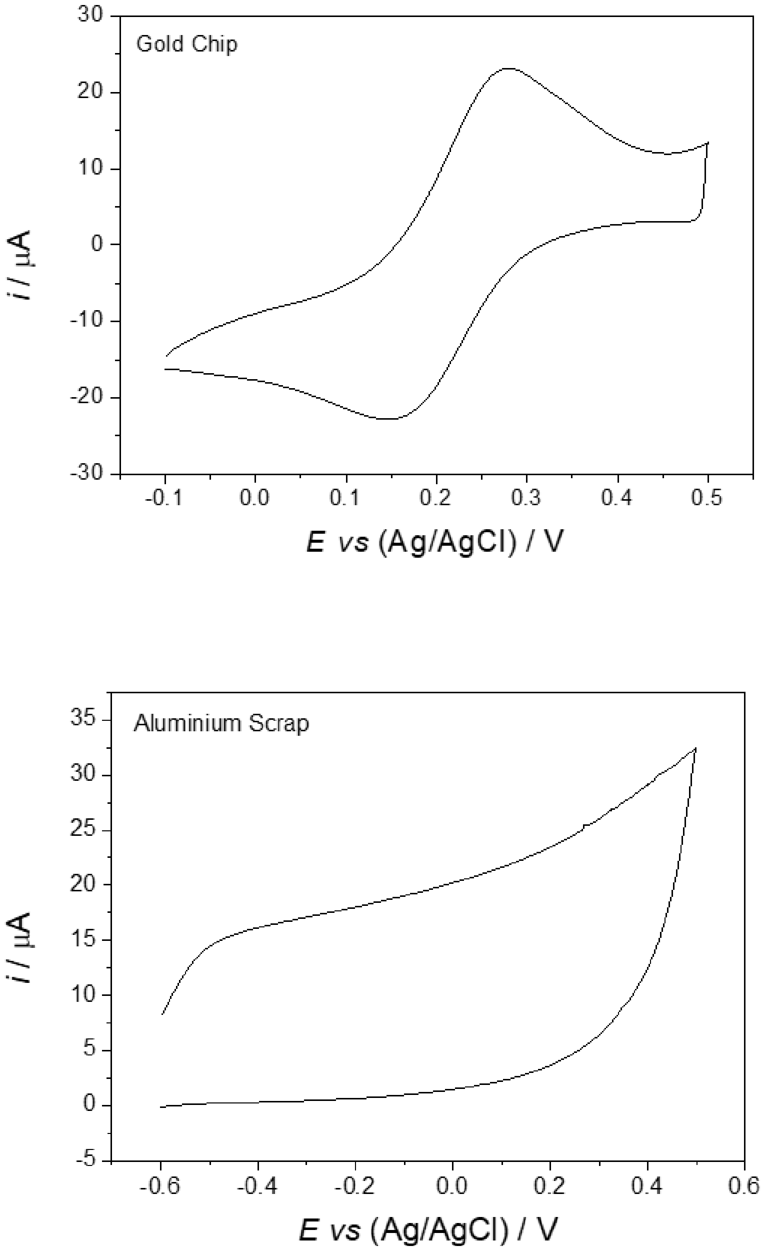

Figure 3.19 Cyclic voltammetry response of gold (top) and aluminium (bottom) against a silver-silver chloride reference electrode. The top voltammogram shows an expected curve for gold, but no peaks in the aluminium curve suggest redox reactions are not taking place at the surface.

3.5.1 Two Gold Surfaces

Using a gold surface and raised gold surface set up, shown in Figure 3.20 ,has its advantages; repeating the metal deposition steps would become simpler as gold for both the surface and raised part of the grating can be deposited in the same way, and the electrochemical behaviour of gold is well studied (122–124).

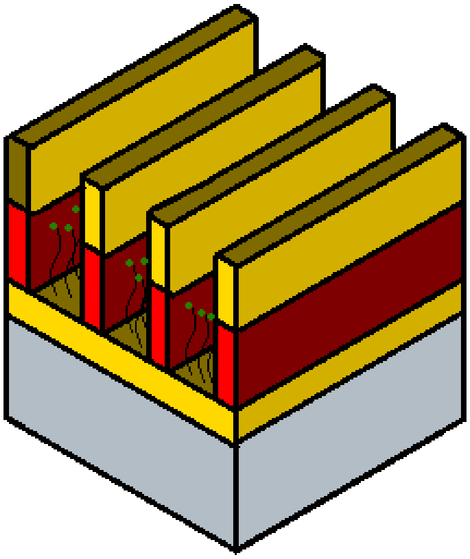

Figure 3.20 Schematic of the raised electrode structure using two layers of gold.

However, deposition of the thiol SAMs and thiol terminated recognition molecules would become more complex, as there would be no way of confining the locations of the SAMs to only the surface electrode as both electrodes are gold. Studies by Fisher et al (125) show that multiple methods for cleaning gold surfaces with different reagents, but also using potential sweep giving top cleaning results from the various methods. The potential sweep method of cleaning gold was reported by Heiskanen et al (126), using 50 mM solution of potassium hydroxide (KOH) with the gold electrode connected to a potentiostat, a -200 to -1200 mV (vs Ag/AgCl) sweep is used to clean the gold. This was investigated as a method of selectively cleaning a surface.

SAM of 1-Decanethiol were deposited onto glass chips with a 50 nm gold layer. Gold was cleaned in piranha solution at 70 °C for 10 minutes, liberally rinsed with DI water and stored in ethanol before use. Samples were immersed for 12 hours to allow formation of a monolayer. After immersion, samples were washed with fresh HPLC grade ethanol and dried with nitrogen. Presence of monolayer was confirmed by contact angle and ellipsometry. Cleaning of gold was performed using the potential stat method used by Heiskanen et al (127). A solution of 50 mM KOH was prepared, and samples were submerged. A linear sweep from -200mv to 1200mV was used, repeating the sweep 3 times to ensure the SAM has been removed. CV of each samples before and after treatment are shown in Figure 3.21. CV was carried out with a Ag/AgCl reference electrode, platinum wire counter electrode, performed in 1M KCl with 2mM K3[Fe(CN)6]/K4[Fe(CN)6]   It can be seen that before cleaning, a characteristic CV of a non-charged SAM surface is present (128), that inhibits redox reactions at the surface. After cleaning, a characteristic bare gold curve was seen (129), which shows the SAM was removed successfully. Control chips which were not wired to the potential stat were not significantly changed.

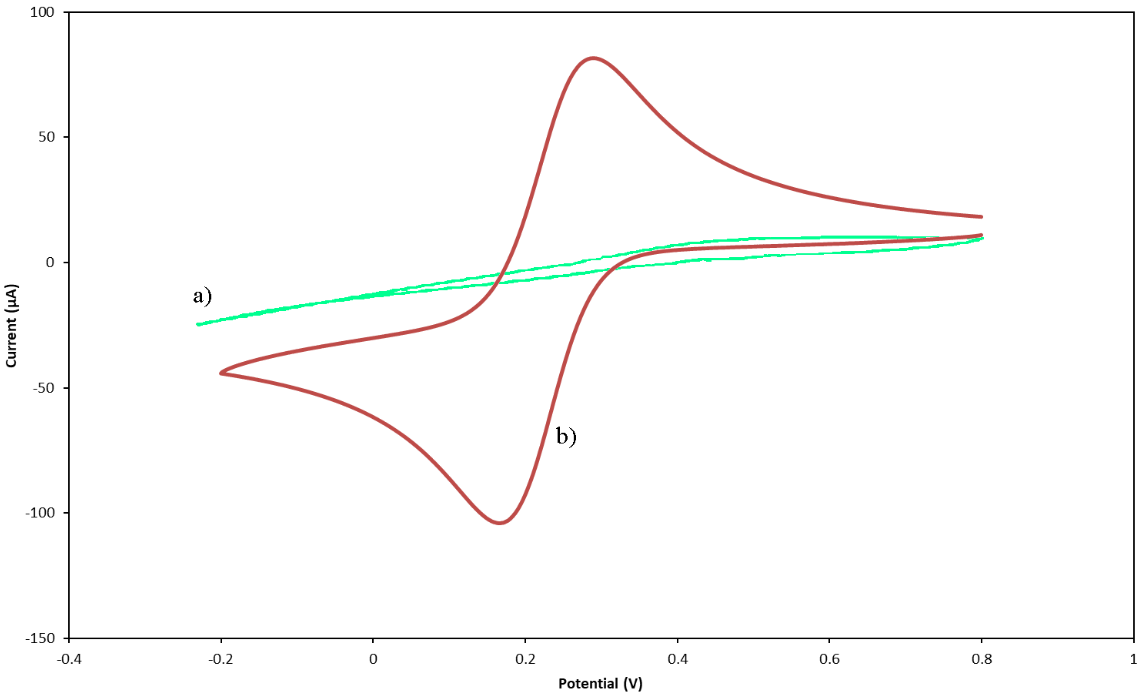

Figure 3.21 Cyclic voltammogram performed with 2mM K3[Fe(CN)6]/K4[Fe(CN)6] with 1M KCl as supporting electrolyte. It shows the CV of a gold SAM of 1-Decanethiol a) before and b) after linear sweep cleaning.

3.6 Patterning Interdigitated Fingers

SML100 was spun to 100 nm on gold coated silicon, and patterning was performed on the XL30 at 30 keV, with development in MIBK:IPA at a 1:3 ratio. Prior to spinning an adhesion layer of chromium was sputtered at 300 W for 30 secs with a chamber pressure of 6 $\times 10^{-6}$ Pa and argon pressure of 1 $\times 10^{-2}$ Pa, followed by a 200 nm layer of gold, sputtering at 100 W for 6 min 30 seconds.

The resulting lines on a 1:1 pitch were 45 nm, lines were patterned at 100 nm pitch with an aspect ratio of ~ 2:1, as shown in Figure 3.22. As the dielectric and second layer of metal is to be deposited in the spaces, the most important dimension is the gap between the metal features rather than the width of the metal lines, although thinner metal lines would allow for a stronger signal overall due to the density of the packing.

As aptamers were to be spaced evenly among the SAMs in the gaps, and only those close to the metal walls would produce a signal on the raised metal, so minimising the resist width in patterning was the priority. A method of over exposing the resist features allows for a narrower resist profile, as shown in Figure 3.23 achieving a pattern of down to 22 nm on a ~130 nm pitch. However, in the image shown it can be seen that the thickness of the resist is reduced significantly to ~75nm, and this led to difficulties in metal deposition.

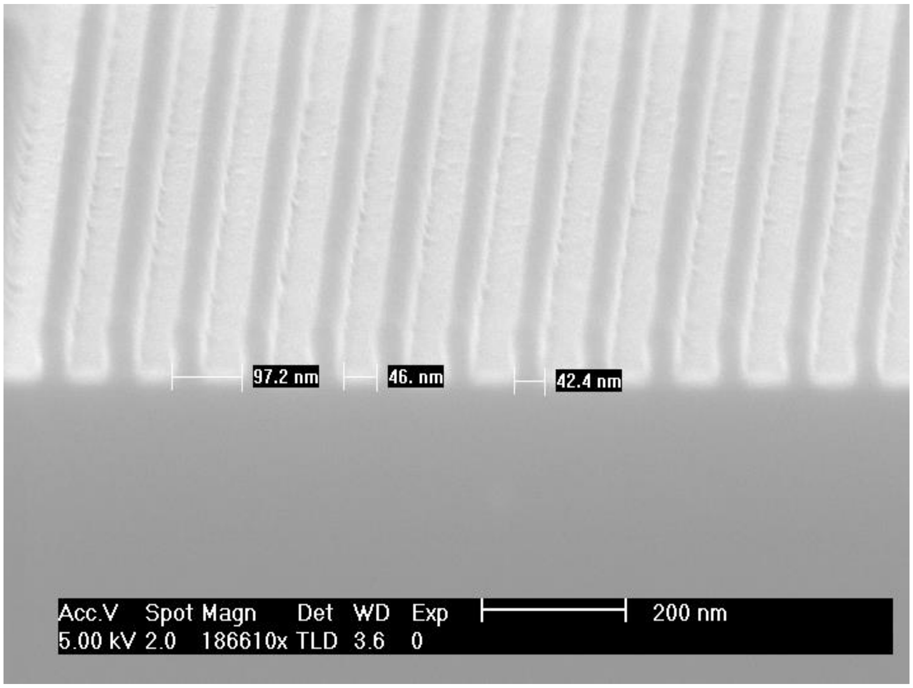

Figure 3.22 patterns in SML resist showing 46nm spacing on a 100nm pitch

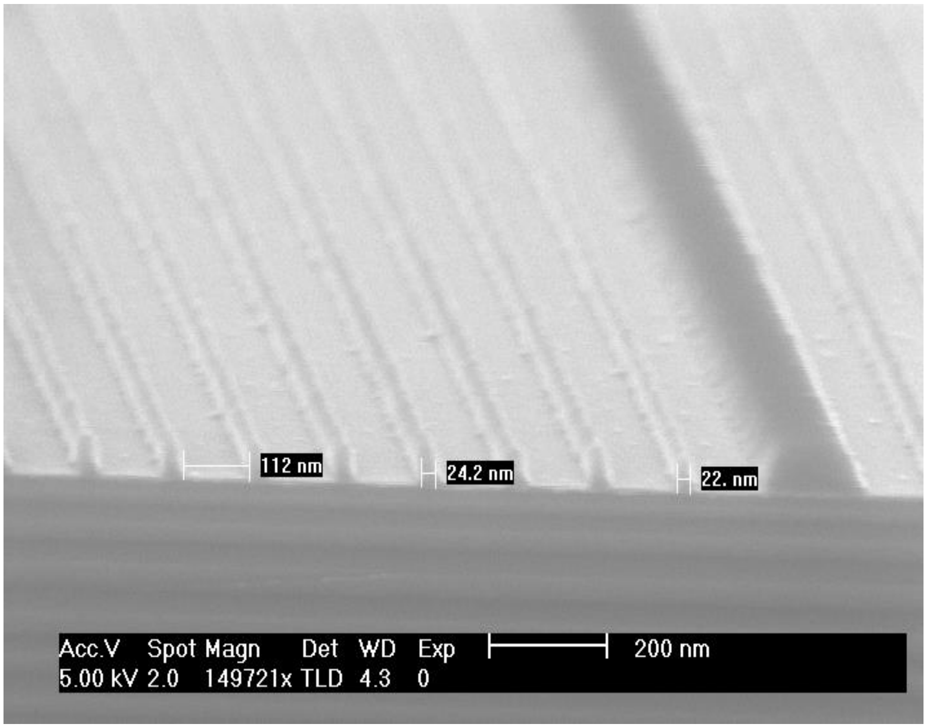

Figure 3.23 SML100 over exposure produced 22nm patterns at a cost of reduced thickness in the resist.

To transfer the pattern, a dielectric layer of 20 nm SiO_2 and a gold layer of 50 nm were deposited by sputtering, including a thin (< 10 nm) adhesion layer of chromium. Thickness of deposited material were determined by deposition of materials at a given condition onto a chip patterned with a resist pattern of a 100 µm square area. Upon deposition of material, the resist of removed leaving a square of material, and the height measured by dektak. Evaporation of gold is often the best choice for metal deposition and lift off as isotropic sputter processes can lead to coating of the side walls of the resist. However, the Edwards 306 auto sputter had the advantage that three targets could be used without needing to vent to atmosphere, greatly simplifying the process of building the structures. Annealing the gold at elevated temperatures of up to 400 °C was attempted to improve the roughness and structure of the gold(130).

By using the sputter coating, after resist patterning, the dielectric layer, chromium adhesion layer and gold top layer could all be performed in series without requiring venting to atmosphere. Sputtering also allowed the use of a new dielectric, hafnium oxide (HfO_2), which cannot be evaporated except by electron beam evaporation(131). This has a higher dielectric constant (k) compared to SiO_2 which leads to a thinner layer being required to achieving the same function.

Table 3.2 compares different materials that were available with our sputter coater along with their dielectric properties. By switching to HfO_2, a thinner separating layer of just 10 nm can be used potentially aiding in lift-off and reducing the feature size.

Material	Dielectric Constant k	Gap (eV)
Si	-	1.1
SiO2	3.9	9
Al2O3	9	8.8
HfO_2	25	5.8

Table 3.3 Dielectric constants and bandgaps of materials available (132)

Lift-off of metals after sputtering was achieved by submerging the chip in acetone for 30 seconds along with gentle agitation to completely dissolve the remaining resist and remove metals on top of the resist. For large features such as pads and connecting wires this method was sufficient, although fine features often required an ultrasonic bath in acetone for between 20 – 120 seconds. Lift-off of the very finest patterns was not achieved without significant bridging or damage to some areas of the grating as shown in Figure 3.24. Other methods of lift-off that were attempted included creating a bilayer out of two different molecule PMMA(133). Two films of PMMA were created from solids of molecule weights 495K and 120K (narrow range) purchased from Sigma Aldrich. Solutions of 2% solid (w/w) of each were made in anisole solvent (HPLC grade). The 120K was spun at 3000 RPM (50 nm film), and following a 1 minute, 180°C prebake, the 495K solution was spun on top, at 3000 RPM, prebake of 150C for 1 minute. Exposure on the SEM was performed within the normal dose ranges and patterns. The bi layer process gives a pronounced undercut, which aids in lift off (134) after metal deposition. Unfortunately, whether with bi layer resists or SML, only in the case of less fine features was lift-off successful across chips at 50 nm lines / 200nm pitch as shown in Figure 3.25. An alternative process of etching patterns was considered to avoid the problems encountered with the lift-off of patterns, and is discussed further on.

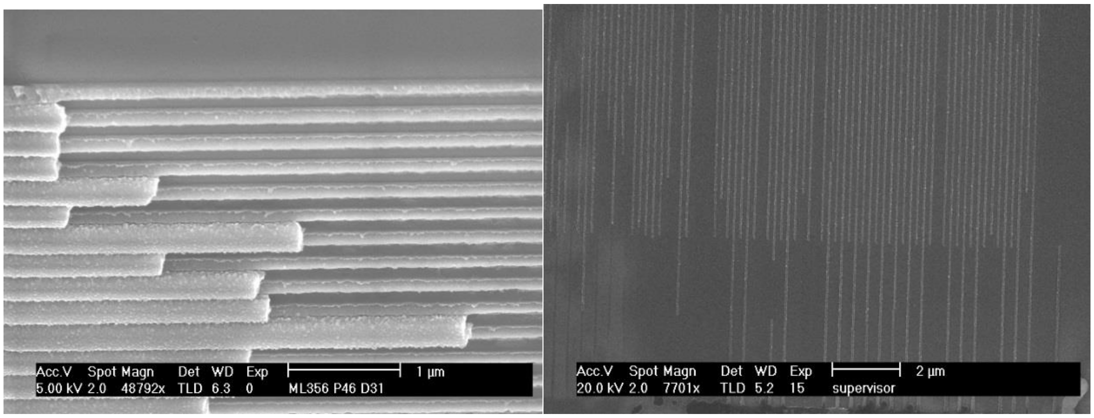

Figure 3.24 Examples of poor or partial lift-off of gold lines on silicon where some of the material is not removed (left) and a damage of grating (gold on silicon) from a vigorous lift of step where line of metal at the bottom of the image are removed entirely (right).

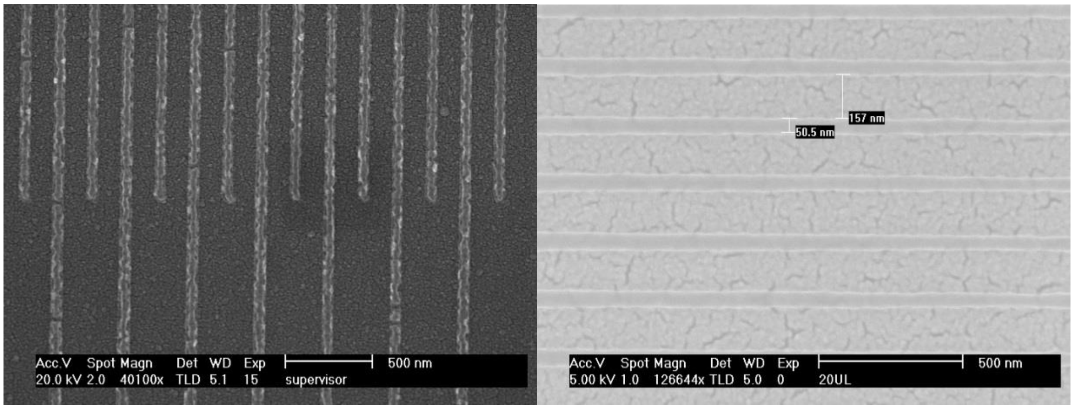

Figure 3.25 Micrograph of 50 nm raised electrodes (gold) on a gold surface, at 200nm pitch. Patterns were transferred from SML100 (left) and Micrograph of ~150 nm raised electrodes (gold) on a silicon surface, at 200nm pitch. Patterns were transferred from SML100 (right).

EBL tools are suited for fine areas of patterning in relativity small areas, as photolithography tools are limited in their resolution as discussed in chapter 1. However, patterning large areas with electrons takes a long time even with sensitive resists, and required a high precision stage with multiple write fields. Using PMMA or SML resist, patterning the wires and pads to the edge of the chips was taking > 24 hr per chip, and taking up time and the limited life span of the field emission electron source. To speed up this repetitive and time-consuming task, photolithography was used. This process allowed multiple chips to be patterned in minutes and greatly increased throughput, as well as provided large surfaces for proof of concept experiments.

Masks for photolithography were designed using the CAD program DRAFTSIGHT™ - (Dassault Systèmes). An array of designs shown in Figure 3.26 were transferred onto quartz glass as shown in Figure 3.27 by the company JD-photodata. The fused silca quartz glass is optically transparent in visible and near UV wavelengths (λ = 365nm), with chrome masking of features. As small chips were being fabricated, multiple designs could be fitted on a 5” single mask, and both wires and electrodes, and gratings were created in positive and negative tones, as well as designs useful for this and other projects. The maximum resolution of the mask features were 2.5 µm, which although not high enough resolution for the original designs and project scope, would allow quicker fabrication for trials and proof of concept experiments.

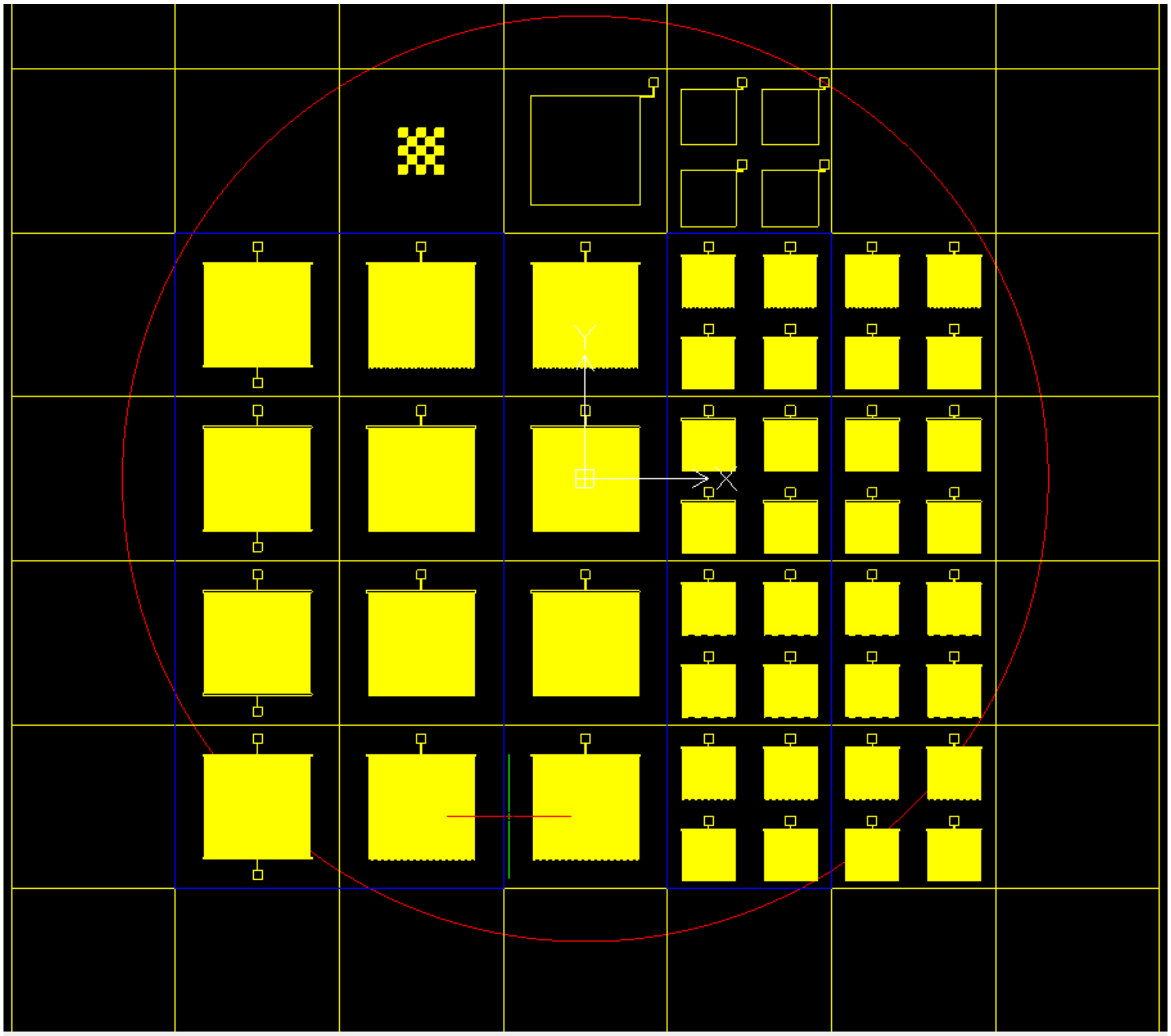

Figure 3.26 CAD design of photomask and final photomask.

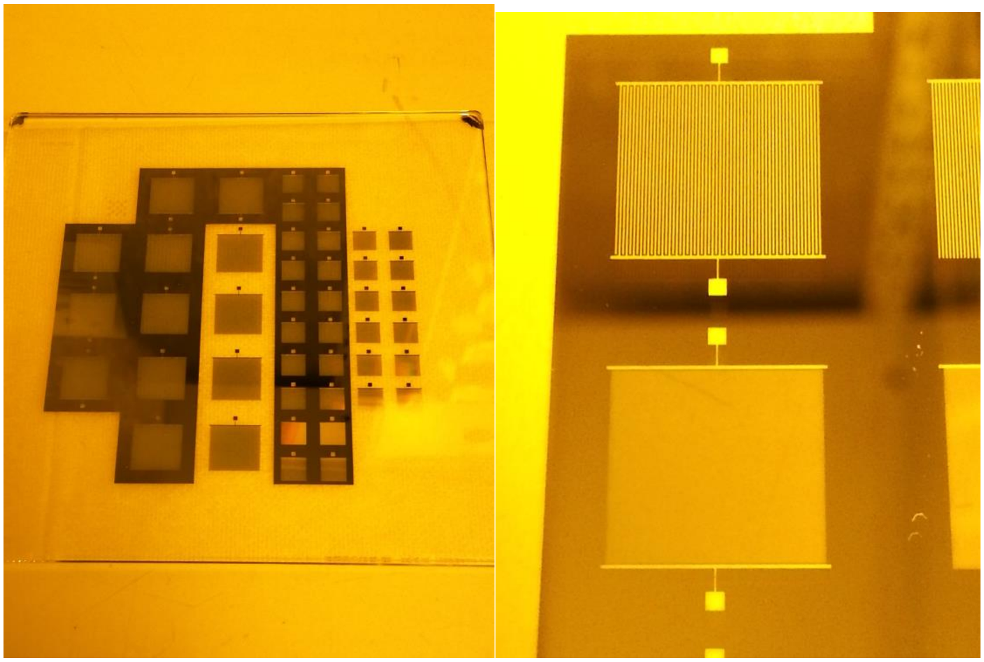

Figure 3.27 Image of one completed mask (left) and (right) zoomed in imaged of interdigitated fingers at 100 µm and 50 µm pitch.

3.7 Sandwich Electrodes

An alternative and novel design that aims to simplify the chip fabrication process by eliminating the metal deposition step is shown in Figure 3.28. This process makes use of spin on carbon (SOC), a spin able hard mask consisting of fullerene molecules, the thickness of which can be controlled in the spin speed stage, and oxygen etching to pattern the carbon using a photoresist. The hard mask, HM140 provided by Irresistible Materials (97) hardens after PAB to provide support for the final electrode. Initially for proof of concept and process development, designs of these electrodes are at a larger feature size, 5 µm – 25 µm, compared with the Ebeam lithography, and instead make use of photolithography. The similar process with exception of patterning can be used in further work, where Ebeam is used to minimize feature sizes in replacement of photolithography. The development of the spin on carbon material is discussed in chapter 4.

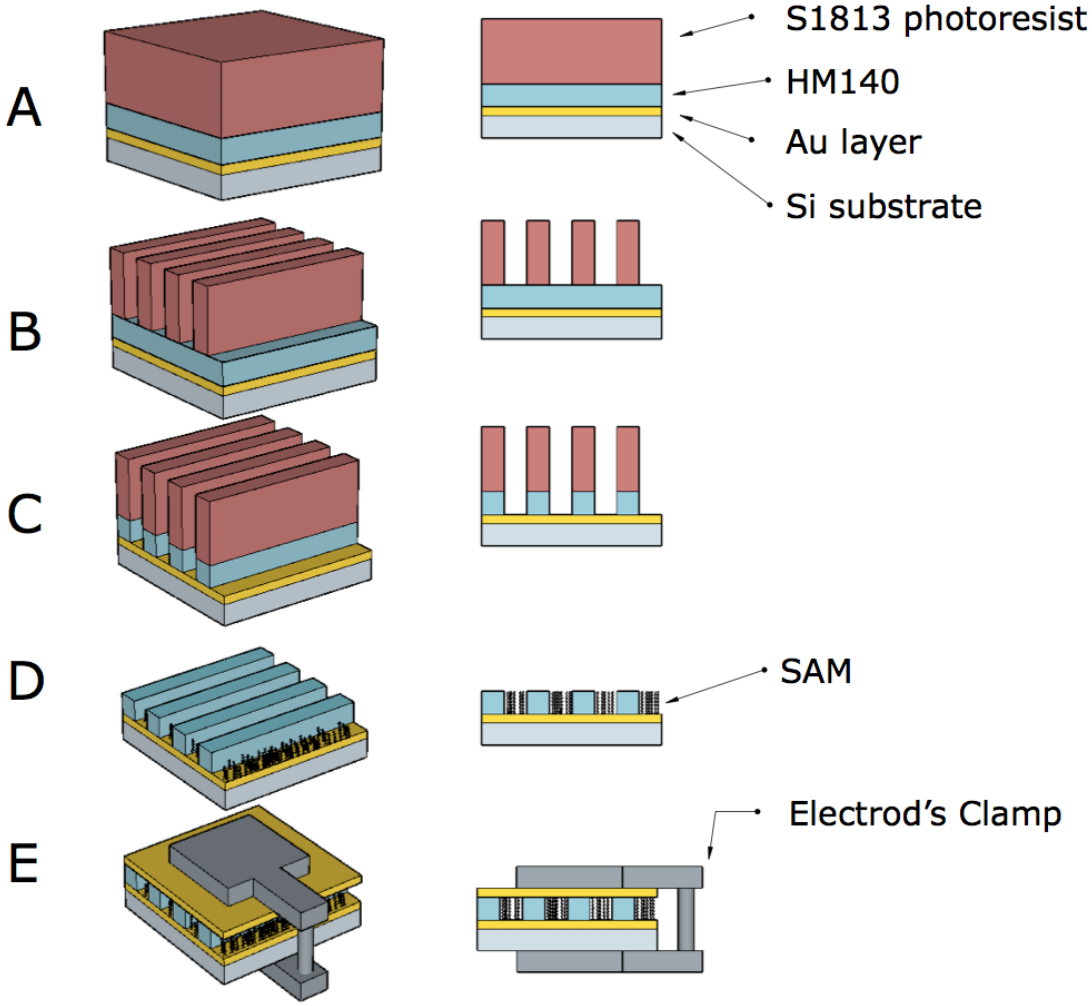

Figure 3.28 Sandwich electrode fabrication process A) spinning of resist on a carbon layer (B) photolithography (C) pattern transfer via etching (D) Resist removal and SAM deposition (E) clamping of electrode for electrochemical analysis

3.7.1 Substrate Preparation

Fabrication of sandwich electrodes was investigated along with the etch rate of the various hard masks(120). Patterning was initially performed using photolithography and the photomasks shown in Figure 3.26, which have a dense line resolution from 2.5 µm – 100 µm half pitch. For denser lines, EBL and SML resist could be used instead of the photoaligner and photomask.

Two types of SOC formulation were used in this work, HM140 series and HM340. Each of these formulations is made of a fullerene derivative and crosslinking group which can be mixed at different ratios to give different final carbon content, and different etch resistances. The HM140 is created from a formulation of a mix of C60 PCBM – [6,6]-Phenyl C61 butyric acid methyl ester and C70 PCBM – [6,6]-Phenyl C71 butyric acid methyl ester, shown in Figure 3.29, along with an epoxy crosslinker Poly[(o-cresyl glycidyl ether)-co-formaldehyde]. Table 3.4 shows the different formulation and ratios of each component.

	PCBM (g / l)	**oQDM (g/ l)**	**Epoxy Crosslinker (g / l)**	**Solvent**
HM140-350	12.5	-	12.5	Cyclohexanone
HM340-350	-	12.5	12.5	Anisole
HM340-383	-	20.83	4.17	Anisole

Table 3.4 Formulations of the different versions of SOC, with the ratio of each type of modified fullerene and crosslinker.

The crosslinker, upon heating to 350°C for 3 min, reacts with the fullerene derivatives to form an insoluble and harder carbon based film. The HM140 SOC has been previously characterised, but while the HM340, made from the fullerene derivative o-Quinodimethane C60 monoadduct, was experimental it promises better thermal stability, etch control and planarization, all which are of importance in the sandwich electrode. The experiments here lead onto the work of characterisation that is the focus of Chapter 4 in this thesis, and as such details of the use and composition of the hard masks are not discussed in detail in this chapter.

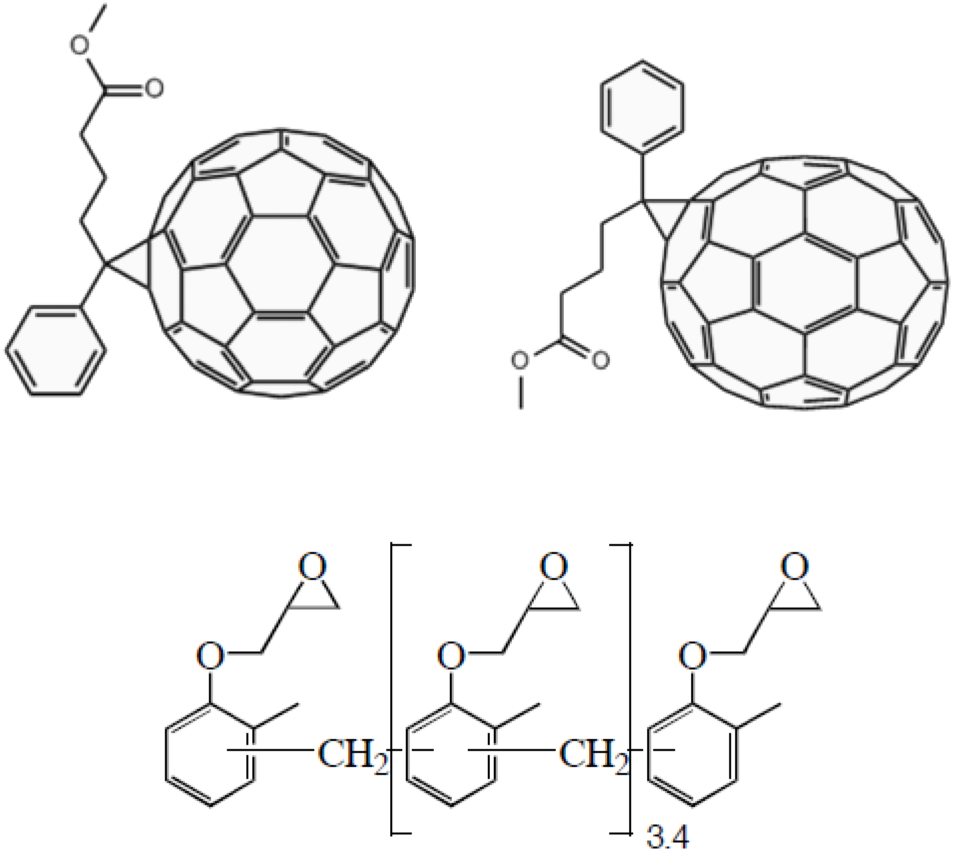

Figure 3.29 Chemical structures of a) C60 PCBM b) C70 PCBM and c) Epoxy crosslinker

The SOCs were mixed from their components and dissolved in organic solvent to a final concentration of 25 g/l. This were used to spin a film initially at 50 nm at 1500 RPM for HM140-350, as shown in the spin speed curve in Figure 3.30. The HM340 was also spun to the same thickness. Spin speed curves for this SOC were determined as discussed in chapter 4. Post exposure bakes (PAB) for each formulation were 300°C for 120 seconds and 300°C for 180 seconds for the HM140 and HM340 series respectively.

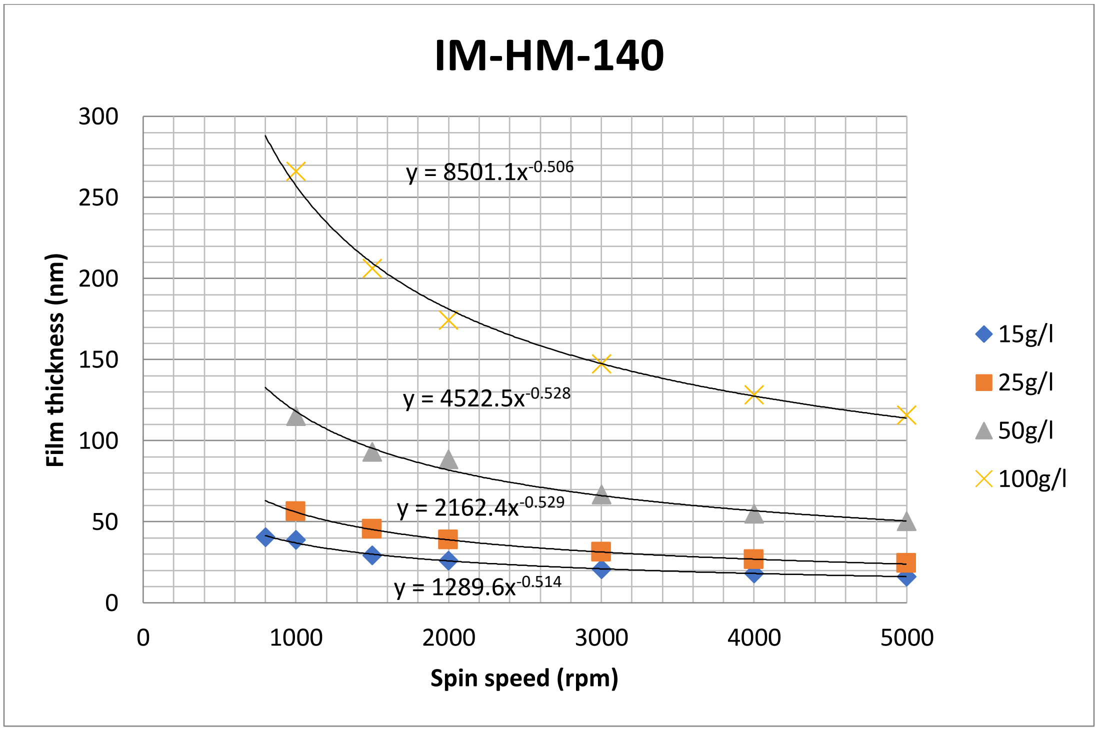

Figure 3.30 Spin speed curve of HM140 in cyclohexanone solvent (135)

The photoresist S1813 was purchased from Shipley, and spun at 5000 RPM to a measured thickness of 1.25 µm, measured by dektak, and a PAB of 115°C for 60 seconds. Patterning of the resist using the photomask was performed under UV with emission spectrum of 365 nm. Figure 3.31 shows a pattern in the photoresist

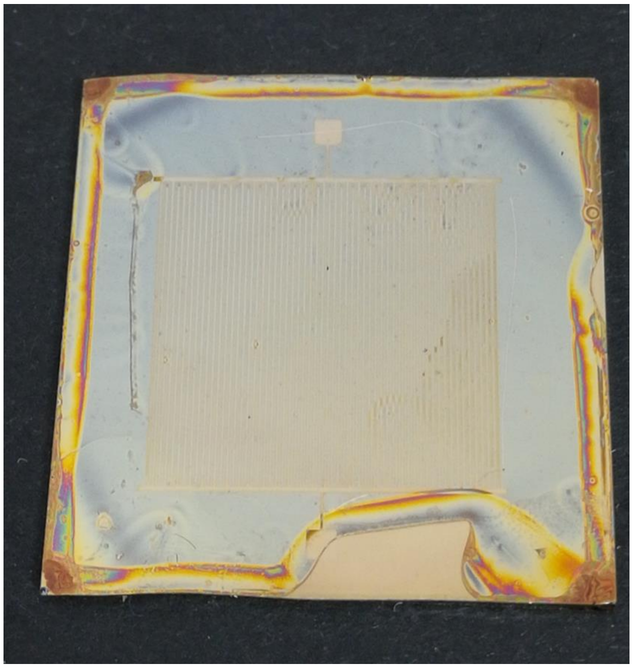

Figure 3.31 A gold coated, silicon chip with 100µm dense lines patterned in S1813 before pattern transfer to the SOC.

3.7.2 Etching

The HPT-100 O_2 Asher (Henniker Plasma) was used for oxygen etching. The HPT-100 can produce a maximum power of 300W and a flowrate of O_2 of 50 sccm. At the conditions used, the HM140 was determined to be removed at a rate of 2 nm/min, but the HM340 was not removed at all, suggesting it was a much more stable hardmask.

Initially there were many issues to achieve a pattern that was flat across the whole device, likely due to the anisotropic etching using the Asher. These were solved by careful mounting of single chips in the Asher chamber. Figure 3.32 shows SEM images of a completed pattern, the height of which are 35nm.

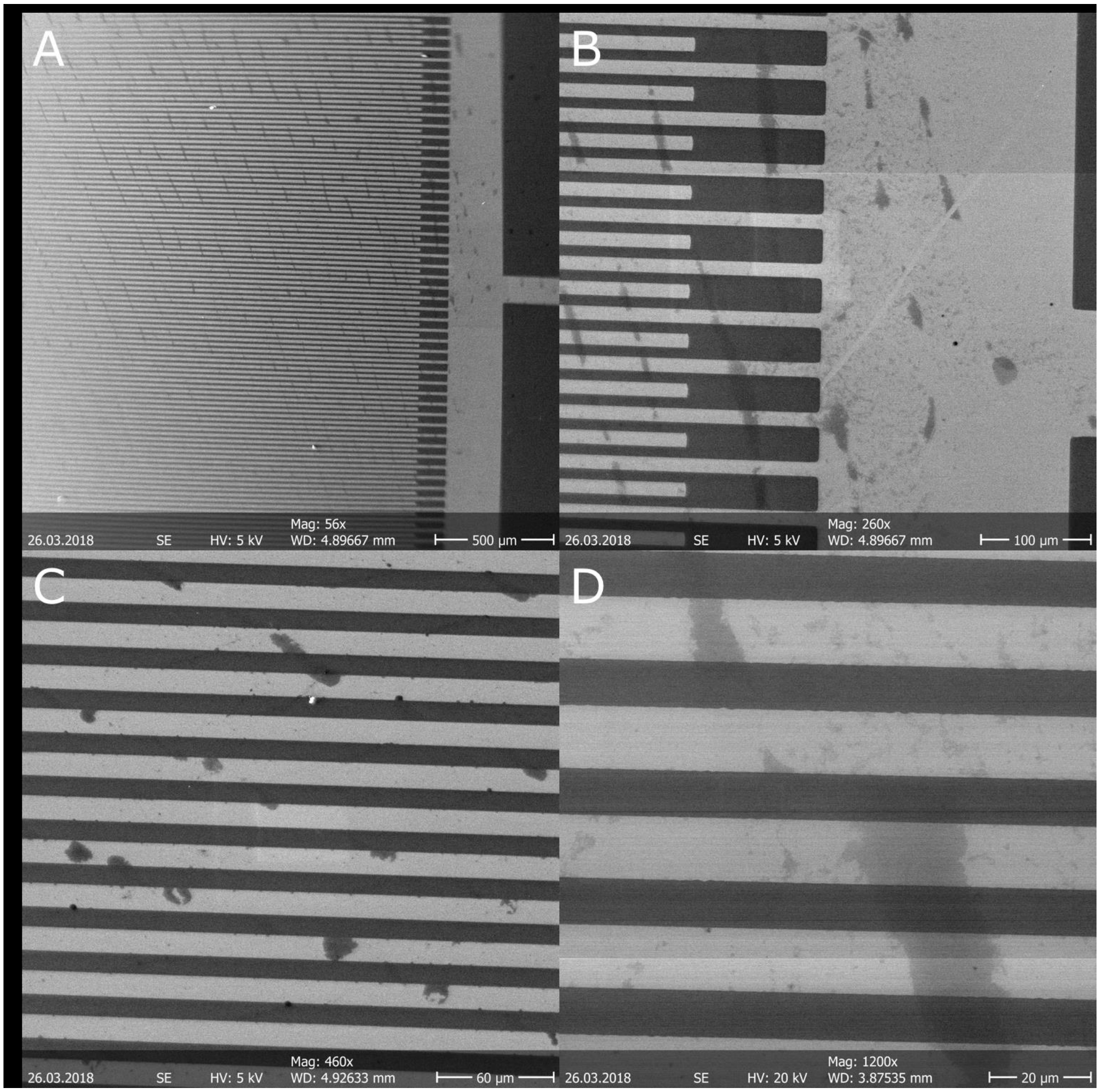

Figure 3.32 SEM images of the 10 µm features in HM140 after etching. (A) and (B) side of the interdigitated finger design and (C and D) close up of the dense lines.

3.8 Conclusions and Further Work

Multiple different fabrication approaches were used in this work with various successes and challenges along the way. The ebeam resist SML was successful patterned with sub 30 nm features, but transferring the pattern to metal was less successful, with good results only with features at >100 nm on a larger pitch. Fabrication using photomasks were achieved and these surfaces. The materials of construction needed to be changed multiple times in the project, from silicon oxide and aluminium to gold and hafnium. Throughout the work the quality of the gold deposition was often called into question, so further fabrication options using the SOC aimed to avoid this issue by using commercially purchased surfaces without the need to sputter or evaporate. The sandwich electrodes surfaces were fabricated successfully, and further work will ensure that the sandwich structure can be made. This will likely involve creating a surface that is completely flat across the whole area on the nanometer scale, and depositing the SAM layer, aptamer and target molecule whilst the two sides of the device are clamped together using a microfluidic set up.

The biosensor molecules them need to be proven to give a signal on two electrodes simultaneously which was not achieved, and more work on the deposition of the aptamer and SAMs, and characterisation of this is required.

CHAPTER IV

Carbon Hardmasks

4.1 Introduction

Carbon based hardmasks have a variety of uses as discussed in chapter 1. The primary use in fabrication and lithography is that of a transfer layer for dense, high aspect ratio etching. With the continuing advancements of ever smaller feature sizes in electronic devices, it is necessary to adopt increasingly thin photoresist films to alleviate the problems of pattern collapse due to high aspect ratio.

The use of a multi-layer etch stack incorporating a sacrificial layer of carbon is one method to allow the pattern in the resist to be transferred via etch into the substrate. Traditionally deposited by chemical vapour deposition, a thick amorphous carbon layer is coated onto the substrate followed by a thin silicon layer (spun or CVD), and finally the resist film. The thickness of the resist is sufficient to etch the pattern into the silicon whilst avoiding pattern collapse issues associated with high aspect ratios, and then the process makes use of the alternating organic and inorganic layers of material allow for good etch selectivity with SF_6 and O_2, to transfer the pattern into carbon with silicon acting as a hardmask. Finally, the pattern can be etched into the substrate layer with the carbon hardmask allowing sufficient etch protection. Deposition of the carbon layer with CVD faces the challenges of high capital and running costs, particle defects, and the non-planarizing nature of the layer(136), and therefore there is a drive for alternatives. Spin on carbon, that is a carbon-based formulation in a volatile solvent that can form a defect free thin film upon spinning, avoids these challenges by both simplifying the process and being suitable to run with existing setups required both up and downstream in the fabrication process.

Some of the major challenges that a SOC formulation must overcome are caused by the fact that the spun carbon-based films will have a lower carbon content than the pure amorphous layer from CVD. The presence of other atoms, particularly hydrogen and oxygen, that are required to give solubility, can cause ‘wiggling’ of features during the pattern transfer (137,138). Wiggling is a deformation of the features caused by the SF_6 etching step thought to be caused by volume changes and concomitant stresses in the features due to the substitution of hydrogen atoms with fluorine atoms. A study by Van Delph(139) on a spin-on-carbon based on novalac achieved 40 nm half-pitch resolution, with isolated 40 nm lines at a 20:1 aspect ratio. Wiggling becomes an issue when etching at this size, as shown in Figure 4.1 and Figure 4.2. The wiggling effect is typically more severe for aliphatic compounds (140) and therefore by using a SOC without these groups (i.e. aromatics instead), accurate and reliable pattern transfer should be possible.

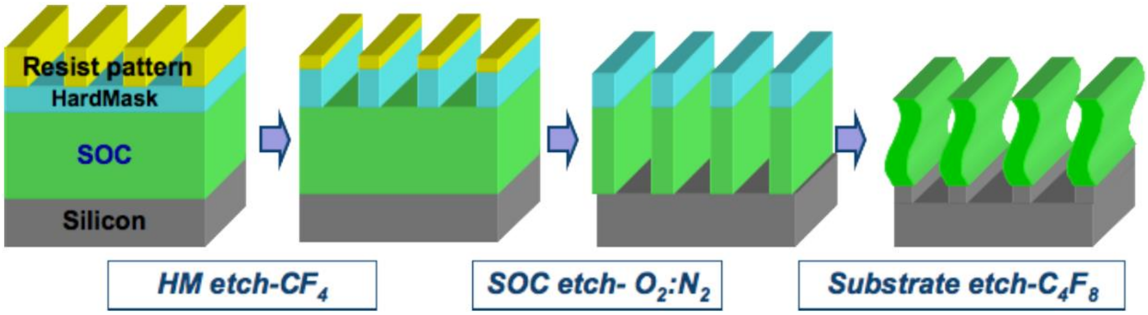

Figure 4.1 Schematic of the wiggle effect in a multistack

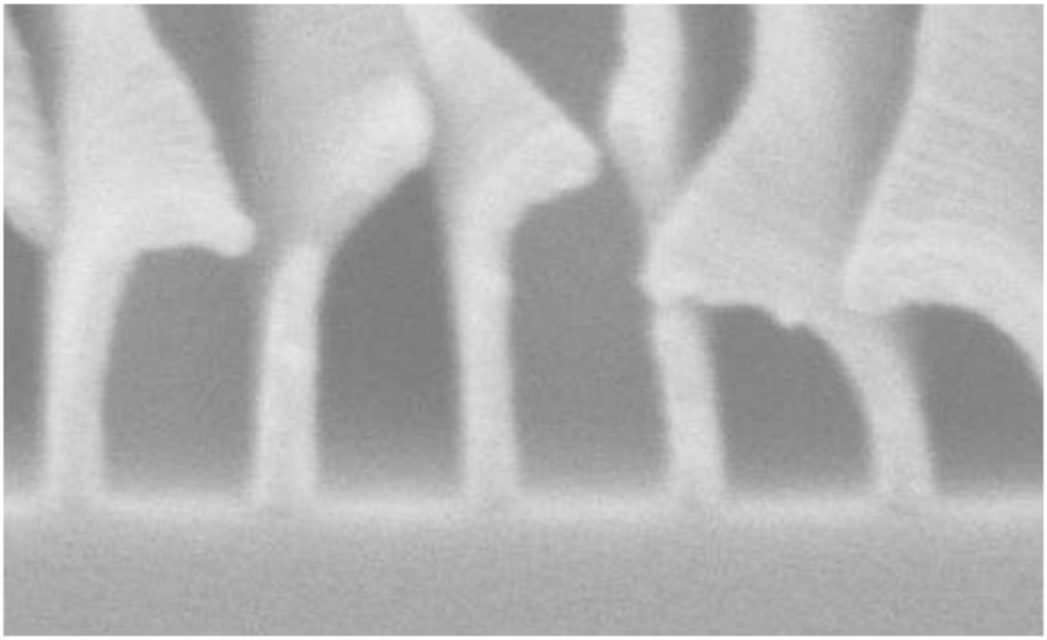

Figure 4.2 SEM image of a spin on carbon that has deformed due to wiggling. (137)

A group of molecules that are both high in carbon —thus providing high etch resistance— and which have no aliphatic groups within them are the fullerenes. Fullerenes are carbon allotropes, hollow geometric shapes such as spheres or cylinders consisting of an arrangement of hexagonal ring like structure of carbon atoms as shown in Figure 4.3. The first fullerene was that was manufactured was the buckminsterfullerene, created by Smalley et al in 1985 (141),and since his discovery fullerenes have been the focus of many areas of science due to their unique properties. Work on a fullerene based SOC has been ongoing within the University of Birmingham for some time, and this chapter focuses on continuation of that work and improvement of the hardmask.

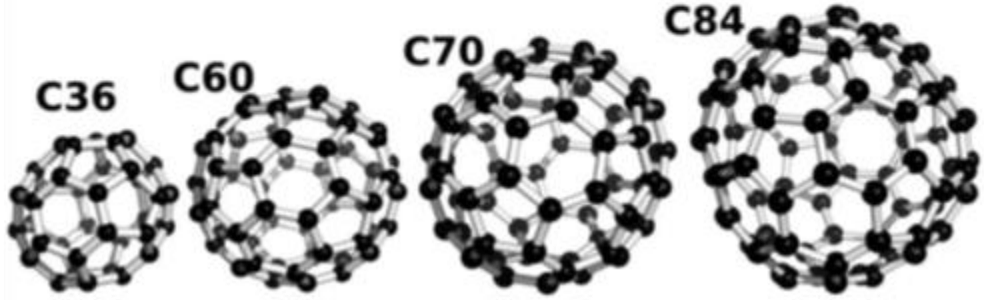

Figure 4.3 Spherical fullerenes of different sizes, showing the total carbon atoms (142)

4.1.1 Previous Work

The commercially available HM 140 series of hard masks are fullerene based SOC and as such have a low Ohnishi number, a high etch resistance and do not exhibit wiggling during SF_6 etching. This formulation was previously developed jointly at the University of Birmingham, Irresistible Materials and Nano-C (143), and shows promise as a suitable SOC for sub 22 nm multi stack feature transfer. Figure 4.4 shows the monomer groups of the HM140 series, formulated by the addition of an ester terminated fullerene group and novalac epoxy, a phenol-formaldehyde resin. The formulation is fully soluble in certain organic solvents. When spun and baked, cross linking of the components creates a film insoluble in the casting solvent, leaving a thin film on the substrate. Etching data of HM140 resists show it to be comparable with that of CVD carbon and of commercially available alternative SOC(143), with high thermal stability low etch rate in halogen plasmas and high etch rates in oxygen plasmas. Importantly, this hardmask did not exhibit wiggling upon pattern transfer.

The HM140 based SOC has been proven to be a potential candidate for multilayer etching, at high resolutions. But still it has certain characteristics that need further improving — particularly the thermal stability and halogen etch resistances, which did not match the targets set by the client. Development of the next generation of fullerene hardmasks, the HM300 series resists is ongoing, and aims to build upon the properties of HM140. The rest of this chapter details the work undertaken to achieve on these and other targets by the addition, replacement or removal of various components in the HM300 series formulation, and initial work on further formulations HM900 and HM1000

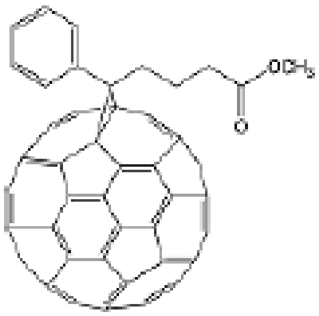

Phenyl C_{60} Butyric Acid Methyl Ester

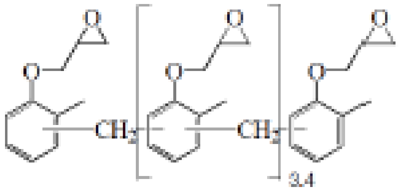

Poly[(o-cresyl glycidyl ether)-co-formaldehyde

Figure 4.4 Molecules used in the HM140 series of hardmask

4.2 Methods

All the fullerenes were synthesised at Nano-C and shipped as solid powders to the University of Birmingham for use. Unless mentioned, all formulations of the completed solutions (fullerene with cross linker in solvents) were made in the clean room environment on site, and stored in refrigerated conditions. The novalak crosslinker was purchased from Sigma Aldrich (UK) and Huntsman Advanced Materials (USA), stored at 21 °C. Solvents were purchased from Sigma Aldrich (UK), and unless stated, HPLC grade. Water was purified in using a Purite water purifier (18MΩ.cm). Compounds were dissolved and mixed in the solvent (anisole) with ultrasonic agitation, and filtered using a 200 nm pore filter before use. Formulations not used immediately were stored in refrigerated conditions. Any pre-formulated samples from Nano-C were stored likewise.

The following parameters were for a standard hard mask, and other formulations differ where stated. The standard spin recipe used required 70 µl for 18 × 18mm for chips. (350 µl for 4” wafers) spun at 500 RPM for 5 seconds, ramped up (ramp time 1 second) to the final spin speed stated for 60 seconds. For the higher spins (>4000 RPM) an additional short spin at 4000 RPM for held for 3 seconds before ramping (1 second) to the final speed. Standard post application bake (PAB) was 300°C or 350°C for 3 minutes immediately after the spin cycle on a preheated wafer hotplate.

Elution tests were carried out to ensure an insoluble film had been created after the PAB. In each case the thickness of the sample would be measured by ellipsometry or with the surface profiler both before and after a 60 sec dip in the casting solvent. If there was no change in the thickness then the film was accepted as insoluble and fully crosslinked. Where a change in film thickness or quality was observed, the formulation would be considered only partially cross linked, and the PAB time or temperature would be altered.

4.3 HM340 Series Initial Characterisation

HM340 series hard masks are formed from a fullerene based compound and a novalac epoxy crosslinker, similar to HM140 but with the noticeable difference being the fullerenes. The HM340 uses a mixed-multiadduct (MiMu) set of fullerenes consisting of fullerene derivative– o-Quinodimethane C_{60} (OQDM), shown in Figure 4.5. The mixed OQDM consisting of a blend of C_{60} – C_{84} OQDM fullerenes, alongside the crosslinker Poly[(o-cresyl glycidyl ether)-co-formaldehyde] (CL-1201).

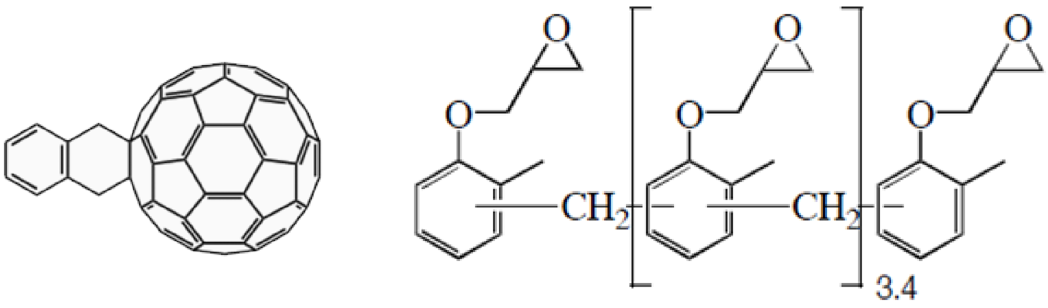

Figure 4.5 An example of the fullerene present in MiMu (left), and the novalac epoxy Poly[(o-cresyl glycidyl ether)-co-formaldehyde (right).

The fullerenes react with CL-1201 at elevated temperatures to polymerise into an insoluble film. The fullerene compound is made of a mixture of different molecular weight fullerenes that are simultaneously created during synthesis, known as mixed fullerene multi adduct. The formulations were initially made at three different ratios of the fullerene to crosslinker, to observe the difference performance with relation to amount of fullerene, and thus carbon content in the films. These compounds were named HM340-383, HM340-350 and HM340 -317 for the 5:1, 1:1 and 1:5 parts fullerene to cross linker respectively. The atomic compositions of the components are shown in Table 4.1, and the total carbon content and Ohnishi numbers of each formulation, after solvent evaporation shown in Table 4.2.

	C	**H**	**O**
Fullerene	98.3	1.74	
Poly[(o-cresyl glycidyl ether)-co-formaldehyde]	78.4	18.7	6.8

Table 4.1 values of Carbon, Hydrogen and Oxygen (% weight) in different components

Formulation	**Parts fullerene**	**Parts Cross linker**	**Carbon content (% weight)**	**Ohnishi Number**
PMMA	N/A	N/A	76.3	5
HM140-383-100	5	1	88.6	1.65
HM140-350-100	1	1	83.8	2.0
HM340-383-100	5	1	94.5	1.8
HM340-350-100	1	1	87.1	1.39
HM340-317-100	1	5	79.7	2.35

Table 4.2 showing the carbon content by weight, and Ohnishi Numbers for various spin on carbon formulations, as well as PMMA.

All initial characterisations were performed using up to 100 g/l concentrations, with the fullerene to crosslinker ratios in Table 4.2 and in anisole solvent. Further work focused on changes to these parameters as well as additional formulations to improve characteristics of the SOC.

4.3.1 Spin Speed Curves

Use of a spin on carbon requires spin speed curves to determine film thickness at a given concentration. The standard formulations of HM340 series resist were prepared and spun onto chips of silicon at various maximum spin speeds at solid concentrations ≤ 100 g/l to calculate spin speed curves. All formulations were cast in anisole solvent, using the standard spin recipe and procedure. The thickness of the film was measured using both ellipsometry and the surface profiler after a PAB of 300°C for 3 minutes.

Figure 4.6 shows the spin speed curves at different concentrations for the 383 formulation, and Figure 4.7 shows the thicknesses of film spun at 1000 RPM for 383 and 350 formulations, at a given concentration. There are no significant differences in thickness between the two formulations. Films from 20 nm to 240 nm were measured. The film quality was good with no major deviations or changes in thickness at different points across the chips.

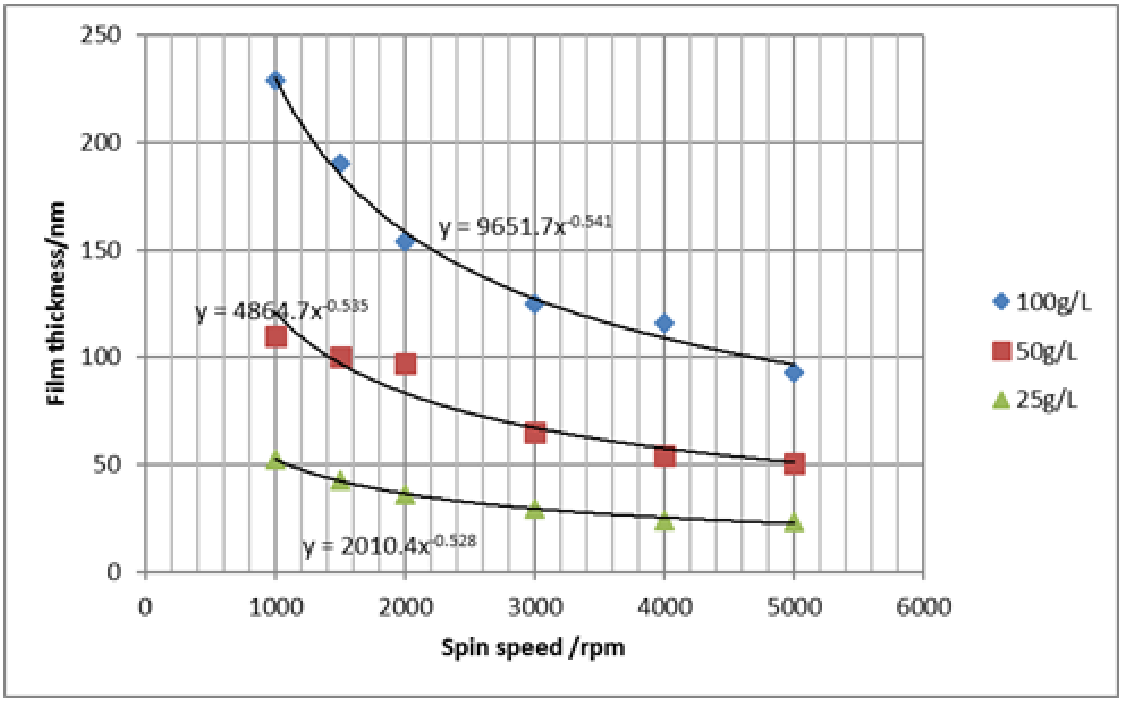

Figure 4.6 Spin speed curves of HM 340-383

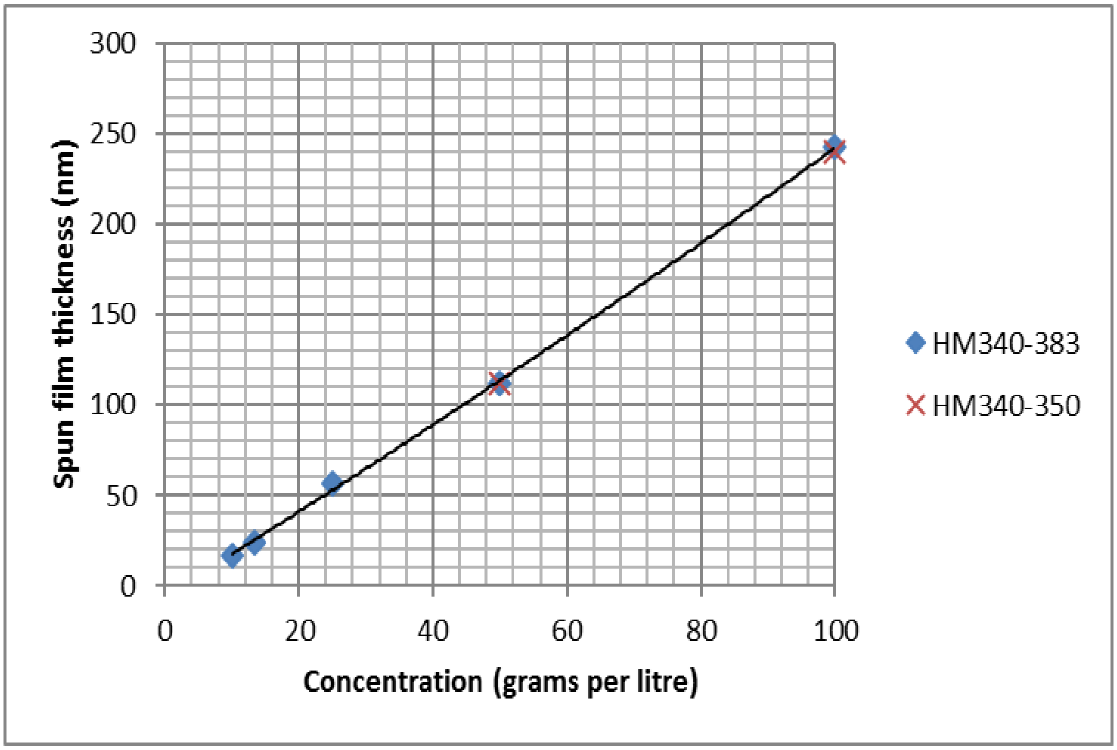

Figure 4.7 Film thickness in relation to solid concentrations of HM340-383 and HM340-350

4.3.2 Thicker Films

Some applications require thicker films than can be spun using the standard formulation. There are multiple parameters that effect film thickness. These are summarised in Table 4.3. The dominant parameters that are controllable by the end user are spin recipe (speed and time of the spins), with the ambient temperature and humidity only having a minor effect (144) as well as not being a realistic variable in a cleanroom. The simplest method to produce thicker films with a given formulation is by lowering the spin speed. The thickness for a film is generally inversely proportional to the root of the spin speed(145) as shown in equation 4.1 where t is film thickness and ω is angular velocity:

$$t \propto \frac{1}{\sqrt{\omega}} \tag{4.1}$$

When reducing spin speed there is a lower limit at which the film quality and uniformity are affected. The exact limit depends of the formulation and equipment; however, film quality is usually an issue at < 800 RPM. Substituting the measured thickness of 240 nm at 100 g/l at 1000RPM into equation 4.1, a maximum thickness of only ~270 nm would be achievable at 100 g/l.

It was determined experimentally that applying a second film on top of the first, after PAB, would achieve linearly thicker without detriment to the film quality, however, as this would add time and cost to the fabrication process, this too is not a suitable solution to the underlying problem. With no simple solution for the end user to achieve 500 nm films, instead changing the formulation itself was investigated. The creation of higher concentration formulations, the use of different casting solvents and the addition of a thickening component were proposed to be investigated to achieve this aim.

Parameter	Effect on Thickness	Comment
Formulation		
Composition	Varies	
Concentration	Increases	
Solvent volatility	Increase	
Solvent viscosity	Increase	
Spin Cycle		
Spin speed	Decrease	Minimum spin speed required to achieve good coating.
Spin time	Decrease	Increases in time will not affect thickness once the solvent stop evaporating
Solvent in atmosphere	Decrease	Affects solvent evaporation rate
Ambient conditions		
Temperature	Negligible	Increase solvent evaporation rate, decreases viscosity, which have opposing effects on thickness
Humidity	Decrease	Affects solvent evaporation rate
Other		
Multiple coatings	Increases	

Table 4.3 Showing how increasing parameters affect the thickness of a spun film.

Solid concentrations of 125 g/l and 150 g/l of HM-340-383 were mixed in anisole solvent. Higher concentrations, particularly higher masses of fullerenes, add significantly to the cost of the formulations, so although simple, this solution would have an impact on the cost of hardmask. There is also an upper limit of solubility, and formulations of 150 g/l became difficult to filter, and even after an extended 24-hour mixing process, a significant amount of solid was lost in the filtering step. This suggests the solubility limit had been approached, and as the formulations were mixed at 21 °C and stored at 5 °C, the films required further filtering before use, or if unfiltered gave poor films which could not be used. Concentrations of 125 g/l did not experience the same filtering difficulties.

Table 4.4 shows the maximum thickness of HM340-383 at a given concentration and spin speed of 1000 RPM. Increases in the concentration will not achieve the desired 500 nm thickness.

Concentration of solids (g/l)	**Spin speed (RPM)**	**Thickness (nm)**	**Comment**
100	1000	228	
125	1000	305	
150	1000	330	Poor Film

Table 4.4 Maximum thicknesses achieved at different solid concentrations.

The solvent in a formulation has a major effect on the film that is created, in terms of quality, thickness and uniformity. The lower the boiling point of a casting solvent (and thus higher the rate of evaporation), the thicker the resulting film, but high evaporation rates can lead to very non-uniform films as the resins may not have time to arrange evenly. On the other hand, if there is a lower rate of evaporation, centrifugal forces move the solution and resin solutes off the edge of the substrate leading to a thin film. Often the best results can occur with a mixture of multiple solvents acting together, with the low BP allowing a thick and uniform film to be created, and the high BP solvent helping to improve the quality of the film as shown in Figure 4.8. The challenge of modelling film thickness based on solvent is a complex one, and although models have been suggested for various situations there is not an overriding model that can accurately predict most practical situations, and therefore it is often more practical to determine the film thickness experimentally.

In this study, only solvents that were readily used or possibly acceptable in the industrial fabrication process were used. Formulations were mixed with different solvents and films spun cast in each solvent. The solvents used were cyclohexanone, toluene, xylene and cyclopentanone. A hardmask composition of HM340-350 at 100 g/l was used in each solvent. Combinations of the most suitable blends of solvents were also examined. Films were initially spun 1500 RPM, as this speed tended to give the highest quality films on the equipment. Table 4.5 and Table 4.6 shows the results of this experiment.

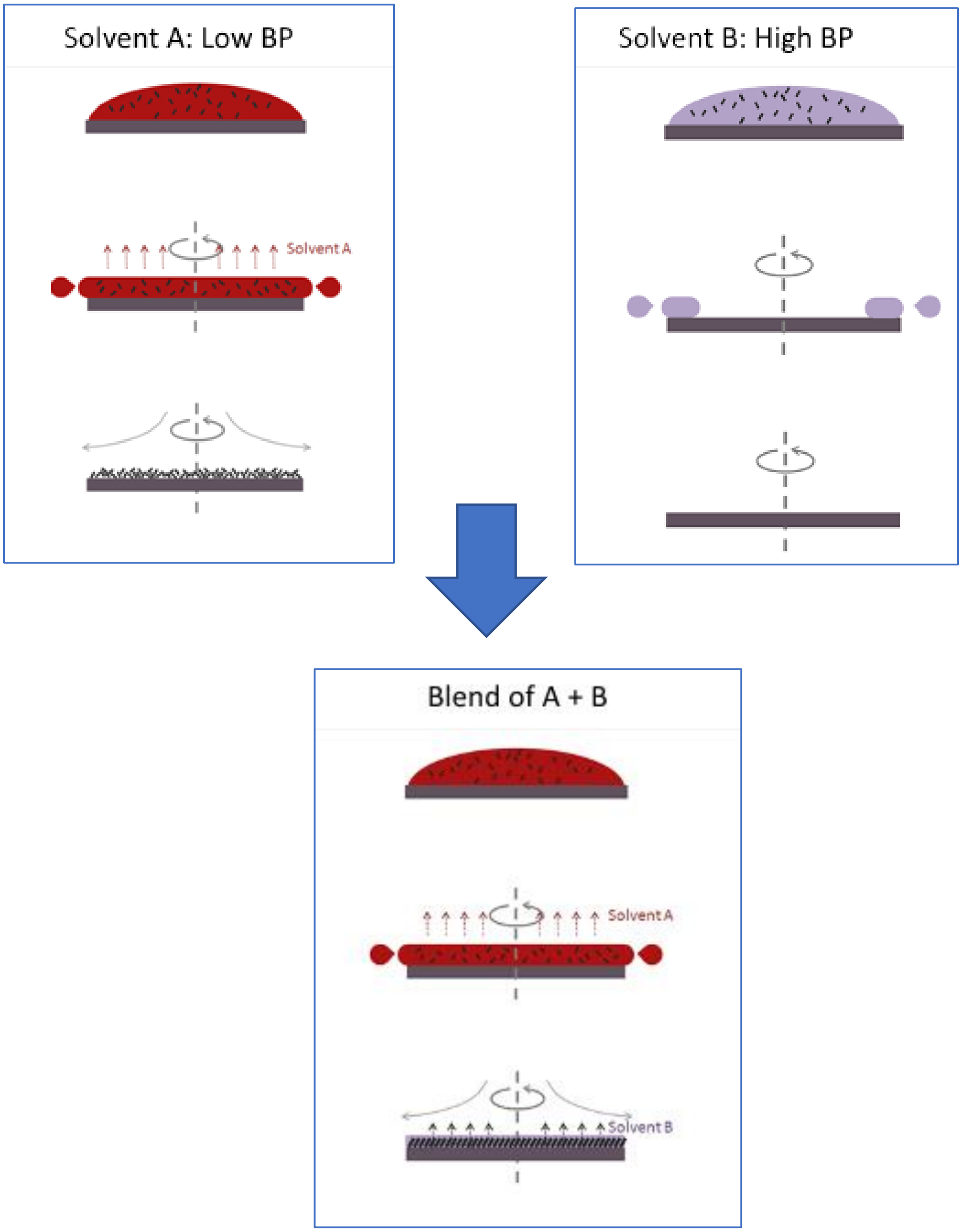

Figure 4.8 Diagram showing resin arrangement with A) Spinning of a low boiling point solvent B) with a high boiling point solvent and C) blended solvents

Solvent	**Thickness (nm)**	**Film Quality**
Anisole	220	Good
Cyclohexanone	283	Passable
Toluene	912	Poor
Cyclopentanone	-	Poor

Table 4.5 Summary of pure solvents and the thickness of films produced

Cyclohexanone (% v/v)	**Anisole (%v/v)**	**Thickness (nm)**	**Quality**
90	10	270	Passable
80	20	237	Passable
60	40	228	Passable
Cyclohexanone (% v/v)	Toluene (%v/v)	Thickness (nm)	Quality
90	10	318	Passable
100	0	283	Poor
Cyclopentanone (% v/v)	Toluene (%v/v)	Thickness (nm)	Quality
90	10	372	Poor

Table 4.6 Blends of solvents used to produce thicker films

After PAB, many of the formulations were not able to produce a useable film, the exception being the anisole / cyclohexanone blends and the cyclohexanone / toluene blend. The thickness increase in these films was significant compared to that of the pure anisole, and warranted further investigation. However, assuming different blends of solvents would result in a film thickness between the two extremes of pure solvents, the target of 500nm would not be reached, except in the case of toluene blended films. These experimental results were reported, but further work stopped as the use of toluene solvent inside the fabrication plant was not desirable in this case. The cyclohexanone /anisole blends would be used in further work. Both the poor and acceptable films spun films are shown in Figure 4.9.

Further work to increase the film thickness was undertaken with the use of additives to the formulation, effectively increasing both the solids concentration and the viscosity, but at a much lower cost than adding more fullerene. A molecule with a high proportion of carbon was needed to keep the total carbon content high and thus good etch resistances. Polystyrene and several co polymers of polystyrene were purchased from Sigma Aldrich and the effect on the formulation of HM340-350 tested. Figure 4.10 shows the molecules of polystyrene and poly (4-vinyl pyridine- co styrene) (PVPCS). PVPCS was purchased at three different ratios of pyridine to styrene monomer, 1:9, 1:1 and 9:1.

Formulations of polystyrene, polystyrene with CL-1201 and of HM340-350 with added PVPCS were created, spun and baked as per the standard procedure. Of these the polystyrene and polystyrene with CL1201 formulations did not produce a thermally stable film, which was totally removed during PAB at 300 °C.

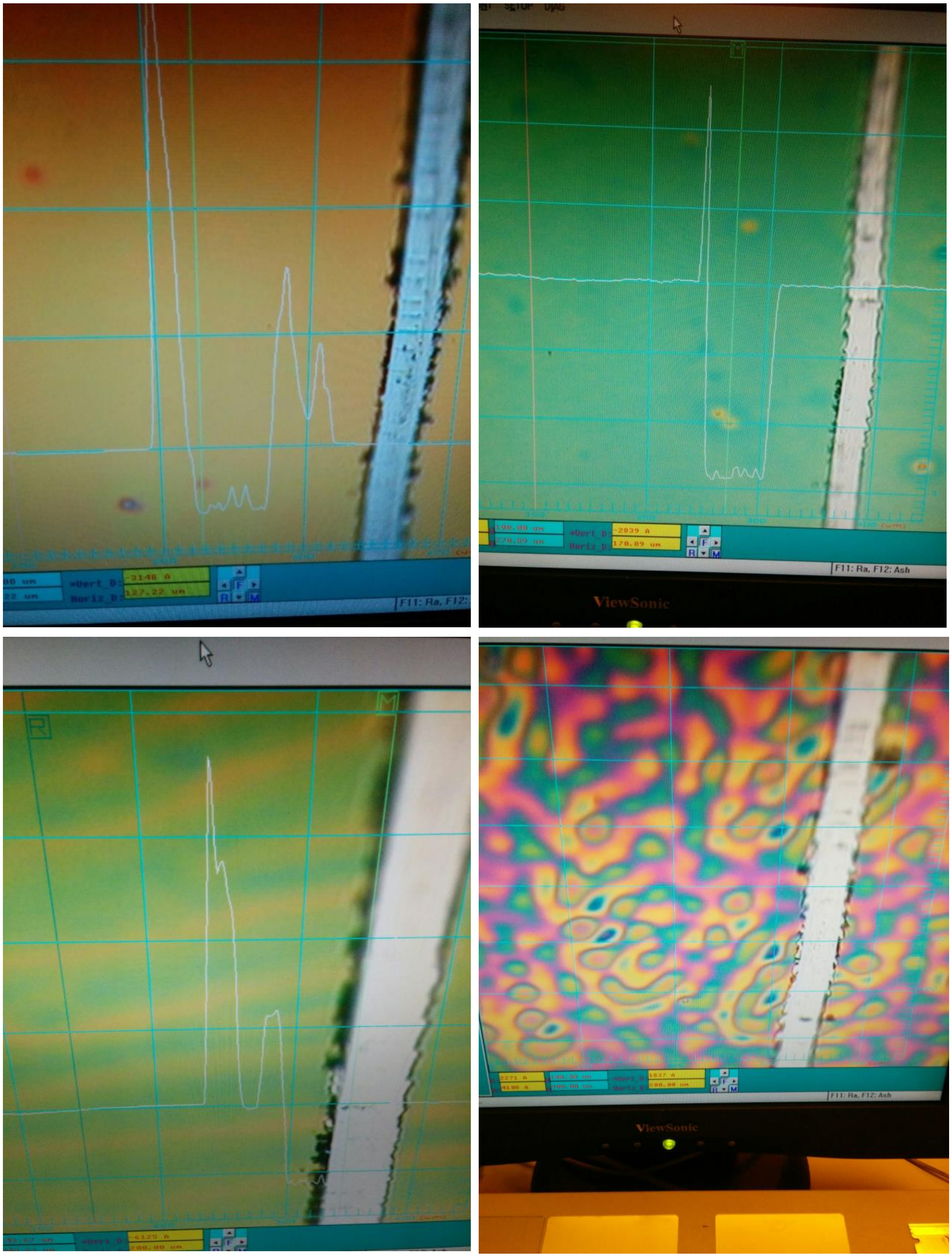

Figure 4.9 Images of films from the surface profiler of HM340-350 spun in (A) pure toluene showing regions of different thicknesses as a wave pattern (B)100% cyclohexanone, some imperfections (C) 90% Cyclopentanone 10% toluene (very poor), and (D) 90% Cyclohexanone, 10% anisole (passable)

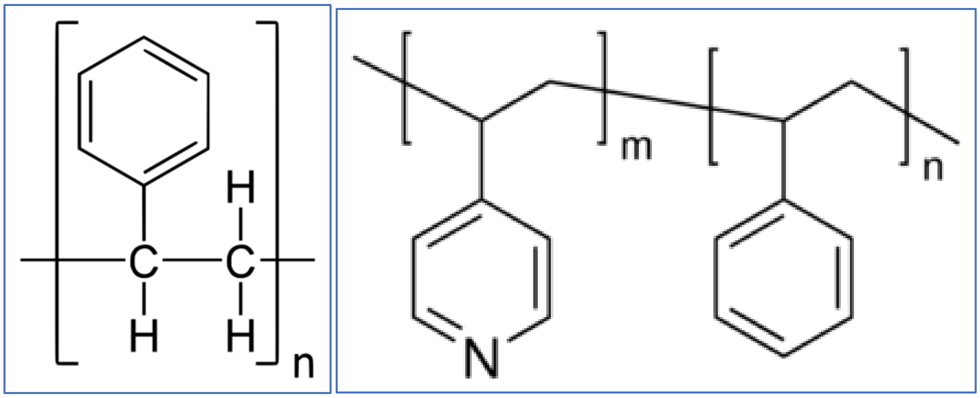

Figure 4.10 (A) Polystyrene (B) poly (4-vinyl pyridine-costyrene)

Formulations of polystyrene, polystyrene with CL-1201 and of HM340-350 with added PVPCS were created, spun and baked as per the standard procedure. Of these the polystyrene and polystyrene with CL1201 formulations did not produce a thermally stable film, which was totally removed during PAB at 300 °C. Experimentally it was found that only the PVPCS with 1 part vinyl pyridine to 9 parts styrene performed well in terms of solubility and film quality after PAB, and further formulations were made at varying concentrations. This deviation also contained the highest proportion of carbon of the co-polymers. The formulations total solid concentration could be increased by adding different masses of PVPCS, whilst keeping the fullerene and CL-1201 ratio at 1:1, giving control over the total carbon content. Figure 4.11 shows the spin speed curves of two different formulations, which spun films in the 500 nm region.

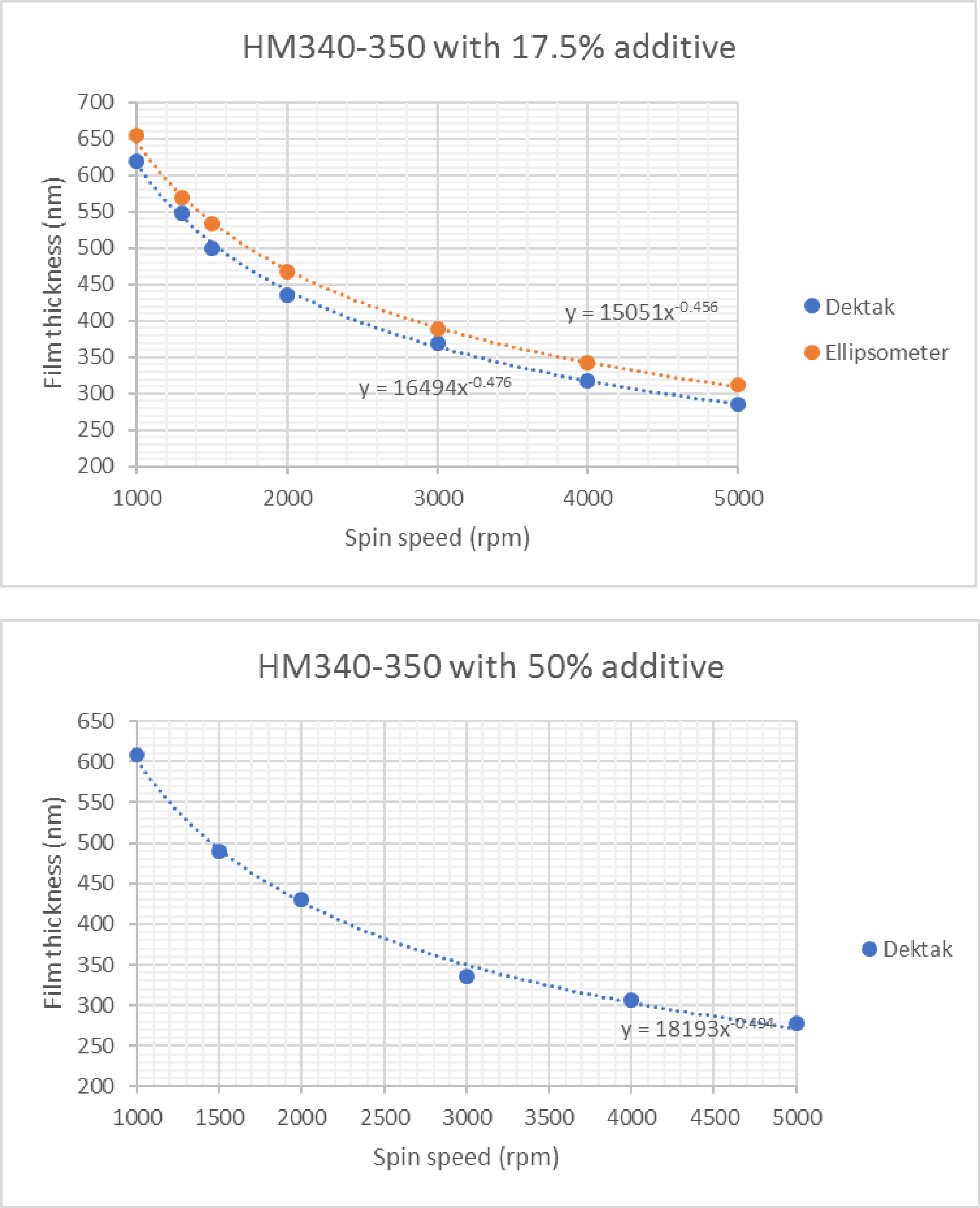

Figure 4.11 Spun thickness v concentration for (top) HM340-350 with 17.5% viscosity additive, total solids concentration 136g/L and (bottom) HM340-350 with 50% additive, total solids concentration 120g/L.

4.3.3 Thermal Stability

The thermal stability of the SOC is an essential parameter of the films. Due to downstream processes in a fabrication plant, the SOC film must be stable to temperatures of 400 °C. The method used to determine the thermal stability was thermogravimetric analysis (TGA). The principle of TGA is that the change of weight as a function of time, temperature and atmosphere can be used to determine both the composition of materials and to predict their stability, due to weight loss from desorption of volatiles, reduction and decomposition. A TGA tool in its basic form consist of a furnace, a sample holder with controlled atmosphere, a balance and a controller, and measurements are recorded over periods of time with a linear temperature increase, producing a TGA characteristic for a given substance and set of conditions.

The TGA was performed in collaboration with Nano-C in an argon atmosphere, with a temperature ramp of 10 °C/min. Samples for thermogravimetric analysis (TGA) were prepared by spin coating and baking several wafers, and the scrapping the films off, shipping the samples for TGA. Figure 4.12 shows that the thermal stability of the HM340-383, where 5.2% of mass is lost at 400°C, is an improvement on the permanence of HM140 (146) where mass loss of 13.7% was observed at 400 °C. This result shows that the structure of the HM340-383 film is significantly more stable, and approaches the 5% maximum mass loss at 400 °C industry target. The results from the two TGA are shown in Table 4.7.

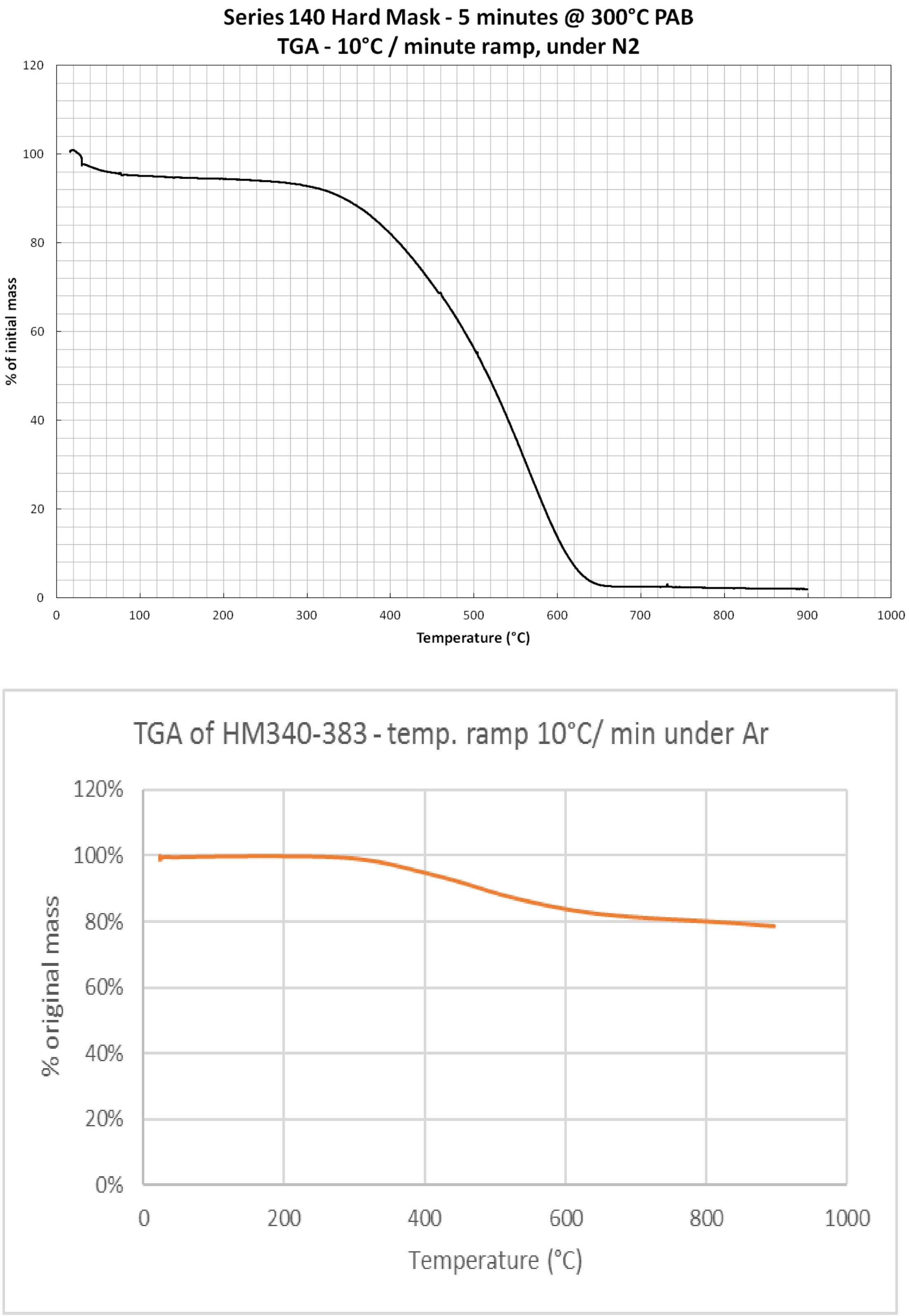

Figure 4.12 TGA curves, provided by Nano-C, showing (a) HM140 and (b) HM340-383 results.

Temperature (°C)	HM140 TGA mass loss (%)	HM340-383 TGA mass loss (%)
350	6.6	2.6
375	8.7	3.8
400	13.7	5.2
800	100	20.0

Table 4.7 The mass loss from TGA of HM140(146) and HM340-383

4.3.4 Thermal Acid Generators

There is commercial pressure for hardmask and resist to have the PAB temperature and bake time to be as low as possible, to increase throughput and decrease cost in manufacture. Initially, work on the HM340 series of resist was building on the HM140 series, and the PAB temperature and time procedure was inherited from this, however, to fully determine the optimal PAB parameters, the minimum PAB temperature was measured for the HM340 series of resist. Optimum PAB parameters were determined by measuring the thickness of a film after PAB at a specific temperature and time, and then thickness measurements were repeated after an elution test, to determine if the film was full formed and insoluble. The results of minimum require bake time and temperatures for each formulation are summarised below in first column of Table 4.8. The data shows that temperatures of 300 °C are required to achieve a fully insoluble film in the formulations with a minimum bake time of 180 seconds for HM340-383 formulation, and that this time is reduced as the fullerene content in the formulation is lowered.

Formulation	PAB conditions	1% addition CXC 1612 Minimum duration at 300°C	1% addition CXC 1612 Minimum PAB temperature at 180 seconds
HM340-317	60 seconds at 300°C	20 seconds at 300°C	180 seconds at 220°C
HM340-350	120 seconds at 300°C	30 seconds at 300°C	180 seconds at 220°C
HM340-383	180 seconds at 300°C	120 seconds at 300°C	180 seconds at 300°C

Table 4.8 Post application bake temperature and time of standard formulations, and formulations with a TAG based additive

To reduce this temperature/time further, it is possible to make use of thermal acid generators (TAG) in the formulation. Thermal acid generators are molecules that, on heating, release an acid group that is otherwise inert within the molecule, resulting in an acid species (147,148). The exact mechanism of a TAG depends on the blocking functional group. Figure 4.13 shows the mechanisms of different functional groups in TAGs (149). The choice of TAG depends heavily on the type and function of resist or hardmask; below are four different functional group and their properties (149):

1. Amine blocked acids – these are soluble in water and polar solvents, and can activate over a large temperature range.
2. Covalent blocked acids – hydrophobic TAGs that do not produce volatile species, have a narrow solubility range.
3. Quaternary blocked acids – these are usually solids that produce no volatiles species.

4. Metal blocked acids – Metals can act as catalysts, and can be hydrophobic or hydrophilic.

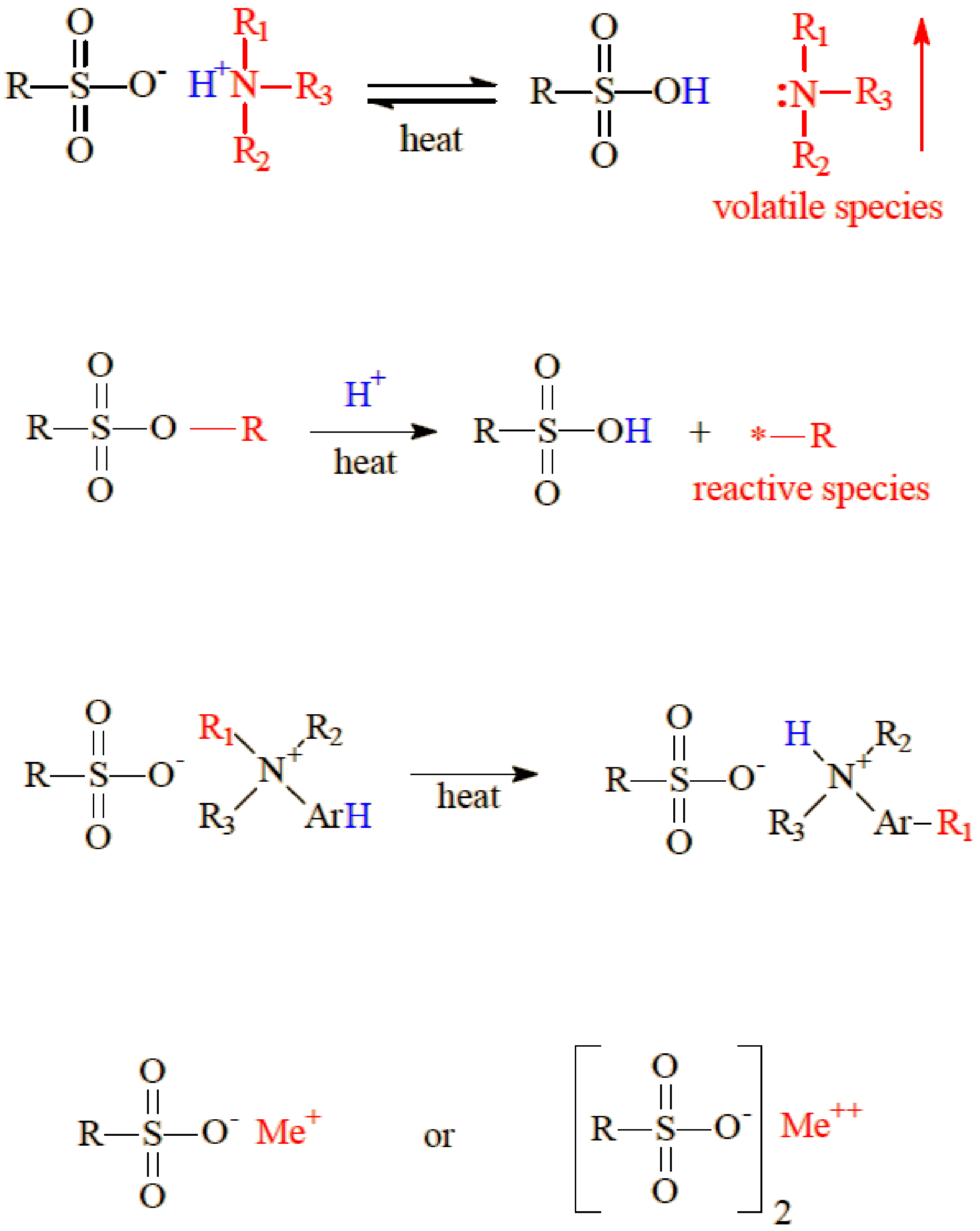

Figure 4.13 TAG blocking technologies and mechanisms of released acid groups(149)

Two different thermal acid generators, K-pure CXC-1612 containing Hexafluoroantimonate (SbF6) anions, and K-pure CXC-1821 which is a version of CXC-1612 without antimony, both quaternary blocked acids, were purchased from King Industries. These substances were chosen for their activation temperature, solubility and, in the case of CXC-1821, lack of metals. The TAG was added to formulations at different concentrations, up to 5 % to observe the effect upon the minimum temperature, and the minimum bake time required to have a fully insoluble film—one that would not lose thickness after elution with the casting solvent. Table 4.8 shows the results of the experiment. The TAG had a marked effect on the bake temperatures and duration or the 317 and 350 formulations, but did not reduce the crosslinking temperature in the higher carbon 383 formulation. As there is much less available CL-1201 in the 383 formulation, it can be theorised that the TAG changes the PAB conditions based on the CL-1201 rather than the fullerene. Further, increasing the concentration of the TAG to 5% still did not affect the PAB temperature or time required in the 383 formulations, whereas there was a noticeable effect at just 1% in the other 350 and 317 formulations.

4.3.5 Etch Rates

In the design of the hardmask, one of the most important factors is its etch properties, particularly the etch rate in halogen plasma such as SF_6/C_4F_8 and O_2 etches. Films of HM340-383, HM340-350 and HM340-317 were spun onto 4” wafers giving film thickness of 200nm. HM 340 samples were etched with N2:H2 with the following conditions: RF power: 10 w, ICP power: 500 w, Pressure: 10 mTorr N_2: 25 sccm, H_2: 11 sccm. The results of the etch is shown in Table 4.9, which shows that was a large difference in etch rate between the HM 340-317 and the higher carbon variants, but similar rates of the 1:1 and 5:1 fullerene to cross linker concentrations.

Sample	Etch Rate (Å/s)
HM340 -317	4.8
HM340- 350	2.6
HM340- 383	2.5

Table 4.9 Etch Rates of different hard mask formulations in H_2N_2.

Wafers of HM140 series, as well as control samples of polymethylmethacrylate (PMMA), polystyrene and SAL601 (a well-studied, chemically amplified resist) were etched using the Oxford Instruments applications lab for durability evaluation with an RIE etch process. The results of the etching trials are shown in Figure 4.14. Note that etching conditions are not available for this comparison study as etching was performed externally. The lower etch rate of the hardmask with higher fullerene confirms the expected results, and the HM340 resist is shown to be comparable to HM140 resist. The O_2 etch rate was also tested, shown in Figure 4.15.

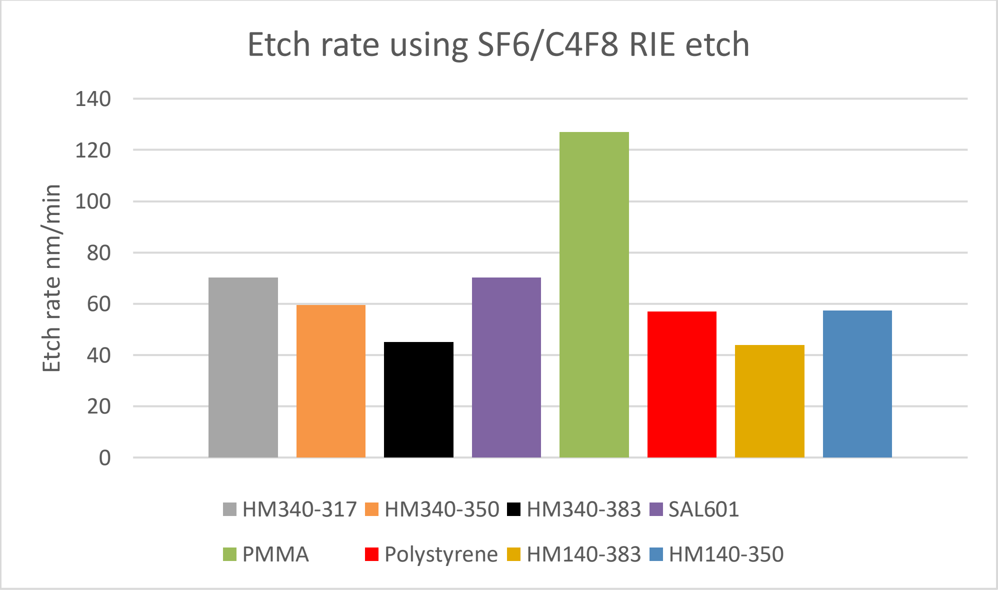

Figure 4.14 Blanket Etch rates for HM340 hardmask, with controls and HM140 series hardmasks.

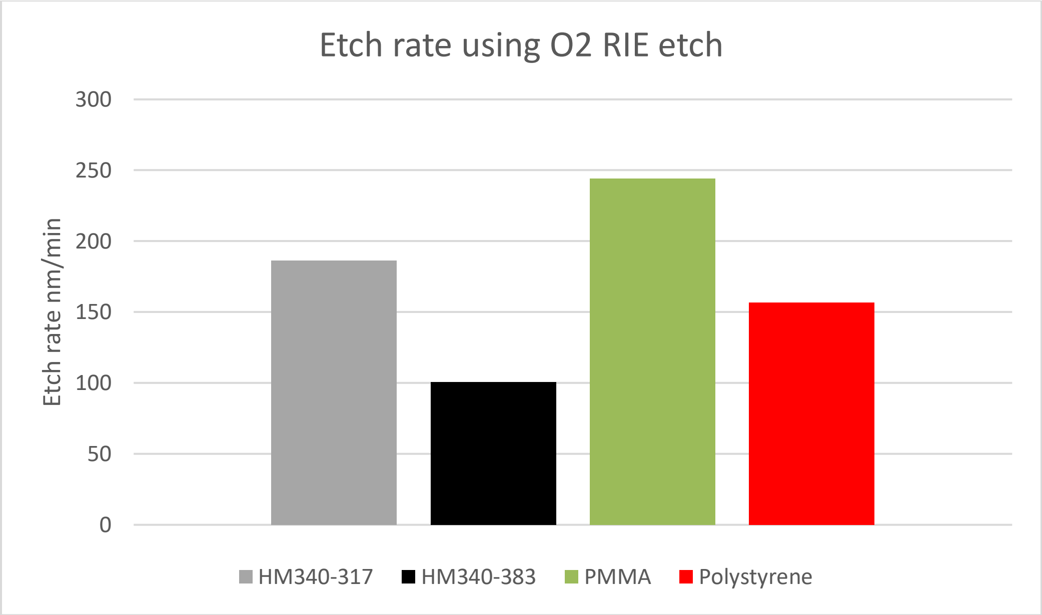

Figure 4.15 RIE blanket etch rates with O_2

Pattern transfer of dense lines was performed at PSI, to observe any wiggle effect with the HM340 resist. Wafers were prepared, patterned and etched at PSI. Figure 4.16 shows the results of the etch, importantly no wiggle is present.

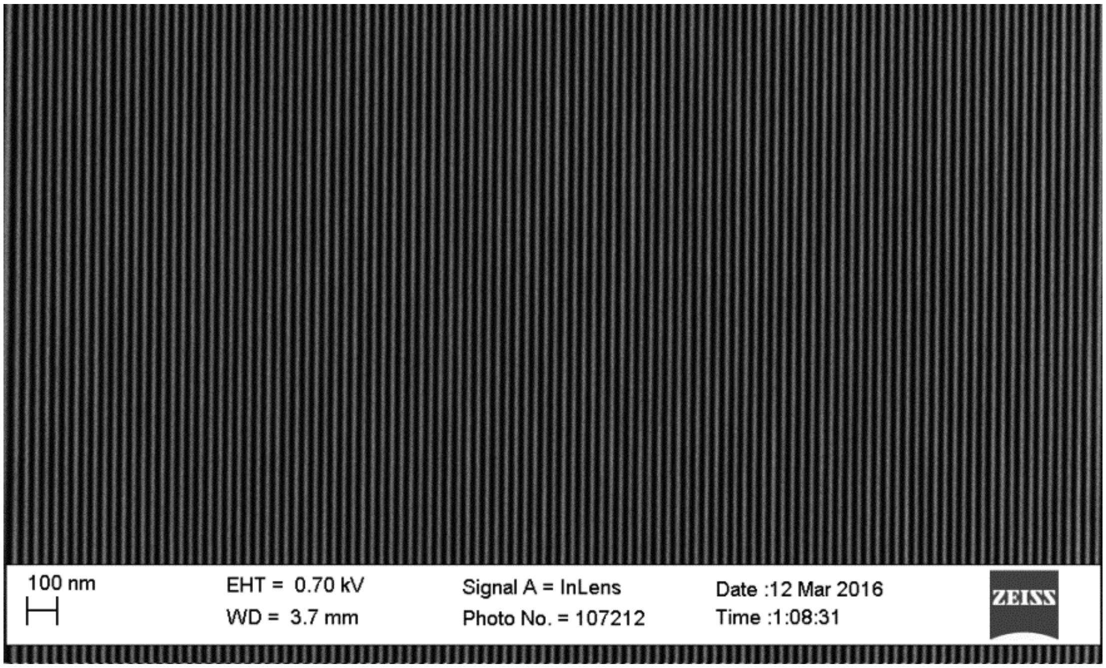

Figure 4.16 25nm half-pitch pattern transferred into HM340-383. Etching was undertaken by Dr. Andreas Frommhold, University of Birmingham

4.3.6 Drain Test

For use in the semiconductor industry, all materials must pass a drain test, that is be fully soluble in the drain liquids that run through the plant. Should the dissolved solids of a particular resist or hardmask precipitate out of solution in the drain line, it may cause blockages or contamination in the process. The hardmask material was normally dissolved in anisole or cyclohexanone solvents, whereas the industry has shifted PGMEA solvents due to their lesser environmental impact and increased safety. Therefore, it was a concern whether the HM340 series would be accepted by end users should there be precipitants when in a common drain line. Composition of the drain solvents were obtained as shown in Table 4.10. The Hansen solubility parameter was developed by C.Hansen in his 1967 paper(150) as a method of predicting solubility in different solvents.

Component Name	Common Name	Hansen Solubility Polarity(151)
Propylene glycol methyl ether acetate	PGMEA	5.7
Propylene glycol methyl ether	PGME	4.4
Cyclohexanone		6.3
Ethyl Lactate		7.6
Butyl Acetate		3.7
Methoxy-benzene	Anisole	4.1

Table 4.10 Solvents used in the drain test and their Hansen solubility parameters

The HM340 series SOC formulation was blended with each of the above solvents at a ratio of 1 part hardmask formulation, 9 parts solvent (to represent the conditions in a fabrication drain line), and also a mixture or equal parts of each solvent. Concentrations of HM340 were 100 g/l. Mixtures were fully mixed via ultrasonicifaction, and left undisturbed to settle. If any precipitant was observed or the mixture cloudy then the mixture was deemed to have failed the drain test. Table 4.11 along with Figure 4.17 shows the results of the tests. All mixtures containing the oQDM fullerenes failed the drain test in all solvents expect for cyclohexanone (vial J) although the HM340-350 was clearer than the HM340-383. PGMEA was observed to have the most cloudiness, and further experiments using PGMEA solvent showed the oQDM was only soluble in it to ~30 g/l, the results of this are summarised in Table 4.12.

Figure 4.17 Images of drain test results. Refer to Table 4.12 for formulations and solvents. From left to right: Vials D, G, H, I–N

Formulation	Vial	Solvent	Observation
oQDM (Anisole) 100 g/l	D	PGMEA	Cloudy precipitant
HM340-350 (Anisole) 100 g/l	G	PGMEA	Cloudy
HM340-383 (Anisole) 100 g/l	H	PGMEA	Cloudy precipitant
HM340-383 (Anisole) 100 g/l	I	PGME	Cloudy precipitant
HM340-383 (Anisole) 100 g/l	J	Cyclohexanone	Clear
HM340-383 (Anisole) 100 g/l	K	Ethyl Lactate	Cloudy precipitant
HM340-383 (Anisole) 100 g/l	L	Butyl Acetate	Cloudy precipitant
HM340-383 (Anisole) 100 g/l	M	Mixture	Cloudy precipitant
CL1201	N	PGMEA	Clear

Table 4.11 Results of mixing formulations with various drain test solvents. Images of results are shown in Figure 4.16

Formulation	Concentration (g / L)	Solvent	Observation	Fullerene Concentration (g / L)
HM340-383-010	100	PGMEA	Fails, cloudy	83.3
HM340-383-010	50	PGMEA	slightly cloudy	41.7
HM340-350-010	100	PGMEA	slightly cloudy	50.0
HM340-350-010	50	PGMEA	clear	25.0
HM340-317-010	100	PGMEA	clear	16.7
HM340-317-010	50	PGMEA	clear	8.3

Table 4.12 Results of lower concentration of HM340 hardmask, to determine maximum oQDM solubility in PGMEA.

4.4 HM900 Series Hardmask

To try to alleviate the issue of the drain test, it was necessary to look at the structure of the oQDM more closely. As there are only nonpolar groups on the molecule, and PGMEA and the other drain test solvents are fairly polar solvents, a fullerene with a polar functional group may help solvent compatibility. A modified version of oQDM (A-oQDM) was synthesised by Nano-C. This fullerene would be the bases of a new series of hardmask, the HM 900 series, consisting of A-oQDM and CL-1201. As with the 300 series ratios of the fullerene to crosslinker were created at 5:1, 1:1 and 1:5 and named HM940-383, HM940-350 and HM-940-317 respectively.

Drain tests were performed on the HM940 hardmask to see its solubility with regard to PGMEA solvents. the results are shown in Table 4.12 and Figure 4.18.

Formulation	Vial	Concentration (g/l)	Solvent	Observation	Fullerene Concentration (g/l)
HM940-383	D1	100	PGMEA	Slightly cloudy under bright light	83.3
HM940-350	E1	100	PGMEA	Very Slightly cloudy under bright light	50
HM940-317	F1	100	PGMEA	Clear	16.7
oQDM	oQDM	100	PGMEA	Fails, Very cloudy	100

Table 4.13 Drain test results for HM900 series formulations

It can be seen that the HM940 resists are much more compatible with the drain test solvents compared to the HM340.

Figure 4.18 Images of oQDM and HM940-383, 350 and 317 blended with PGMEA

4.5 Conclusions and Future work

The HM340 resists are promising in their properties to meet industry targets in etching, thermal stability and planarisation. However, the HM340 resists do not meet the industry targets with regard to solvent compatibility. Fortunately, a new set of SOC formulations, the HM900 series is much better in this regard, and initial studies have shown it outclasses the HM140 and HM340 in many regards. Future work will characterise the HM900 series further, as well as complete etch test trails on both the HM340 and HM900 series resists.

Chapter V

Conclusion and Further Work

The scope of the project was to create high resolutions patterns on surfaces to aid with accuracy of biosensors. Fabrication was performed and different methods investigated to prove the concept of a multi-electrode surface. There were difficulties with successful and consistent fabrication throughout the project, in particular lift-off in denser structures that had been created by ebeam lithography. It has been discussed that different lift-off methods and metal deposition methods may lead to better results in this area.
It was shown that fabrication of aluminum electrodes was achieved, but these did not respond well to electrochemistry, with the aluminium surfaces being physically removed. Silicon surfaces were also investigated as a method of creating SAMs, but inconstancies as measured by contact angle, and ellipsometry, in the deposited SAM quality led to using gold for both the surface electrodes and the raised electrodes. The use of the same material for each electrode required a technique to selectively clean a single electrode using linear sweep voltammetry. Thiol chemistry was used throughout to form good quality SAMs with alkane thiols, amino terminated thiols and alcohol terminated thiols.

Fabrication of the desired structures were successful at 50 nm lines at a 200 nm pitch, initially in aluminium, but these did not exhibit electrochemical behavior that made them suitable for use. Fabrication of gold electrodes was partially achieved, but removing of the gold was an issue. It has been discussed that using evaporation metal deposition would likely lead to better results in this area. Sandwich electrodes, in which a spin on carbon was used to separate a patterned surface from a second substrate were made and tested. Further work on these, including the deposition and measuring of SAMs and electrochemistry should be considered.

Future work to continue studies discussed in this thesis should focus on the addition on DNA molecules to the SAMs on the surface now that a useable surface can be fabricated. With both the sandwich electrode and the raised electrode, this work has not yet shown sensing of a target molecule. There are a number of challenges that will have to be overcome, particularly in the spacing of the DNA groups such as each will have sufficient volume into which conformational change can occur.

Park et al used a type of molecule called a dendron to control the surface density of an oligonucleotides. Dendrons are branched molecules, first created by Buhleier et al in 1978 (152), that use repeating units to exponentially grow each generation creating large bulky molecules (153). When attached to a SAM Figure 5.1 shows how spacing out groups on a surface leaves distances between the molecule to allow the space for hair pin loops to open. In the work by Tokuhisa et al (154), a spaced monolayer a gold surface was created by attaching a dendron to thioctic acid. The size of the dendron was able to control the spacing, and using a hydrolysis reaction dendrons could be cleaved leaving an acid terminated, spaced molecule, available for anchoring a modified DNA probe.

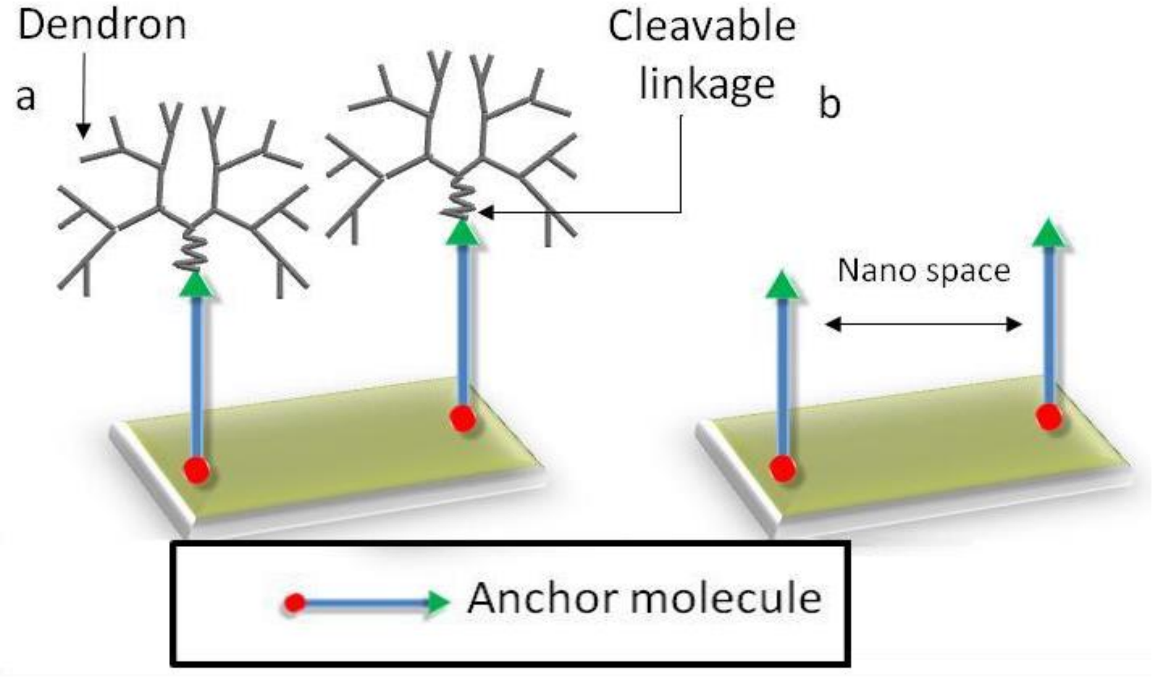

Figure 5.1 Dendrons are bulky molecules that can be used to space out anchor molecules ready for further modification

A second potential challenge with a working sensing surface is the diffusion of a target molecule to the small spaces in between the raised electrodes. Wider spacing between the interdigitated fingers of the sensors would aid in diffusion of the target to the surface at the cost of a lower surface area of the recognition molecule close to the raised electrode. The optimum density of the fabricated structures will need to be investigated, and ways of aiding diffusion, such as microfluidics may need to be considered (155).

The oQDM fullerene based hard mask, was a step forward in a series of hardmask resists, showing improved etching and thermal stability compared to the PCBM based resists. The HM-340 series resist was characterised at three formulations, each with different carbon content. Etching was performed that show stronger etch resistance to SF_6/C_4F_8 of 42 nm / min compared to 58 nm / min of the HM140. Work using thermal acid generators lowed the required post application bake temperature or post application time, and was particularly effective with the formulations containing a higher ratio of cross linker to fullerene, where PAB temperature was lowered from 300 °C to 220 °C.

Spin speed curves were developed, and the solubility of the formulations in a number of solvents were tested, giving different options for film thickness, surface roughness and the choice of safer solvents. Mixtures of two solvents at different concentrations were explored, and a cyclohexanone: anisole combination particularly successful. The drain test, where a formulation was tested in widely used solvents present in fabrication plants, showed that the HM340 series precipitated out in the more polar solvents PGMEA, PGME and Ethyl lactate. A new fullerene derivative, with an added polar group was developed, and synthesised, which showed much improvement in the drain test compared to the HM340.

Further work in the development of the hardmask would require the further characterisation and etch performance of the 340 series resists, and full characterisation of the 900 series formulation. Particularly it would be desirable to test the hardmasks in a multistack process shown in Figure 5.2 and examine the resulting etch compared to alternative carbon mask methods available, as direct comparisons are lacking.

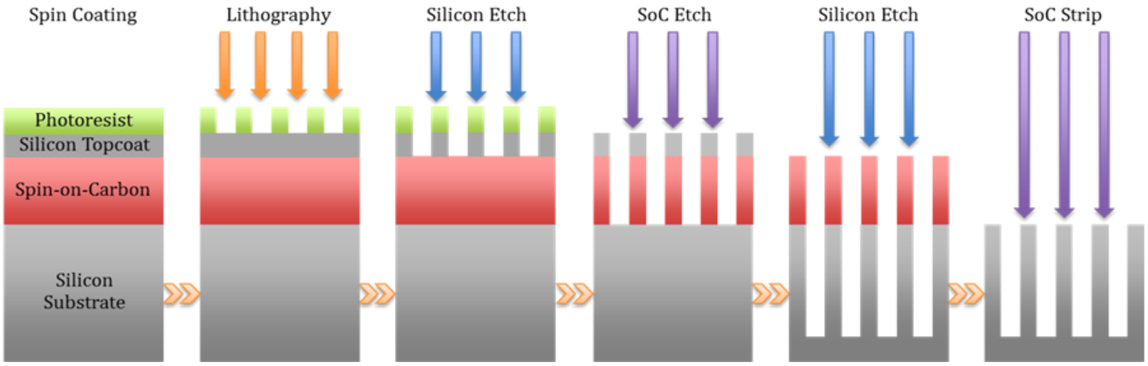

Figure 5.2 multistack process etching data

Further work on the development of different fullerene derivatives should be explored. By adding functional groups the solvent properties have been shown to be changeable, but self crosslinker fullerenes may be explored which would further increase the carbon content for a spin on carbon, leading to higher etch resistances.

REFERENCES

1. Sadana A, Sadana N. Handbook of Biosensors and Biosensor Kinetics. Handbook of Biosensors and Biosensor Kinetics. Elsevier; 2011.
2. Biosensors Market Size Worth USD 21.2 Billion By 2020 | CAGR 7.9% [Internet]. [cited 2019 Feb 12]. Available from: https://www.grandviewresearch.com/press-release/global-biosensors-market
3. Cheng KL. pH Glass Electrode and Its Mechanism. In 1989. p. 286–302.
4. Severinghaus JW, Astrup PB. History of blood gas analysis. IV. Leland Clark's oxygen electrode. J Clin Monit. 1986 Apr;2(2):125–39.
5. Clark LC, Lyons C. ELECTRODE SYSTEMS FOR CONTINUOUS MONITORING IN CARDIOVASCULAR SURGERY. Ann N Y Acad Sci. 2006 Dec 15;102(1):29–45.
6. Grieshaber D, MacKenzie R, Vörös J, Reimhult E. Electrochemical Biosensors - Sensor Principles and Architectures. Sensors (Basel). 2008 Mar 7;8(3):1400–58.
7. Rafique B, Iqbal M, Mehmood T, Shaheen MA. Electrochemical DNA biosensors: a review. Sens Rev. 2019 Jan 21;39(1):34–50.
8. Neugroschl J, Wang S. Alzheimer's disease: Diagnosis and treatment across the spectrum of disease severity. Vol. 78, Mount Sinai Journal of Medicine. 2011. p. 596–612.
9. Smittenaar CR, Petersen KA, Stewart K, Moitt N. Cancer incidence and mortality projections in the UK until 2035. Br J Cancer. 2016 Oct

25;115(9):1147–55.

10. Shui B, Tao D, Florea A, Cheng J, Zhao Q, Gu Y, et al. Biosensors for Alzheimer's disease biomarker detection: A review. Vol. 147, Biochimie. Elsevier B.V.; 2018. p. 13–24.

11. Bohunicky B, Mousa SA. Biosensors: The new wave in cancer diagnosis. Vol. 4, Nanotechnology, Science and Applications. 2011. p. 1–10.

12. Migliozzi D, Guibentif T. Assessing the Potential Deployment of Biosensors for Point-of-Care Diagnostics in Developing Countries: Technological, Economic and Regulatory Aspects. Biosensors. 2018 Nov 29;8(4):119.

13. Sin ML, Mach KE, Wong PK, Liao JC. Advances and challenges in biosensor-based diagnosis of infectious diseases. Vol. 14, Expert Review of Molecular Diagnostics. 2014. p. 225–44.

14. Thompson M, Krull UJ. Biosensors and the transduction of molecular recognition. Anal Chem. 1991 Apr;63(7):393A-405A.

15. V K. DNA Biosensors-A Review. J Bioeng Biomed Sci. 2017 Apr 5;07(02):1–5.

16. Luppa PB, Sokoll LJ, Chan DW. Immunosensors—principles and applications to clinical chemistry. Clin Chim Acta. 2001 Dec 1;314(1–2):1–26.

17. Gnoth C, Johnson S. Strips of hope: Accuracy of home pregnancy tests and new developments. Geburtshilfe Frauenheilkd. 2014;74(7):661–9.

18. Chard T. Pregnancy tests: a review. Hum Reprod. 1992 May;7(5):701–10.

19. Byrne B, Stack E, Gilmartin N, O'Kennedy R. Antibody-based sensors: Principles, problems and potential for detection of pathogens and associated

toxins. Vol. 9, Sensors (Switzerland). 2009. p. 4407–45.

20. Carr-Smith J. Modified nucleic acids: structural studies and applications in biosensing. 2015;

21. Madeleine Price Ball. File:Pregnancy test.svg - Wikimedia Commons [Internet]. [cited 2019 Jan 25]. Available from: https://commons.wikimedia.org/wiki/File%3APregnancy_test.svg

22. Ozsoz M. Electrochemical DNA biosensors. Pan Stanford Publishing; 2012.

23. Teengam P, Siangproh W, Tuantranont A, Vilaivan T, Chailapakul O, Henry CS. Multiplex Paper-Based Colorimetric DNA Sensor Using Pyrrolidinyl Peptide Nucleic Acid-Induced AgNPs Aggregation for Detecting MERS-CoV, MTB, and HPV Oligonucleotides. Anal Chem. 2017 May 16;89(10):5428–35.

24. Bhalla N, Jolly P, Formisano N, Estrela P. Introduction to biosensors. Essays Biochem. 2016 Jun 30;60(1):1–8.

25. Ju H. Electrochemical biosensors for DNA analysis. Front Biosci. 2005;10(1–3):37.

26. Xiao Y, Lubin AA, Baker BR, Plaxco KW, Heeger AJ. Single-step electronic detection of femtomolar DNA by target-induced strand displacement in an electrode-bound duplex. Proc Natl Acad Sci U S A. 2006 Nov 7;103(45):16677–80.

27. Wang JH, Wang K, Bartling B, Liu CC. The detection of alkaline phosphatase using an electrochemical biosensor in a single-step approach. Sensors. 2009 Nov;9(11):8709–21.

28. Tainaka K, Sakaguchi R, Hayashi H, Nakano S, Liew FF, Morii T. Design

strategies of fluorescent biosensors based on biological macromolecular receptors. Vol. 10, Sensors. 2010. p. 1355–76.

29. Song K-M, Lee S, Ban C. Aptamers and Their Biological Applications. Sensors. 2012 Jan 9;12(1):612–31.

30. Ku T-H, Zhang T, Luo H, Yen TM, Chen P-W, Han Y, et al. Nucleic Acid Aptamers: An Emerging Tool for Biotechnology and Biomedical Sensing. Sensors (Basel). 2015 Jul 6;15(7):16281–313.

31. Reverdatto S, Burz DS, Shekhtman A. Peptide aptamers: development and applications. Curr Top Med Chem. 2015;15(12):1082–101.

32. Dunn MR, Jimenez RM, Chaput JC. Analysis of aptamer discovery and technology. Nat Rev Chem. 2017 Oct 4;1(10):0076.

33. Mullis KB, Erlich HA, Arnheim N, Horn GT, Saiki RK, Scharf SJ. Process for amplifying, detecting, and/or cloning nucleic acid sequences. 1989.

34. Zhang X, Yadavalli VK. Surface immobilization of DNA aptamers for biosensing and protein interaction analysis. Biosens Bioelectron. 2011 Mar 15;26(7):3142–7.

35. Loaiza ÓA, Campuzano S, López-Berlanga M, Pedrero M, Pingarrón JM. Development of a DNA Sensor Based on Alkanethiol Self-Assembled Monolayer-Modified Electrodes. Sensors (Basel). 2005;5(6):344.

36. Zhuo Z, Yu Y, Wang M, Li J, Zhang Z, Liu J, et al. Recent Advances in SELEX Technology and Aptamer Applications in Biomedicine. Int J Mol Sci. 2017 Oct 14;18(10).

37. Grieshaber D, MacKenzie R, Vörös J, Reimhult E. Electrochemical Biosensors

- Sensor Principles and Architectures. Sensors. 2008 Mar 7;8(3):1400–58.

38. Duprey JLHA, Tucker JHR. Metalcarbon bonds in biopolymer conjugates: Bioorganometallic nucleic acid chemistry. Vol. 43, Chemistry Letters. 2014. p. 157–63.

39. Roberts HV. Ferrocene conjugated DNA for biosensing and antisense applications. 2018;

40. Tyagi S, Kramer FR. Molecular Beacons: Probes that Fluoresce Upon Hybridization. Nat Biotechnol. 1996;14(3):303–8.

41. Thelwell N. Mode of action and application of Scorpion primers to mutation detection. Nucleic Acids Res. 2000 Oct 1;28(19):3752–61.

42. Lubin AA, Plaxco KW. Folding-Based Electrochemical Biosensors: The Case for Responsive Nucleic Acid Architectures. Acc Chem Res. 2010 Apr 20;43(4):496–505.

43. Fan C, Plaxco KW, Heeger AJ. Electrochemical interrogation of conformational changes as a reagentless method for the sequence-specific detection of DNA. Proc Natl Acad Sci. 2003 Aug 5;100(16):9134–7.

44. Chatelain G, Ripert M, Farre C, Ansanay-Alex S, Chaix C. A “four-ferrocene” modified stem-loop structure as a probe for sensitive detection and single-base mismatch discrimination of DNA. Electrochim Acta. 2012 Jan 1;59:57–63.

45. Zhang X, Sun C, Fang N. Manufacturing at nanoscale: Top-down, bottom-up and system engineering. J Nanoparticle Res. 2004 Feb;6(1):125–30.

46. Kumar S, Bhushan P, Bhattacharya S. Fabrication of Nanostructures with Bottom-up Approach and Their Utility in Diagnostics, Therapeutics, and

Others. In 2018. p. 167–98.

47. Hobbs RG, Petkov N, Holmes JD. Semiconductor Nanowire Fabrication by Bottom-Up and Top-Down Paradigms. Chem Mater. 2012 Jun 12;24(11):1975–91.

48. Franssila S. Introduction to Microfabrication. Introduction to Microfabrication. John Wiley and Sons; 2010.

49. Tang L, Li X, Ji R, Teng KS, Tai G, Ye J, et al. Bottom-up synthesis of large-scale graphene oxide nanosheets. J Mater Chem. 2012 Mar 28;22(12):5676–83.

50. Thiruvengadathan R, Korampally V, Ghosh A, Chanda N, Gangopadhyay K, Gangopadhyay S. Nanomaterial processing using self-assembly-bottom-up chemical and biological approaches. Reports Prog Phys. 2013 Jun;76(6).

51. Laibinis PE, Whitesides GM, Allara DL, Tao YT, Parikh AN, Nuzzo RG. Comparison of the structures and wetting properties of self-assembled monolayers of n-alkanethiols on the coinage metal surfaces, copper, silver, and gold. J Am Chem Soc. 1991 Sep;113(19):7152–67.

52. Wink T, Van Zuilen SJ, Bult A, Van Bennekom WP. Self-assembled monolayers for biosensors. Vol. 122, Analyst. 1997.

53. Ivarsson BA, Hegg PO, Lundström KI, Jönsson U. Adsorption of proteins on metal surfaces studied by ellipsometric and capacitance measurements. Colloids and Surfaces. 1985;13(C):169–92.

54. Löfås S, Johnsson B. A novel hydrogel matrix on gold surfaces in surface plasmon resonance sensors for fast and efficient covalent immobilization of

ligands. J Chem Soc Chem Commun. 1990;(21):1526–8.

55. Kepley LJ, Crooks RM, Ricco AJ. A selective SAW-based organophosphonate chemical sensor employing a self-assembled, composite monolayer: a new paradigm for sensor design. Anal Chem. 1992 Dec 15;64(24):3191–3.

56. Bamdad C. A DNA self-assembled monolayer for the specific attachment of unmodified double- or single-stranded DNA. Biophys J. 1998;75(4):1997–2003.

57. UWEB :: Research : Biomaterials Tutorial [Internet]. [cited 2019 Feb 15]. Available from: https://www.uweb.engr.washington.edu/research/tutorials/sam.html

58. Mete E, Yortanli M, Danişman MF. A van der Waals DFT study of chain length dependence of alkanethiol adsorption on Au(111): Physisorption: vs. chemisorption. Phys Chem Chem Phys. 2017;19(21):13756–66.

59. Clegg RS, Hutchison JE. Hydrogen-Bonding, Self-Assembled Monolayers: Ordered Molecular Films for Study of Through-Peptide Electron Transfer. Langmuir. 1996 Jan;12(22):5239–43.

60. Nicosia C, Huskens J. Reactive self-assembled monolayers: From surface functionalization to gradient formation. Vol. 1, Materials Horizons. Royal Society of Chemistry; 2014. p. 32–45.

61. Lessel M, Bäumchen O, Klos M, Hähl H, Fetzer R, Paulus M, et al. Self-assembled silane monolayers: an efficient step-by-step recipe for high-quality, low energy surfaces. Surf Interface Anal. 2015 May 17;47(5):557–64.

62. Walsh R. Bond dissociation energy values in silicon-containing compounds

and some of their implications. Acc Chem Res. 1981 Aug;14(8):246–52.

63. Vericat C, Vela ME, Benitez G, Carro P, Salvarezza RC. Self-assembled monolayers of thiols and dithiols on gold: New challenges for a well-known system. Vol. 39, Chemical Society Reviews. 2010. p. 1805–34.

64. Bain CD, Troughton EB, Tao YT, Evall J, Whitesides GM, Nuzzo RG. Formation of monolayer films by the spontaneous assembly of organic thiols from solution onto gold. J Am Chem Soc. 1989 Jan;111(1):321–35.

65. Aswal DK, Lenfant S, Guerin D, Yakhmi J V., Vuillaume D. Self assembled monolayers on silicon for molecular electronics. Vol. 568, Analytica Chimica Acta. 2006. p. 84–108.

66. Ng A, Ciampi S, James M, Harper JB, Gooding JJ. Comparing the Reactivity of Alkynes and Alkenes on Silicon (100) Surfaces †. Langmuir. 2009 Dec 15;25(24):13934–41.

67. Zhang S, Chandra KL, Gorman CB. Self-Assembled Monolayers of Terminal Alkynes on Gold. J Am Chem Soc. 2007 Apr;129(16):4876–7.

68. Villares A, Lydon DP, Low PJ, Robinson BJ, Ashwell GJ, Royo FM, et al. Characterization and Conductivity of Langmuir–Blodgett Films Prepared from an Amine-Substituted Oligo(phenylene ethynylene). Chem Mater. 2008 Jan;20(1):258–64.

69. Martín S, Haiss W, Higgins S, Cea P, López MC, Nichols RJ. A Comprehensive Study of the Single Molecule Conductance of α,ω-Dicarboxylic Acid-Terminated Alkanes. J Phys Chem C. 2008 Mar;112(10):3941–8.

70. Villares A, Lydon DP, Robinson BJ, Ashwell GJ, Royo FM, Low PJ, et al. Langmuir-Blodgett films incorporating molecular wire candidates of ester-substituted oligo(phenylene-ethynylene) derivatives. Surf Sci. 2008 Dec 15;602(24):3683–7.

71. Fock J, Sørensen JK, Lörtscher E, Vosch T, Martin CA, Riel H, et al. A statistical approach to inelastic electron tunneling spectroscopy on fullerene-terminated molecules. Phys Chem Chem Phys. 2011 Aug 28;13(32):14325–32.

72. Herrer L, González-Orive A, Marqués-González S, Martín S, Nichols RJ, Serrano JL, et al. Electrically transmissive alkyne-anchored monolayers on gold. Nanoscale. 2019 Apr 28;11(16):7976–85.

73. Schreiber F. Self-assembled monolayers: From “simple” model systems to biofunctionalized interfaces. J Phys Condens Matter. 2004 Jul 21;16(28).

74. Kondoh H, Kodama C, Sumida H, Nozoye H. Molecular processes of adsorption and desorption of alkanethiol monolayers on Au(111). J Chem Phys. 1999 Jul 15;111(3):1175–84.

75. Onclin S, Ravoo BJ, Reinhoudt DN. Engineering silicon oxide surfaces using self-assembled monolayers. Vol. 44, Angewandte Chemie - International Edition. 2005. p. 6282–304.

76. Ulman A. Formation and Structure of Self-Assembled Monolayers. Chem Rev. 1996 Jan;96(4):1533–54.

77. Pranzetti A. Switchable charged surfaces to regulate bacterial adhesion. 2014;

78. Cometto FP, Paredes-Olivera P, Macagno VA, Patrito EM. Density Functional Theory Study of the Adsorption of Alkanethiols on Cu(111), Ag(111), and

Au(111) in the Low and High Coverage Regimes. J Phys Chem B. 2005 Nov;109(46):21737–48.

79. Kankate L, Turchanin A, Gölzhäuser A. On the Release of Hydrogen from the S−H groups in the Formation of Self-Assembled Monolayers of Thiols. Langmuir. 2009 Sep 15;25(18):10435–8.

80. Zuo X, Song S, Zhang J, Pan D, Wang L, Fan C. A Target-Responsive Electrochemical Aptamer Switch (TREAS) for Reagentless Detection of Nanomolar ATP. J Am Chem Soc. 2007 Feb;129(5):1042–3.

81. Munuera C, Barrena E, Ocal C. Chain-Length Dependence of Metastable Striped Structures of Alkanethiols on Au(111). Langmuir. 2005 Aug;21(18):8270–7.

82. Nuzzo RG, Zegarski BR, Dubois LH. Fundamental studies of the chemisorption of organosulfur compounds on gold(111). Implications for molecular self-assembly on gold surfaces. J Am Chem Soc. 1987 Feb;109(3):733–40.

83. Moore GE. Cramming more components onto integrated circuits, Reprinted from Electronics, volume 38, number 8, April 19, 1965, pp.114 ff. IEEE Solid-State Circuits Soc Newsl. 2006 Sep;11(3):33–5.

84. International Roadmap for Devices and Systems (IRDS^{TM}) 2018 Edition - IEEE International Roadmap for Devices and Systems^{TM} [Internet]. [cited 2019 Dec 31]. Available from: https://irds.ieee.org/editions/2018

85. Razavy M. Quantum Theory of Tunneling. Quantum Theory of Tunneling. WORLD SCIENTIFIC; 2003.

86. Wilson M. Immersion Objectives: Using Oil, Glycerol, or Water to Overcome some of the Limits of Resolution. 2017.

87. Broglie L de. XXXV. *A tentative theory of light quanta*. London, Edinburgh, Dublin Philos Mag J Sci. 1924 Feb 8;47(278):446–58.

88. Von Ardenne M. 4.4 Reminiscences on the origins of the scanning electron microscope and the electron microprobe. In: Advances in Imaging and Electron Physics. Academic Press Inc.; 1996. p. 635–52.

89. Nanotechnology Now - Press Release: Hitachi Launches World's Highest Resolution FE-SEM [Internet]. [cited 2019 Dec 31]. Available from: http://www.nanotech-now.com/news.cgi?story_id=42612

90. Zhou W, Apkarian R, Wang ZL, Joy D. Fundamentals of scanning electron microscopy (SEM). In: Scanning Microscopy for Nanotechnology: Techniques and Applications. Springer New York; 2007. p. 1–40.

91. MyScope [Internet]. [cited 2020 Jan 3]. Available from: https://myscope.training/#/SEMlevel_3_1

92. Claudionico. Electron Interaction with Matter [Internet]. [cited 2019 Feb 26]. Available from: https://en.wikipedia.org/wiki/Electron_microscope

93. Dirne F. Electron Beam Lithography -key enabling technology in nanofabrication [Internet]. Available from: https://fhi.nl/

94. Huang V, Chiu CC, Lin CA, Chang CY, Gau TS, Lin BJ. Effect of novel rinsing material and surfactant treatment on the resist pattern performance. In: Lin Q, editor. International Society for Optics and Photonics; 2007. p. 65193C.

95. Drechsler A, Bellmann C, Synytska A, Petong N, Grundke K, Stamm M, et al.

The adsorption of cationic surfactants on photoresist surfaces and its effect on the pattern collapse in high aspect ratio patterning. Colloids Surfaces A Physicochem Eng Asp. 2007 Dec;311(1–3):83–92.

96. Montgomery W, Robinson APG, Dawson G, McClelland A, Brown AG, Lada T. High-carbon fullerene based spin-on organic hardmask. In: Hohle CK, Gronheid R, editors. Advances in Patterning Materials and Processes XXXV. SPIE; 2018. p. 22.

97. Irresistible Materials – Developing advanced materials for a new generation of microchip technology [Internet]. [cited 2019 Feb 27]. Available from: http://irresistiblematerials.com/

98. Home page [Internet]. [cited 2019 Feb 16]. Available from: https://www.jd-photodata.co.uk/

99. Nayak AP, VJ L, Islam and MS. Wet and Dry Etching | Microtechnology | Semiconductors [Internet]. [cited 2019 Feb 27]. Available from: https://www.scribd.com/document/200796337/Wet-and-Dry-Etching

100. Adamson AW, Gast AP (Alice P. Physical chemistry of surfaces. Wiley; 1997. 784 p.

101. Gould RF, editor. Contact Angle, Wettability, and Adhesion, Copyright, Advances in Chemistry Series. In 1964. p. i–iii.

102. Millar J, Stamford JA, Kruk ZL, Wightman RM. Electrochemical, pharmacological and electrophysiological evidence of rapid dopamine release and removal in the rat caudate nucleus following electrical stimulation of the median forebrain bundle. Eur J Pharmacol. 1985 Mar 12;109(3):341–8.

103. Fisher AC. Electrode Dynamics. Oxford University Press; 1996. 83 p.

104. Compton RG, Banks CE. Understanding voltammetry. Understanding Voltammetry. World Scientific Publishing Co.; 2007. 1–371 p.

105. Fan C, Plaxco KW, Heeger AJ. Electrochemical interrogation of conformational changes as a reagentless method for the sequence-specific detection of DNA. Proc Natl Acad Sci U S A. 2003 Aug 5;100(16):9134–7.

106. Iqbal P, Critchley K, Attwood D, Tunnicliffe D, Evans SD, Preece JA. Chemical Manipulation by X-rays of Functionalized Thiolate Self-Assembled Monolayers on Au. Langmuir. 2008 Dec 16;24(24):13969–76.

107. Beulen MWJ, Huisman B-H, van der Heijden PA, van Veggel FCJM, Simons MG, Biemond EMEF, et al. Evidence for Nondestructive Adsorption of Dialkyl Sulfides on Gold. Langmuir. 1996 Jan;12(26):6170–2.

108. Chen C, Hutchison JE, Postlethwaite TA, Richardson JN, Murray RW. Chemically Modified Electrodes by Nucleophilic Substitution of Chlorosilylated Platinum Oxide Surfaces. Langmuir. 1994 Sep;10(9):3332–7.

109. Zeng X, Xu G, Gao Y, An Y. Surface Wettability of (3-Aminopropyl)triethoxysilane Self-Assembled Monolayers. J Phys Chem B. 2011 Jan 27;115(3):450–4.

110. Jönsson U, Olofsson G, Malmqvist M, Rönnberg I. Chemical vapour deposition of silanes. Thin Solid Films. 1985 Feb 8;124(2):117–23.

111. Turan E, Caykara T. Construction of hydroxyl-terminated poly(N-isopropylacrylamide) brushes on silicon wafer via surface-initiated atom transfer radical polymerization. J Polym Sci Part A Polym Chem. 2010 Jul

15;48(17):3880–7.

112. Balachander N, Sukenik CN. Monolayer transformation by nucleophilic substitution: Applications to the creation of new monolayer assemblies. Langmuir. 1990 Nov;6(11):1621–7.

113. Silberzan P, Leger L, Ausserre D, Benattar JJ. Silanation of silica surfaces. A new method of constructing pure or mixed monolayers. Langmuir. 1991 Aug;7(8):1647–51.

114. Germer K, Leonard M, Zhang X. RNA aptamers and their therapeutic and diagnostic applications. Int J Biochem Mol Biol. 2013;4(1):27–40.

115. Lewis S, Piccirillo L. Influence of Nanocomposite Materials for Next Generation Nano Lithography. In: Advances in Diverse Industrial Applications of Nanocomposites. InTech; 2011.

116. EM Resist – Specialists in electron beam resist [Internet]. [cited 2019 Feb 25]. Available from: http://www.emresist.com/

117. Lewis SM, DeRose GA. SML electron beam resist: Ultra-high aspect ratio nanolithography. Front Nanosci. 2016 Jan 1;11:421–46.

118. SML Product information [Internet]. [cited 2019 Jan 23]. Available from: http://www.emresist.com/downloads/SML Resist Product Information.pdf

119. Mazlan NS, Ramli MM, Abdullah MMAB, Halin DSC, Isa SSM, Talip LFA, et al. Interdigitated electrodes as impedance and capacitance biosensors: A review. In: AIP Conference Proceedings. American Institute of Physics Inc.; 2017.

120. Dario Giovanni Bazzoli. Surface patterning and SAM deposition for future

enhanced micro-design of electrochemical apta-sensors. University of Birmingham; 2018.

121. Markovsky B, Amalraj F, Gottlieb HE, Gofer Y, Martha SK, Aurbach D. On the Electrochemical Behavior of Aluminum Electrodes in Nonaqueous Electrolyte Solutions of Lithium Salts. J Electrochem Soc. 2010;157(4):A423.

122. Hamelin A. Cyclic voltammetry at gold single-crystal surfaces. Part 1. Behaviour at low-index faces. Vol. 407, Journal of Electroanalytical Chemistry. Elsevier; 1996. p. 1–11.

123. Hamelin A, Martins AM. Cyclic voltammetry at gold single-crystal surfaces. Part 2. Behaviour of high-index faces. Vol. 407, Journal of Electroanalytical Chemistry. Elsevier; 1996. p. 13–21.

124. Hoare JP. A Cyclic Voltammetric Study of the Gold-Oxygen System. J Electrochem Soc. 1984;131(8):1808–15.

125. Fischer LM, Tenje M, Heiskanen AR, Masuda N, Castillo J, Bentien A, et al. Gold cleaning methods for electrochemical detection applications. Microelectron Eng. 2009 Apr 1;86(4–6):1282–5.

126. Heiskanen AR, Spégel CF, Kostesha N, Ruzgas T, Emnéus J. Monitoring of *Saccharomyces cerevisiae* Cell Proliferation on Thiol-Modified Planar Gold Microelectrodes Using Impedance Spectroscopy. Langmuir. 2008 Aug 19;24(16):9066–73.

127. Heiskanen AR, Spégel CF, Kostesha N, Ruzgas T, Emnéus J. Monitoring of Saccharomyces cerevisiae cell proliferation on thiol-modified planar gold microelectrodes using impedance spectroscopy. Langmuir. 2008 Aug

19;24(16):9066–73.

128. Kakiuchi T, Usui H, Hobara D, Yamamoto M. Voltammetric Properties of the Reductive Desorption of Alkanethiol Self-Assembled Monolayers from a Metal Surface. Langmuir. 2002 Jun;18(13):5231–8.

129. Šustrová B, Štulík K, Mareček V, Janda P. A Study of the Modification of the Gold Electrode Surface with a Calix[4]arene Self-Assembled Monolayer. Electroanalysis. 2010 Sep;22(17–18):2051–7.

130. Shen P-T, Sivan Y, Lin C-W, Liu H-L, Chang C-W, Chu S-W. Temperature- and roughness-dependent permittivity of annealed/unannealed gold films. Opt Express. 2016 Aug 22;24(17):19254.

131. Hafnium Oxide HfO2 for Optical Coating [Internet]. [cited 2019 Feb 25]. Available from: https://materion.com/resource-center/product-data-and-related-literature/inorganic-chemicals/oxides/hafnium-oxide-hfo2-for-optical-coating

132. Robertson J. High dielectric constant oxides. Eur Phys J Appl Phys. 2004 Dec 2;28(3):265–91.

133. Bogdanov AL, Andersson EK. Fine undercut control in bilayer PMMA-P(MMA-MAA) resist system for e-beam lithography with submicrometer resolution. In: Peckerar MC, editor. 1991. p. 324.

134. Blanchard-Dionne A-P, Meunier M. Electron beam lithography using a PMMA/P(MMA 8.5 MAA) bilayer for negative tone lift-off process. J Vac Sci Technol B, Nanotechnol Microelectron Mater Process Meas Phenom. 2015 Nov;33(6):061602.

135. Brown AG, Frommhold A, Lada T, Bowen J, el Otell Z, Robinson APG. Spin-on-carbon hard masks utilising fullerene derivatives. In: Hohle CK, Younkin TR, editors. 2016. p. 977927.

136. Semiconductor Engineering .:. The Problem With Spin-On Carbon Materials [Internet]. [cited 2019 Feb 21]. Available from: https://semiengineering.com/the-problem-with-high-temp-spin-on-carbon-materials/

137. Weigand M, Krishnamurthy V, Wang Y, Lin Q, Guerrero D, Simmons S, et al. Evaluating spin-on carbon materials at low temperatures for high wiggling resistance. In: Zhang Y, Oehrlein GS, Lin Q, editors. 2013. p. 86850R.

138. Tadokoro M, Yonekura K, Yoshikawa K, Ono Y, Ishibashi T, Hanawa T, et al. Improvement of the wiggling profile of spin-on carbon hard mask by H 2 plasma treatment. J Vac Sci Technol B Microelectron Nanom Struct. 2008;26(1):67–71.

139. van Delft FCMJM. Delay-time and aging effects on contrast and sensitivity of hydrogen silsesquioxane. J Vac Sci Technol B Microelectron Nanom Struct. 2002 Dec 9;20(6):2932.

140. M. Glodde, S. Engelmann, M. Guillorn, S. Kanakasabapathy, E. Mclellan, C.-S.Koay, Y. Yin, M. Sankarapandian, J.C. Arnold, K. Petrillo, M. Brink, H. Miyazoe, E.A. de Silva, H. Yusuff, K.-S. Yoon, Y. Wei, C.-H.J. Wu PRV. No Title. In: spie. 2011. p. 797216.

141. Kroto HW, Heath JR, O’Brien SC, Curl RF, Smalley RE. C60: Buckminsterfullerene. Nature. 1985 Nov;318(6042):162–3.

142. Huy PDQ, Li MS. Binding of fullerenes to amyloid beta fibrils: size matters. Phys Chem Chem Phys. 2014 Oct 7;16(37):20030–40.

143. Frommhold A, Manyam J, Palmer RE, Robinson APG. Fullerene-based spin-on-carbon hardmask. Microelectron Eng. 2012 Oct 1;98:552–5.

144. Application Notes for photolitografy with technical informations for photoresists, solvents, developers and etchants [Internet]. [cited 2019 Feb 21]. Available from: https://www.microchemicals.com/downloads/application_notes.html

145. Spin Coating: A Guide to Theory and Techniques – Ossila [Internet]. [cited 2019 Feb 20]. Available from: https://www.ossila.com/pages/spin-coating#spin-coating-general-theory

146. Frommhold A, Brown AG, Lada T, Bowen J, Robinson APG. Fullerene derivative based spin-on-carbon hard masks for advanced lithographic applications. 2015 Jul 15;

147. Oberlander JE, Wanat SF, McKenzie DS, Kokinda E. Thermal acid generator (TAG) synthesis variables and their effect on resist performance. In: Houlihan FM, editor. 2000. p. 655.

148. Kudo T, Rahman MD, McKenzie D, Anyadiegwu C, Doerrenbaecher S, Zahn W, et al. Development of spin-on-carbon hard mask for advanced node. In: Advances in Patterning Materials and Processes XXXI. SPIE; 2014. p. 90511X.

149. Electronics: K-PURE | King Industries, Inc. [Internet]. [cited 2019 Feb 21]. Available from: https://www.kingindustries.com/products/electronics-k-pure/

150. HANSEN, M. C. Three dimensional solubility parameter-key to paint-component affinities : Dyes, emulsifiers, mutual solubility and compatibility, and pigments. J Paint Technol. 1967;39:505.

151. Hansen CM. Hansen solubility parameters : a user's handbook. CRC Press; 2007. 519 p.

152. Buhleier E, Wehner W, Vögtle F. "Cascade"- And "nonskid-chain-like" syntheses of molecular cavity topologies. Synth. 1978 Feb 1;1978(2):155–8.

153. Diederich F, Echegoyen L, Gómez-López M, Kessinger R, Stoddart JF. The self-assembly of fullerene-containing [2]pseudorotaxanes: Formation of a supramolecular C60 dimer. J Chem Soc Perkin Trans 2. 1999;(8):1577–86.

154. Tokuhisa H, Liu J, Omori K, Kanesato M, Hiratani K, Baker LA. Efficient biosensor interfaces based on space-controlled self-assembled monolayers. Langmuir. 2009 Feb 3;25(3):1633–7.

155. Jiang L, Korivi NS. Microfluidics: Technologies and applications. In: Nanolithography: The Art of Fabricating Nanoelectronic and Nanophotonic Devices and Systems. Elsevier Ltd; 2013. p. 424–43.